Isogeometric and immersogeometric analysis of incompressible flow problems

PROEFSCHRIFT

ter verkrijging van de graad van doctor aan de Technische Universiteit Eindhoven, op gezag van de rector magnificus prof.dr.ir. F.P.T. Baaijens, voor een commissie aangewezen door het College voor Promoties, in het openbaar te verdedigen op maandag 05 februari 2018 om 13:30 uur

door

Tuong Hoang

geboren te Ho Chi Minhstad, Vietnam

Dit proefschrift is goedgekeurd door de promotoren en de samenstelling van de promotiecommissie is als volgt:

voorzitter:	prof.dr. L.P.H. de Goey
1^e promotor:	prof.dr.ir. E.H. van Brummelen
2^e promotor:	prof.dr. A. Reali (Università degli studi di Pavia)
copromotoren:	dr.ir. C.V. Verhoosel
	prof.dr. F. Auricchio (Università degli studi di Pavia)
leden:	prof.dr. E. Rank (TU München)
	prof.dr. M.G. Larson (Umeå Universitet)
	prof.dr.ir. N.G. Deen

Het onderzoek of ontwerp dat in dit proefschrift wordt beschreven is uitgevoerd in overeenstemming met de TU/e Gedragscode Wetenschapsbeoefening

To my beloved father (1942–2017), who could not see this dissertation completed

The work in this thesis has been funded by the European Commission EACEA Agency, Framework Partnership Agreement 2013-0043 Erasmus Mundus Action 1b, as a part of the *EM Joint Doctorate Simulation in Engineering and Entrepreneurship Development* (SEED).

Istituto Universitario di Studi Superiori di Pavia, 2018
Technische Universiteit Eindhoven, 2018

A catalogue record is available from the Eindhoven University of Technology Library.
ISBN 978-90-386-4449-3

Cover design by Tra Nguyen-Thanh

Preface

This dissertation has been part of the Erasmus Mundus Joint Doctorate program Simulation in Engineering and Entrepreneurship Development (EMJD-SEED). The research has been carried out from 2013 to 2017 at the Computational Mechanics & Advanced Materials group - Department of Civil Engineering and Architecture, University of Pavia, and the Energy Technology and Fluid Dynamics group - Department of Mechanical Engineering, Eindhoven University of Technology.

First of all, I would like to express my gratitude to my Italian promotor Alessandro Reali and co-promotor Ferdinando Auricchio. Thank you for accepting me to be part of the Pavia team. I really appreciate your great vision for conducting research, which helped me guide myself through the PhD journey.

Next, I would like to acknowledge my Dutch promotor Harald van Brummelen and co-promotor Clemens Verhoosel. Thank you for your unconditional dedicated supervision, weekdays and weekends. The rigorousness from Harald and the excellent project implementation skill from Clemens is a perfect match which I am so lucky to have. I could not find a better environment.

Once again, to my promotors and co-promotors, please receive my deepest thanks for the encouragement and freedom offered to me, so that I could be an independent reseacher and thinker.

Also, I would like to thank my committee members, Ernst Rank, Mats G. Larson, and Niels G. Deen for spending time reading and giving feedback on my thesis.

I am thankful to the Evalf Computing team for the Nutils software package, which plays an important role in my numerical experiments. Special thanks go to Gertjan van Zwieten for his assistance in the realization of mathematical formulations into computer codes in a beautiful way. Also, I want to thank

Chaozhong Qin for the resulting fruitful collaboration during my last year, due to our different expertise and perspectives.

I would like to thank all of my Compmech friends in Pavia for the cheerful time being together, with Italian food, language, and culture. I am grateful to the MEFD friends in Eindhoven for the unforgetable memories we have been sharing. I also want to thank my Vietnamese friends in Italy and The Netherlands for the social activities that helped me relieve homesickness and uplift me through hardships.

I am grateful to my former Vietnamese teachers and professors in my high-schools (LVT, 218LTT, PTNK), my bachelor (HCMUP), and my master (HCMUS) studies for their mathematical love and inspiration. I would like to thank my former master supervisor Hung Nguyen-Xuan, for introducing me to Computational Mechanics.

A special recognition goes to my family. I am indebted to the unconditional sacrifice of my Mom and Dad, they are my heroes. All of my efforts so far are nothing compared to what they have encountered. To my brothers, I am happy to have you. And finally, I would like to thank Tra - my love, for her support, smile, and understanding.

Hoàng Tường
Utrecht, January 2018

Contents

List of Figures

List of Tables

Chapter 1
Introduction

The study of fluid mechanics dates (at least) back to ancient Greece and Rome, in particular with the famous work of Archimedes (*ca.* 250 BC). The study of eddies, vortices, and turbulence by Leonardo da Vinci in the Renaissance (*ca.* 1508) is commonly considered as the pioneering work on fluid dynamics. Around a century and a half after Newton's *Principia Mathematica* (1687), a rigorous continuum mechanics framework for fluid dynamics was developed in the form of the Navier-Stokes equations[1] (NSEs). Ever since, the NSEs have been the universally accepted model for viscous flow problems.

Until today the behavior of solutions to the NSEs is still not fully understood. Analytical solutions for the NSEs can only be derived under special assumptions, with simple geometries for which the complexity of the equations can be reduced. For instance, solutions for the flow between two parallel plates or for the flow in a circular pipe can be represented explicitly. In general cases and with more complex geometries, solving the NSEs analytically is generally impossible. Moreover, from a purely mathematical point of view, the question about the existence and smoothness of solutions to the NSEs in three dimensions is still an open problem [1]. Answering this question is considered as one of the seven most important open problems in mathematics as formulated by The Clay Mathematics Institute, with an award of US$ 1,000,000 offered for a solution.

The advent of computers opened new doors to studies and applications of NSEs. This branch of computational science is referred to as Computational Fluid Dynamics (CFD). Computational science is a rapidly growing

[1] The major contributions to the development of the NSEs are generally attributed to Euler (1757), Navier (1823), Cauchy (1828), Poisson (1829), Saint Venant (1843) and Stokes (1845).

multidisciplinary field that employs advanced computing technology to study complex problems, and is nowadays commonly considered as the third pillar of science, besides the traditional theory and experimentation pillars. The combination of mathematical analysis and the power of computers makes it possible to solve the NSEs numerically. The work in this thesis is conducted within the scope of the field of CFD, as it considers the development of a geometrically versatile solution technique for the NSEs.

1.1 Background

In this thesis we focus ourselves to incompressible flow problems, which are governed by the incompressible Navier-Stokes equations[2] (NSEs). In an incompressible flow the density of a fluid element does not change during its motion. For incompressible flows, the divergence of the velocity field is zero. From a continuum mechanics point of view, the incompressible NSEs can be derived from the conservation laws of momentum and mass.

1.1.1 Finite Element Methods for incompressible fluid flows

The NSEs are useful for describing many physical phenomena in science and engineering. The applications are vast, ranging from atmospheric changes, ocean currents, and surface flows in rivers in geo-engineering, to fluid flows in pipes and subsurface flows in oil reservoirs in petroleum engineering, and air flow around wings in aerospace engineering. Nowadays, computer simulations of the NSEs play an important role in, for example, the design of aircraft and cars, studying blood flows inside the human body, designing power stations, and understanding pollution transport.

Finite Element Analysis (FEA) was pioneered by Courant (1943), who utilized the Ritz method to obtain approximate solutions of vibration systems. The term "Finite Element" was later introduced in the work of Clough (1960). Since its introduction, FEA has been applied and developed intensively, with contributions from many different fields, including engineering and mathematics. We refer the reader to, *e.g.*, Refs. [2–4] for reference works regarding

[2] Throughout this thesis, when we refer to the NSEs, the incompressibility assumption is implied.

FEA. The first applications of the FEM for solving Stokes and the NSEs were studied in the 1970s. The stability analysis for FEM of these equations was introduced by Babuška in 1971 [5] and Brezzi in 1974 [6]. Prior to that, the problem on the existence and smoothness of the continuous NSEs in two dimensions was solved by Ladyzhenskaya in 1961 [7], and the necessary and sufficient condition for the well-posedness of bilinear operators in Hilbert spaces – nowadays referred to as the inf-sup condition – was stated by Necas in 1962 [8]. The inf-sup condition is the foundation for the development of inf-sup stable mixed element methods for fluids. The early monographs in FEM for fluids of Girault and Raviart (1979) [9], and the extended versions in 1986 and 2012 are classical references [10, 11] in this field. Other classic references for mixed and hybrid methods are the books by Boffi, Brezzi and Fortin [12, 13].

The incompressibility constraint in the NSEs and its Stokes linearization does not allow for straight-forward application of the FEM in the sense that the discrete approximation spaces for velocity and pressure cannot be chosen arbitrarily. Instead, a compatible pair must be selected to satisfy the inf-sup condition. If the inf-sup condition is violated, unphysical spurious oscillations occur. The same phenomena happens in (linear) elasticity problems when the material is (quasi-)incompressible (such as rubber-like materials). Finding pairs of inf-sup stable spaces has been an active field of research over the last decades. The recently proposed periodic table of mixed elements (Arnold and Logg [14]) – which has been developed in the framework of finite element exterior calculus (FEEC) [15–17] – aims at systematically classifying the (well-)known pairs, and to indicate new mixed element pairs.

An alternative approach to circumvent the inf-sup stability condition is to use stabilization techniques. In this class of techniques the variational form is modified. This approach allows for using identical discrete approximation spaces for both the velocity and the pressure fields. Some of the most popular methods in this framework are Brezzi-Pitkäranta stabilization [18] and SUPG/PSPG/Galerkin-Least Square (GLS) type stabilizations [19–23]. The Brezzi-Pitkaranta formulation is non-consistent – *i.e.*, the problem is (slightly) modified – and only achieves optimal convergence rates for linear approximations. PSPG/GLS stabilization on the other hand is optimally high-order accurate, and fully consistent (provided that the exact solution is sufficiently smooth). However, PSPG/GLS stabilization introduces a quite strong artificial coupling between the velocity and the pressure, and also needs a modification of the right hand side of the system. A later development of PSPG/GLS is the Variational Multiscale Method [24–28]. Prominent alternative techniques that have been developed for fluid problem stabilization are stream functions [29–32], algebraic sub-grid scales [33, 34], fractional step finite elements [35], projection-based stabilization [36, 36–39], and the continuous interior penalty method [40–42]. The continuous interior penalty method is quite different from the other approaches mentioned above in the sense that the stabilization is defined on the skeleton structure of the mesh, instead of element-wise. The methods proposed in this thesis are inspired by this idea.

Although the FEM is very successful in solving incompressible fluid flow problems (and PDEs in general), in practice, the meshing process for complex geometries is commonly experienced to be the bottleneck in a complete analysis cycle [43]. This meshing process includes geometry clean-up procedures, and communication between the CAD design and the polygonal approximation of that geometry in order to *e.g.* refine the FEM mesh. This problem has led to a demand for minimizing the time of this pre-analysis stage. The most prominent candidates to solve this problem are Isogeometric Analysis (IGA) and immersed methods.

1.1.2 Isogeometric analysis

Isogeometric analysis (IGA) was proposed by Hughes *et al.* in 2005 [44] as a framework to reduce the gap between Computer Aided Design (CAD) and Finite Element Analysis (FEA). CAD is extensively used in industry, including the automotive industry, the ship building industry, the aerospace industry, architectural design, prosthetics, and many more. Traditionally, CAD files generated by designers must be transformed into (generally) geometrically approximate meshes before they can be input to FEA codes. This meshing procedure – which includes the geometry clean-up operations in order to apply a tessellation algorithm – is far from trivial, and for complex engineering designs it accounts for the large majority of the complete analysis time. Moreover, the polygonal approximation geometry of the original CAD design potentially leads to solution instabilities (*e.g.*, in imperfection-sensitive problems such as buckling) and reduced analysis accuracy (*e.g.*, in sliding contact problems or boundary layer phenomena). Boundary conditions can become inconsistency by the geometry approximation (*e.g.* the Sapondzhyan—Babuška plate paradox where boundary conditions in the original problem and the geometric limit problem are different [45, 46]). The fundamental idea of IGA is to eliminate the meshing step by directly using the CAD model for the analysis.

Amongst the computational geometry technologies, Non-uniform Rational B-splines (NURBS) are the industry standard [47–50]. NURBS exactly represent conic sections such as circles, cylinders, and spheres. NURBS possess various useful mathematical properties, such as built-in refinement algorithms, point-wise positivity, the convex hull property, and the variation diminishing property in the presence of discontinuous data. A property that has deserved special attention in the context of IGA is the higher-order continuity of NURBS, this in contrast to the C^0-continuity of Lagrange bases employed in the traditional FEM. In IGA the NURBS basis functions inherited from CAD are employed directly for the analysis. For analysis-suitable CAD models, geometrically exact meshing procedures can therefore seamlessly be performed on the coarsest level of the CAD geometry. Refinement, de-refinement, and degree elevation are naturally facilitated by the CAD model.

Over the past decade, isogeometric analysis has been applied in a wide range of research areas, and has been shown to outperform traditional C^0 basis functions in many disciplines, including: solid mechanics [44], structural mechanics [51–57], fluids dynamics [58], fluid-structure-interactions [59–62], electromagnetics [63, 64], magnetohydrodynamics [65], contact mechanics [66–69], shape optimization [70–75], fracture mechanics and phase-field modeling [76–81], free-boundary problems [82], multiscale homogenization problems [83, 84], and many more. We refer to Ref. [43] for an overview of established IGA developments. The most prominent methodological developments to the field of IGA include research on T-splines [85, 86], collocation methods [87–89], boundary-element methods [90, 91], subdivision surfaces [92, 93], approximation properties [94–97], multi-patch coupling techniques [98–101], volume parameterizations [102], domain decomposition techniques [103], local refinement strategies [104–106], splines for unstructured meshes [107, 108], and preconditioning techniques [109–113]. A comprehensive overview of the mathematical perspective on IGA can be found in Ref. [114]. An interesting aspect of IGA is that traditional Gauss quadrature is not economically optimal in the sense that it does not take into account the high continuity across elements. This issue is addressed in Refs. [115, 116], where optimal quadrature rules for IGA are proposed. Also, the classical element-by-element assembly procedure leads to unnecessarily high costs when applied to IGA. This problem can be resolved by applying a row-by-row assembly procedure [117].

Within the context of fluid flow problems – particularly in the incompressible regime – IGA has been applied very successfully. Within the framework of inf-sup stable spaces for mixed formulations [13], the control over inter-element continuity in IGA has enabled the generalization of existing compatible discretization pairs to arbitrary orders and regularities, and the development of novel IGA discretizations, most notably: Taylor-Hood elements [94, 118, 119], Nédélec elements [118], subgrid elements [119, 120], and H(div)-conforming elements [118, 121–123].

One of the open challenges for IGA for fluids, and for IGA in general, is that complex geometries originating from industry usually involve multiple trimming surfaces/curves. These trimmed objects cannot be treated within the conforming IGA framework. In order to facilitate treatment of such objects, the conforming IGA framework can be enriched with immersed simulation technology, which is regarded as the natural analysis equivalent of trimmed geometries in CAD. An additional advantage of immersed IGA is that it allows to deal with large mesh deformations, which typically occur in, for example, fluid-structure interactions and free-boundary problems.

1.1.3 Immersed methods & Immersogeometric analysis

The pivotal idea of immersed methods is to extend a geometrically complex physical domain of interest into a geometrically simple embedding domain, on which a regular mesh can be built easily. There are varieties of techniques in the literature that belong to the class of immersed methods, such as: the immersed boundary method (IBM) by Peskin [124], the immersed finite element methods [125], the immersed interface method [126], the immersed boundary finite volume method [127, 128], the embedded boundary method [129], the Cartesian-grid method [130], the fat-boundary method [131], the XFEM/GFEM/PUFEM [132–134], Web-splines [135], CutFEM [136], and the Finite Cell Method [137]. These methods – and similar techniques that we did not list above – typically differ from each other in one or more of the following aspects: boundary condition imposition, variational formulations, integration of cut-elements, the employed basis functions, the modification of the background approximation spaces, and the approximation of Dirac-delta functions, amongst others.

This thesis focuses on the Finite Cell Method (FCM) introduced by Rank and co-workers in 2007, which is a natural companion to isogeometric analysis. The framework leveraging the advantages of both isogeometric analysis and FCM-type immersed techniques is referred to as immersogeometric analysis. The use of B-spline basis functions within an FCM framework was first considered by Schillinger *et al.* [138–140]. Fig. 1.1 illustrates a difference in the discretization metheology between Isogeometric analysis and Immsersogeometric analysis. On the one hand immersogeometric analysis facilitates consideration of CAD trimming curves in the context of isogeometric analysis. On the other hand, it enables the constructions of high-regularity spline spaces over geometrically and topologically complex volumetric domains, for which analysis-suitable spline parametrizations are generally not available. This approach has been applied to various problems in solid and structural mechanics (see [141] for a review), in image-based analysis [142, 143], in fluid-structure interaction problems [144, 145] (the term "immersogeometric analysis" was coined in this context), and in various other application areas.

When considering immersed methods for fluid problems, due to the existence+ of cut elements, the stability aspects related to the *inf-sup* condition from the incompressibility constraint, along with the treatment of conditioning issues are of crucial importance. In the context of the FEM, there are various approaches addressing those issues. For the conditioning, one of the most successful remedies is the Ghost-penalty stabilization proposed by Burman [146]. In the Ghost-penalty approach, the original variational form is augmented with a least-squares term controlling the (high-order) jumps of the derivatives of variables over element interfaces located near cut boundaries. The background approximation basis functions are kept unchanged. The work in this thesis is also inspired by this idea. This is different from approaches where basis functions are modified [135], or from preconditioning algorithms [147]. Another noteworthy treatment is proposed in [148] under the name Stable Generalized Finite Element Method (SGFEM), the pivotal idea of which is to modify solution space enrichment functions to improve conditioning. For the *inf-sup* stability, similar aspects have been studied in the context of, e.g., XFEM and CutFEM [149–153]. .

Although immersed FEM for fluids is a mature field of research – in which the most important aspects have been studied in detail – extension of these developments to the immersogeometric setting is a new and active area of research. A contribution in this direction of research that is particularly noteworthy is the work of Hsu and co-workers [144, 154, 155], which demon-

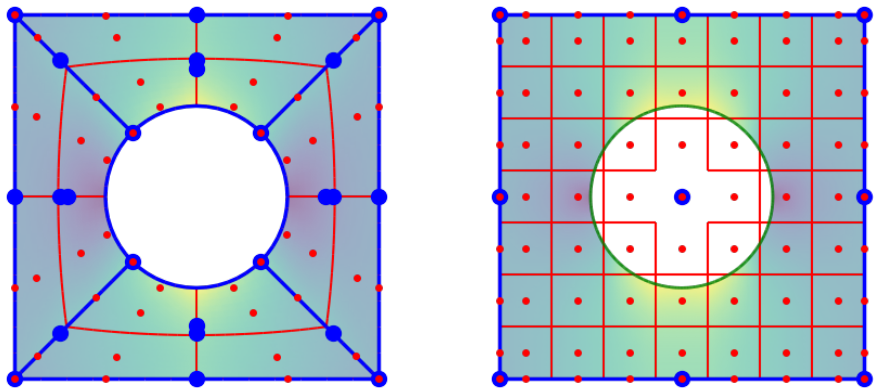

(a) Isogeometric analysis **(b)** Immersogeometric analysis

Fig. 1.1: Comparison of the computation of a horizontal potential flow along a cylinder using *(a)* conforming isogeometric analysis, and *(b)* immersogeometric analysis (the background color represents the flow speed). In the conforming IGA setting of sub-figure *(a)* the domain is parametrized using four NURBS patches, whose boundaries are indicated by the blue lines. The corresponding control points – with varying weights – are indicated by the blue circles. For the analysis a single uniform refinement of the geometric model is performed. The element boundaries and associated control points - which are directly associated with the NURBS basis functions used for the analysis – are marked in red. In the immersed IGA setting of sub-figure *(b)* the domain is parametrized by a single rectangular B-spline patch, whose borders and control points are indicated in blue. The circular exclusion is geometrically modeled by means of a trimming curve, which is printed in green. A refined B-spline patch is used for the analysis, the elements and control points of which are indicated in red. Note that the elements that do not intersect the domain are discarded. For the mesh shown here all (quadratic) B-spline shape functions have support on the computational domain, as a consequence of which all (red) computational control points are maintained.

strates the potential of immersogeometric analysis to solve highly complex problems in engineering and biomechanics. The full potential of immersogeometric analysis for fluid flow problems (in particular the IGA version of the FCM), however, remains to be unlocked. The work in this thesis contributes to unlocking this potential.

1.2 Aims & scope

The main goal of this dissertation is to develop a robust simulation strategy for incompressible flow problems based on the isogeometric and immersogeometric analysis frameworks. The developed simulation strategy should not compromise the key idea of IGA that simulations can be performed directly on the CAD geometry, so that the developments herein improve typical design-through-analysis workflows for CFD problems. To accomplish our primary goal, we identify the following objectives:

1. We first aim at investigating the complications related to the usage of isogeometric inf-sup stable elements in an immersed settings. Our goal is to clarify the conditions under which the performance of inf-sup stable elements for immersogeometric analysis deteriorates compared to the conforming isogeometric setting, and to identify the underlying causes of this deterioration.
2. Based on the results pertaining to the first objective we wish to develop an alternative numerical method that rigorously resolves the identified complications. We aim at providing detailed insights into the performance of this novel approach by considering a wide range of benchmark problems. These insights do not only encompass accuracy and stability aspects, but also implementation and analysis workflow aspects.

We shall focus our scope on incompressible fluid flows, in particular the steady Stokes equations and the steady and unsteady Navier-Stokes equations. To focus on inf-sup stability aspects we consider problems with moderate Reynolds numbers, thereby excluding convection-dominated flow problems. Although the developments in this thesis are conducted within a mathematically rational framework, we note that a stability proof for the developed simulation framework is beyond the scope of this work. This thesis is outlined as follows:

In Chapter 2, we study the applicability of conforming isogeometric *inf-sup* stable velocity-pressure pairs to immersogeometric analysis. We consider the most prominent pairs, *viz.*, Taylor-Hood elements, Sub-grid elements, Raviart-Thomas elements, and Nédélec elements. To understand the performance of these element families in an immersed settings, we study their behavior for the prototypical problem of steady Stokes flow in a quarter annulus ring. We present numerical result that convey that all isogeometric element families exhibit local oscillations in the pressure field near cut boundaries. The occurrence of such oscillations on cut elements with relatively large volume fractions implies that this problem is related to the inf-sup stability of the discrete problem, rather than to conditioning issues related to cut elements with small volume fractions. We conclude that off the shelf usage of isogeometric inf-sup stable pairs in an immersed setting deteriorates the stability properties of these elements, which motivates us to explore alternative stabilization techniques.

In Chapter 3 we propose a novel skeleton-based stabilization technique to circumvent the *inf-sup* stability condition for mixed problems. Since this stabilization technique is not specific to the immersed setting, in this chapter we introduce it in the conforming isogeometric setting (the extension to the immersed setting is discussed in Chapter 4). The pivotal idea of the method that we propose is the introduction of a penalty term that controls the jump of high-order derivatives of the pressure field over the skeleton structure of the mesh, which allows utilization of identical discrete spaces for the velocity and pressure fields. This method – which to the best of our knowledge is new in the context of mesh-conforming isogeometric analysis – can be considered as a high-regularity extension of the (Continuous) Interior Penalty methods, making it applicable to a broad class of spline discretizations with arbitrary continuity conditions across element interfaces. We study the performance of the proposed formulation for a range of Stokes flow and steady and unsteady Navier-Stokes flow benchmark cases at moderate Reynolds number, including the case of a multi-patch NURBS-based isogeometric analysis. We observe that the skeleton-based stabilization method yields solutions free of spurious oscillations, and yields optimal rates of convergence under mesh refinements. We observe excellent results for a large range of stabilization parameters in the conforming IGA setting, which is a precursor for successful extension of the stabilization method to the immersed setting.

In Chapter 4 we extend the stabilization technique of Chapter 3 to the case of immersogeometric analysis of incompressible flow problems. We consider immersogeometric analysis using identical maximum regularity spline spaces for the pressure and the velocity. We treat the *inf-sup* instability of the pressure field and the conditioning issue related to small cut-elements in the same fashion, *viz.* by minimizing the jump of highest-order derivatives of the field variables over the element interfaces. We apply the pressure skeleton-stabilization term proposed in Chapter 3 to the immersed setting in unaltered form, and supplement the formulation with a Ghost-penalty stabilization term to treat the cut-element conditioning issue. We observe that the method obtains oscillation-free solutions, also in the vicinity of immersed boundaries. The formulation yields high-order optimal convergence rates under mesh refinements. To demonstrate the stability and robustness of the method, we apply the proposed formulation to the simulation of fluid flow in a porous medium, the geometry of which is directly extracted from 3D μCT scan data [143].

Chapter 2

Mixed Isogeometric Finite Cell Methods for the Stokes problem

Abstract

We study the application of the Isogeometric Finite Cell Method (IGA-FCM) to mixed formulations in the context of the Stokes problem. We investigate the performance of the IGA-FCM when utilizing some isogeometric mixed finite elements, namely: Taylor-Hood, Sub-grid, Raviart-Thomas, and Nédélec elements. These element families have been demonstrated to perform well in the case of conforming meshes, but their applicability in the cut-cell context is still unclear. Dirichlet boundary conditions are imposed by Nitsche's method. Numerical test problems are performed, with a detailed study of the discrete inf-sup stability constants and of the convergence behavior under uniform mesh refinement.

Reproduced from: T. Hoang, C.V. Verhoosel, F. Auricchio, E.H. van Brummelen, A. Reali, *Mixed Isogeometric Finite Cell Methods for the Stokes problem*, Computer Methods in Applied Mechanics and Engineering, Volume 316, 2017, Pages 400-423, DOI: 10.1016/j.cma.2016.07.027

2.1 Introduction

Isogeometric analysis (IGA) was proposed in [44] as a framework to reduce the gap between Computer Aided Design (CAD) and Finite Element Analysis (FEA). The fundamental idea of IGA is to employ the same basis functions to describe both the geometry of the domain of interest and the field variables. In contrast to conventional FEA which typically uses Lagrange polynomials as basis functions, IGA utilizes basis functions inherited from CAD modeling such as B-splines and NURBS. For analysis-suitable CAD models, geometrically exact meshing procedures can seamlessly be performed on the coarsest level of the CAD geometry. Splines provide a flexible way for refinement, de-refinement, and degree elevation. Furthermore, splines allow one to achieve higher-order continuity, this in contrast to the C^0-continuity provided by the traditional FEM. Isogeometric analysis has been applied in a wide range of application areas, from solid and structures, to fluids, and multi-physics modeling; see [43] for an overview of established IGA developments. More recent contributions to the field of IGA include research on T-splines [85, 86], collocation methods [87–89], multi-patch coupling techniques [54, 98–100], local refinement strategies [104–106], and many more. A review of the mathematical foundation of isogeometric methods can be found in [114].

Recently, the advantages of the high order basis functions in isogeometric analysis have been combined with the topological flexibility of the finite cell method (FCM). The FCM in its original form was introduced by Rank and co-workers [137, 156], and belongs to a larger class of methods for which the domain boundaries do not align with the meshes (e.g., embedded domain methods, immersed boundary methods, fictitious domain methods, see [157–159]). The main idea is to extend the physical domain of interest with complexly-shaped boundaries into a larger embedding domain of simple/regular geometry, where a mesh and approximation space can be built more easily. The exploitation of this concept in the context of isogeometric analysis was first considered by Schillinger et al. [138–140]. This approach has been successfully applied to various problems in solid and structural mechanics (see [141] for a review), in image-based analysis [142, 143], in fluid-structure interaction problems [144, 145], and in many other application areas.

In this work, we investigate the capability of the isogeometric-based finite cell method (IGA-FCM) for solving Stokes-flow problems. When discretizing the Stokes problem, the velocity and pressure spaces cannot be chosen arbitrarily. In order to obtain a discretization which is free of locking and spurious oscillations, this pair of spaces needs to satify the inf-sup (or LBB) condition [5–7, 13]. In the context of IGA, the flexibility of B-splines on structured meshes allows one to construct inf-sup stable velocity and pressure spaces with arbitrary orders, and with different regularities. Herein we study the performance of the IGA-FCM in the context of mixed formulations utilizing four important families of isogeometric mixed elements, viz. Taylor-Hood [94, 118, 119], Sub-grid [119, 120], Nédélec [118], and Raviart-Thomas [118, 121] elements. These isogeometric element families have been demonstrated to perform well in the case of conforming meshes. However, in the cut-cell context their applicability is still not clear. Therefore, we present a detailed numerical study and comparison of these element families in terms of: *i)* discrete inf-sup constants, and *ii)* convergence behavior of the errors under uniform mesh refinements. This investigation provides valuable insights into the capabilities of these element families for mixed form FCM problems in general, and complements the recent advances on the application of (IGA-)FCM to flow problems [144, 154, 160, 161].

The structure of this paper is as follows: Section 2 states the Stokes problem with Nitsche's method and discusses its well-posedness. Section 3 presents a concise introduction to the IGA-FCM with mixed formulations, and discusses in detail some of the related computational aspects. Section 4 presents the above-mentioned pairs of mixed spaces which are then numerically investigated in Section 5. Conclusions are finally drawn in Section 6.

2.2 Problem formulation

Our investigation of the properties of IGA-FCM for mixed problems will be presented in the context of the Stokes equations. The Stokes equations are the archetypal model problems for mixed formulations, representative of incompressible creeping flow and incompressible linear elasticity [13]. In this work, we will restrict ourselves to two-dimensional problems. However, most results extend mutatis mutandis to three dimensions.

2.2.1 Stokes problem

Let Ω be an open bounded domain in $\mathbb{R}^2$ with Lipschitz boundary $\partial\Omega$. We assume that $\partial\Omega$ is composed of two complementary open subsets Γ_D and Γ_N, i.e., $\partial\Omega = \overline{\Gamma_D} \cup \overline{\Gamma_N}$ and $\Gamma_D \cap \Gamma_N = \emptyset$. The steady Stokes problem is given by

$$\begin{cases} -\nabla \cdot (2\mu\nabla^s \mathbf{u}) + \nabla p = \mathbf{f} & \text{in } \Omega \\ \nabla \cdot \mathbf{u} = 0 & \text{in } \Omega \\ \mathbf{u} = \mathbf{g} & \text{on } \Gamma_D \\ 2\mu\nabla^s\mathbf{u} \cdot \mathbf{n} - p\mathbf{n} = \mathbf{h} & \text{on } \Gamma_N \end{cases} \tag{2.1}$$

where the body force $\mathbf{f} : \Omega \to \mathbb{R}^2$, the Dirichlet data $\mathbf{g} : \Gamma_D \to \mathbb{R}^2$, and the Neumann data $\mathbf{h} : \Gamma_N \to \mathbb{R}^2$ are exogeneous data. The exterior unit normal vector to $\partial\Omega$ is denoted by $\mathbf{n}$, and $\nabla^s\mathbf{u} := \frac{1}{2}\left(\nabla\mathbf{u} + (\nabla\mathbf{u})^T\right)$ is the symmetric gradient of $\mathbf{u}$.
In a creeping-flow context, μ represents the kinematic viscosity, and $\mathbf{u}$ and p indicate fluid velocity and pressure, respectively. In the context of incompressible linear elasticity, μ stands for the shear modulus, and $\mathbf{u}$ and p respectively represent the displacement and pressure-like fields.

The weak formulation of (2.1) reads:

Find $(\mathbf{u}, p) \in \mathbf{V}_{g,\Gamma_D} \times Q$ *such that*

$$\begin{aligned} 2\mu \int_\Omega \nabla^s\mathbf{u} : \nabla^s\mathbf{w}\, \mathrm{d}\Omega - \int_\Omega p\, \mathrm{div}\mathbf{w}\, \mathrm{d}\Omega &= \int_\Omega \mathbf{f}\cdot\mathbf{w}\, \mathrm{d}\Omega + \int_{\Gamma_N} \mathbf{h}\cdot\mathbf{w}\, \mathrm{d}\Gamma \quad && \forall \mathbf{w} \in \mathbf{V}_{0,\Gamma_D}, \\ -\int_\Omega q\, \mathrm{div}\mathbf{u}\, \mathrm{d}\Omega &= 0 && \forall q \in Q, \end{aligned} \tag{2.2}$$

where the function spaces are defined as

$$\mathbf{V}_{g,\Gamma_D} := \left\{\mathbf{u} \in [H^1(\Omega)]^2 : \mathbf{u} = \mathbf{g} \text{ on } \Gamma_D\right\}, \qquad Q := L^2(\Omega)$$

Here $H^1(\Omega)$ denotes the usual Sobolev space of square-integrable functions with square integrable weak derivatives. In the case of pure Dirichlet boundary conditions, i.e., if Γ_D coincides with all of $\partial\Omega$, the pressure is determined up to a constant. Therefore, in that case, we will supplement the system with the zero average pressure condition

$$Q := L^2_0(\Omega) \equiv \left\{q \in L^2(\Omega) : \int_\Omega q\, \mathrm{d}\Omega = 0\right\}.$$

2.2.2 Nitsche's method for Dirichlet boundary conditions

In (2.2), Dirichlet boundary conditions are imposed strongly, i.e., they are incorporated into the function space as $\mathbf{V}_{g,\Gamma_D}$. Standard finite-element approximations of (2.1) are based on conforming subspace approximations, which implies that the finite-element approximation space is subject to the same Dirichlet boundary conditions as $\mathbf{V}_{g,\Gamma_D}$. In the immersed-boundary setting considered in this work, such a strong enforcement of boundary conditions is intractable. One way to bypass this issue is to impose Dirichlet boundary conditions in a weak sense. Common approaches are (see, e.g., [162]): penalty methods, Lagrange multipliers, or Nitsche's method. In this work, Nitsche's method [163] is favored because it preserves consistency, symmetry, ellipticity, and it extends directly to high-order finite-element approximations.

To provide a setting for the Galerkin finite-element approximation of (2.2) with weakly-enforced boundary conditions via Nitsche's method, we first introduce a rectangular ambient domain $\mathcal{A} \supset \Omega$ that encompasses the physical domain Ω; see Fig. 4.4. We cover $\mathcal{A}$ with a uniform mesh $\mathcal{T}^h_{\mathcal{A}}$ composed of rectangular open element domains with diameter $h > 0$. We denote by $\mathcal{T}^h$ the corresponding mesh on Ω,

$$\mathcal{T}^h = \left\{\kappa \subset \Omega : \kappa = k \cap \Omega,\ k \in \mathcal{T}^h_{\mathcal{A}}\right\}$$

and by $\mathcal{E}^h$ the corresponding set of boundary edges,

$$\mathcal{E}^h = \left\{e \subset \partial\Omega : e = \operatorname{int}(\partial\kappa \cap \partial\Omega),\ \kappa \in \mathcal{T}^h\right\}$$

where $\operatorname{int}(\cdot)$ denotes the interior of set $(\cdot)$. In particular, $\mathcal{E}^h_D$ designates the boundary mesh that covers the Dirichlet boundary, Γ_D. The mesh $\mathcal{T}^h_{\mathcal{A}}$ serves as a support structure for a pair of regular finite-element or isogeometric approximation spaces. The restrictions of these approximation spaces to the physical domain in turn provide the approximation spaces $\mathbf{V}^h \subset [H^1(\Omega)]^2$ for the velocity approximation and $Q^h \subset Q$ for the pressure approximation.

Weak enforcement of Dirichlet boundary conditions via Nitsche's method relies on a stabilization term that is proportional to the reciprocal length of boundary edges. To define the Nitsche stabilization term, for each boundary edge $e \in \mathcal{E}^h$ we denote by h_e its length. Alternatively, h_e can be defined as $h_e := \sqrt{\operatorname{area}(\kappa_e)}$ where κ_e is the element connected to the boundary edge e, and $\operatorname{area}(\kappa_e)$ is its area. The two definitions of h_e are equivalent for shape-regular meshes, in the sense that for shape-regular meshes there exist (moderate) constants $\overline{c} \geq \underline{c} > 0$ such that $\underline{c}\,\operatorname{length}(e) \leq \sqrt{\operatorname{area}(\kappa_e)} \leq \overline{c}\,\operatorname{length}(e)$.

The discretized problem with Nitsche's weak enforcement of Dirichlet boundary conditions can be cast into the form:

Find $(\mathbf{u}^h, p^h) \in \mathbf{V}^h \times Q^h$ *such that*

$$
\begin{aligned}
a^h(\mathbf{u}^h, \mathbf{v}^h) + b(p^h, \mathbf{v}^h) &= l_1^h(\mathbf{v}^h) \quad \forall \mathbf{v}^h \in \mathbf{V}^h, \\
b(q^h, \mathbf{u}^h) &= l_2(q^h) \quad \forall q^h \in Q^h,
\end{aligned}
\tag{2.3}
$$

where

$$
\begin{aligned}
a^h(\mathbf{u}^h, \mathbf{v}^h) &= 2\mu\bigg(\int_\Omega \nabla^s \mathbf{u}^h : \nabla^s \mathbf{v}^h \,\mathrm{d}\Omega - \int_{\Gamma_D} (\nabla^s \mathbf{u}^h \cdot \mathbf{n}) \cdot \mathbf{v}^h \,\mathrm{d}\Gamma \\
&\qquad - \int_{\Gamma_D} (\nabla^s \mathbf{v}^h \cdot \mathbf{n}) \cdot \mathbf{u}^h \,\mathrm{d}\Gamma \bigg) + \mu \sum_{e \in \mathcal{E}_D^h} \int_e \frac{\beta}{h_e} \mathbf{u}^h \cdot \mathbf{v}^h \,\mathrm{d}\Gamma \\
b(q^h, \mathbf{v}^h) &= -\int_\Omega q^h \,\mathrm{div}\mathbf{v}^h \,\mathrm{d}\Omega + \int_{\Gamma_D} q^h \,\mathbf{n} \cdot \mathbf{v}^h \,\mathrm{d}\Gamma \\
l_1^h(\mathbf{v}^h) &= \int_{\Omega_\alpha} \mathbf{f} \cdot \mathbf{v}^h \,\mathrm{d}\Omega + \int_{\Gamma_N} \mathbf{h} \cdot \mathbf{v}^h \,\mathrm{d}\Gamma - 2\mu \int_{\Gamma_D} (\nabla^s \mathbf{v}^h \cdot \mathbf{n}) \cdot \mathbf{g} \,\mathrm{d}\Gamma \\
&\qquad + \mu \sum_{e \in \mathcal{E}_D^h} \int_e \frac{\beta}{h_e} \mathbf{g} \cdot \mathbf{v}^h \,\mathrm{d}\Gamma \\
l_2(q^h) &= \int_{\Gamma_D} q^h \,\mathbf{n} \cdot \mathbf{g} \,\mathrm{d}\Gamma
\end{aligned}
\tag{2.4}
$$

in which $\beta > 0$ is a suitable stabilization parameter. In the bilinear form a^h, the second term in parenthesis is the consistency term. The third term is the symmetric consistency term, which is added to preserve the symmetry of a^h and, correspondingly, to retain consistency of the dual bilinear form. The ultimate term associated with the β parameter is referred to as the stabilization term and serves to ensure stability.

The stabilization parameter β can be set uniformly for all edges or it can be determined locally for each edge by solving an associated local eigenvalue problem; see [164, 165]. In our numerical experiments in Section 2.5, we select β as a uniform global constant. We note that if the stabilization parameter is selected appropriately, i.e., large enough to retain stability but not so large to cause ill-conditioning, the observed differences in the results are negligible. The two distinct definitions of h_e, i.e., as length(e) or as $\sqrt{\mathrm{area}(\kappa_e)}$, then generally also lead to negligible differences in the observations. Sensitivity of the results to the stabilization parameter β and to the definition of h_e can however emerge if irregular (e.g., sliver-type) cut elements occur.

It is to be noted that the condition $b(q^h, \mathbf{v}^h) = 0$ in combination with $Q^h \supseteq \mathrm{div}\mathbf{V}^h$ does not generally imply $\mathrm{div}\mathbf{v}^h = 0$ on account of the additional term $\int_{\Gamma_D} q^h \, \mathbf{n} \cdot \mathbf{v}^h \, \mathrm{d}\Gamma$ in the bilinear form b. This additional term emerges from the weak imposition of Dirichlet boundary conditions via Nitsche's method. Indeed, if the Dirichlet boundary conditions are strongly imposed and incorporated in $\mathbf{V}^h$, then $\mathbf{n} \cdot \mathbf{v}^h = 0$ on Γ_D and the additional term vanishes.

2.2.3 *Well-posedness: continuity and inf-sup conditions*

To establish conditions for well-posedness of the saddle-point problem (2.3), we introduce the norms:

$$\|\mathbf{v}\|^2_{\mathbf{V}^h} := \|\nabla \mathbf{v}\|^2_{L^2(\Omega)} + \sum_{e \in \mathcal{E}^h_D} \frac{\nu}{h_e} \|\mathbf{v}\|^2_{L^2(e)}, \qquad \|q\|^2_{Q^h} := \|q\|^2_{L^2(\Omega)} \tag{2.5}$$

for some positive constant $\nu \in \mathbb{R}_{>0}$. Problem (2.3) is well-posed if and only if the following conditions hold [6, 13]:

- Continuity of a^h and b:

$$\exists C_a \in \mathbb{R}_{>0} : \qquad a^h(\mathbf{u}^h, \mathbf{v}^h) \leq C_a \big\|\mathbf{u}^h\big\|_{\mathbf{V}^h} \big\|\mathbf{v}^h\big\|_{\mathbf{V}^h} \qquad \forall (\mathbf{u}^h, \mathbf{v}^h) \in \mathbf{V}^h \times \mathbf{V}^h \tag{2.6}$$

$$\exists C_b \in \mathbb{R}_{>0} : \qquad b(q^h, \mathbf{v}^h) \leq C_b \big\|q^h\big\|_{Q^h} \big\|\mathbf{v}^h\big\|_{\mathbf{V}^h} \qquad \forall (q^h, \mathbf{v}^h) \in Q^h \times \mathbf{V}^h \tag{2.7}$$

- Weak coercivity of a^h on the kernel of b:

$$\exists \alpha \in \mathbb{R}_{>0} : \inf_{\mathbf{u}^h \in \mathbf{Z}^h \setminus \{\mathbf{0}\}} \sup_{\mathbf{v}^h \in \mathbf{Z}^h \setminus \{\mathbf{0}\}} \frac{a^h(\mathbf{u}^h, \mathbf{v}^h)}{\big\|\mathbf{u}^h\big\|_{\mathbf{V}^h} \big\|\mathbf{v}^h\big\|_{\mathbf{V}^h}} \geq \alpha \tag{2.8}$$

  with

$$\mathbf{Z}^h := \left\{ \mathbf{v}^h \in \mathbf{V}^h : b(q^h, \mathbf{v}^h) = 0, \ \forall q^h \in Q^h \right\}$$

- Inf-sup condition on b:

$$\exists \gamma \in \mathbb{R}_{>0} : \inf_{q^h \in Q^h \setminus \{0\}} \sup_{\mathbf{v}^h \in \mathbf{V}^h \setminus \{\mathbf{0}\}} \frac{b(q^h, \mathbf{v}^h)}{\big\|q^h\big\|_{Q^h} \big\|\mathbf{v}^h\big\|_{\mathbf{V}^h}} =: \gamma^h \geq \gamma \tag{2.9}$$

The mesh-dependent term in the norm for the velocity space in (2.5) is required for continuity of the bilinear form a^h according to (2.6) with respect to the $\|\cdot\|_{\mathbf{V}^h}$-norm. Indeed, the Cauchy-Schwarz inequality in combination with a standard discrete trace inequality (see, e.g., [166, Lemma 1.44] or [167]) conveys:

$$\left|\int_{\Gamma_D} (\nabla^s \mathbf{u}^h \cdot \mathbf{n}) \cdot \mathbf{v}^h \, \mathrm{d}\Gamma\right| \leq \sum_{e\in\mathcal{E}_D^h} \|\nabla^s \mathbf{u}^h\|_{L^2(e)} \|\mathbf{v}^h\|_{L^2(e)} \leq \sum_{e\in\mathcal{E}_D^h} \frac{C_{\mathrm{tr},e}}{\sqrt{h_e}} \|\nabla \mathbf{u}^h\|_{L^2(\kappa_e)} \|\mathbf{v}^h\|_{L^2(e)}$$
$$\leq \frac{C_{\mathrm{tr}}}{\sqrt{\nu}} \left(\sum_{e\in\mathcal{E}_D^h} \|\nabla \mathbf{u}^h\|^2_{L^2(\kappa_e)}\right)^{1/2} \left(\sum_{e\in\mathcal{E}_D^h} \frac{\nu}{h_e} \|\mathbf{v}^h\|^2_{L^2(e)}\right)^{1/2} \leq \frac{C_{\mathrm{tr}}}{\sqrt{\nu}} \|\mathbf{u}^h\|_{\mathbf{V}^h} \|\mathbf{v}^h\|_{\mathbf{V}^h} \quad (2.10)$$

for certain edge-wise positive constants $C_{\mathrm{tr},e} \in \mathbb{R}_{>0}$, dependent on the shape of κ_e but independent of h_e, and $C_{\mathrm{tr}} = \max\{C_{\mathrm{tr},e} : e \in \mathcal{E}_D^h\}$. From (2.10) one can infer that a^h is bounded and coercive on $\mathbf{V}^h$ for appropriate choices of β and ν. Equation (2.6) follows directly from (2.10) for appropriate β and ν. The continuity condition on b (2.7) is also satisfied for the norms in (2.5). The coercivity of the bilinear form $a^h : \mathbf{V}^h \times \mathbf{V}^h \to \mathbb{R}$ transfers to the subspace $\mathbf{Z}^h \subset \mathbf{V}^h$, which implies (2.8).

The inf-sup condition on b in (2.9) is generally more subtle and requires a suitable choice of the approximation-space pair $(\mathbf{V}^h, Q^h)$. In the context of IGA, stable pairs $(\mathbf{V}^h, Q^h)$ have been studied in, e.g., [94, 118–120]. These IGA velocity-pressure pairs will be discussed in section (2.4.2) before considering their extension to the finite-cell setting. The discrete inf-sup constant γ^h in (2.9) can be computed explicitly based on the algebraic representation of (2.3); see Section 3.4.2.

Remark 2.1. With a minor modification, system (2.3) is also representative of compressible elasticity problems:

$$\boxed{\begin{array}{l}\text{Find } (\mathbf{u}^h, p^h) \in \mathbf{V}^h \times Q^h \text{ such that} \\[1ex] \qquad \begin{aligned} a^h(\mathbf{u}^h, \mathbf{v}^h) + b(p^h, \mathbf{v}^h) &= l_1^h(\mathbf{v}^h) \quad \forall \mathbf{v}^h \in \mathbf{V}^h, \\ b(q^h, \mathbf{u}^h) - \tfrac{1}{\lambda} c(q^h, p^h) &= l_2(q^h) \quad \forall q^h \in Q^h, \end{aligned} \end{array}} \quad (2.11)$$

where μ, λ are the first and second Lamé parameters, respectively, $\mathbf{u}^h$ is the displacement field, $p = -\lambda \mathrm{div}\mathbf{u}$ represents the pressure-like field, and $c(p,q) = \int_\Omega pq \, \mathrm{d}\Omega$. For well-posedness of the problem in the nearly incompressible limit $\lambda/\mu \gg 1$, it is important that the inf-sup condition of (2.9) holds also in this case; see, e.g., [13].

2.3 Mixed formulation of the Finite Cell Method

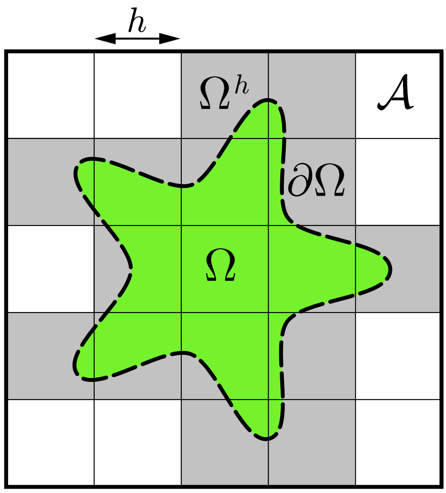

Fig. 2.1: Setup of the FCM: The physical domain Ω is embedded into an ambient domain $\mathcal{A}$. The ambient domain is divided into cells, which serve as a support structure for a FEM or IGA approximation space. Cells that do not intersect the physical domain are discarded (white). Cells that do intersect the physical domain form a discrete embedding domain Ω^h (grey).

The Finite Cell Method (FCM) was introduced by Rank and coworkers in [156]. In its original form, the FCM combines three concepts: the fictitious domain method, the p-version FEM, and an adaptive integration technique for cut cells. In this section, we first discuss the fundamental ideas of the FCM along with its volume and boundary integration procedures. We then present the algebraic form of the FCM for mixed formulations.

2.3.1 Basic setup of the Finite Cell Method

In the FCM the physical domain is embedded into a fictitious (or *embedding* or *ambient*) domain $\mathcal{A}$ with simple – typically rectangular – geometry; cf. Fig. 4.4. This extended domain is covered by a collection $\mathcal{T}_{\mathcal{A}}^h$ of cells of regular shape, where the affix $h > 0$ indicates a resolution parameter, e.g., $h = \max\{\text{diam}(\kappa) : \kappa \in \mathcal{T}_{\mathcal{A}}^h\}$. Cells that do not intersect the physical domain are discarded, and the remaining cells serve as a support structure for basis functions in a similar manner as the elements in FEM. The remaining cells form a discrete embedding domain,

$$\Omega^h := \{\overline{\cup \kappa} : \kappa \in \mathcal{T}^h_{\mathcal{A}},\ \kappa \cap \Omega \neq \emptyset\};$$

see Fig. 4.4. The FCM provides a formulation for the numerical approximation of the problem under consideration on the physical domain Ω and its extension onto the discrete embedding domain Ω^h. Significance is assigned only to the discrete approximation on Ω. While the general computational scheme is similar to standard FEM, essential boundary conditions are typically weakly enforced in the FCM. This weak enforcement is most commonly based on Nitsche's method [163], which circumvents the indeterminate behavior of the approximation space along the – in principle arbitrary shaped – domain boundary $\partial\Omega$.

To mitigate conditioning problems related to the occurence of cut cells with small volume fractions, in the FCM it is common practice to assign a (very small) virtual "stiffness" to the exterior of the domain [168]. This extension of the problem onto the exterior $\Omega^h \setminus \Omega$ generally leads to inconsistency of the formulation, which in some cases can affect the behavior of mixed elements. Therefore, we do not use a virtual "stiffness" in this work, but instead we use a Jacobi preconditioner to avoid ill-conditioning problems [147].

2.3.2 Computation of volume integrals

By virtue of the fact that the FCM formulation is restricted to the physical domain, Ω, the integrands to be evaluated over cells that are intersected by the boundary, $\partial\Omega$, are generally discontinuous. Accordingly, standard quadrature rules yield inadequate accuracy on cut cells. The FCM is therefore generally complemented with an adaptive numerical-integration technique.

Herein we employ the commonly used multi-level integration scheme based on recursive bi-sectioning [139]. While cells that are completly within the physical domain are integrated using standard quadrature rules, an adaptive integration technique is used for cut cells. This technique subdivides each cut cell into four uniform subcells and this subdivision process is continued recursively, i.e., the subcells which are intersected by the boundary are again partitioned into four uniform subcells. This process is repeated until a prescribed recursion depth $k \in \mathbb{Z}_{\geq 0}$ has been reached. On this deepest level of

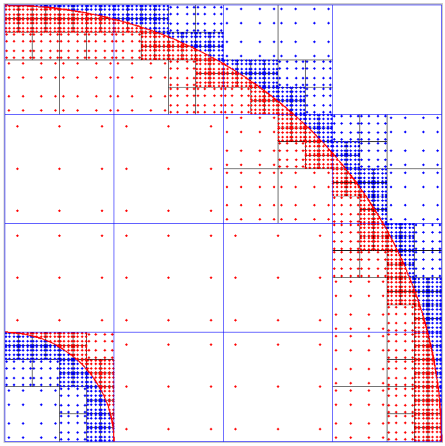

Fig. 2.2: Illustration of the FCM discretization along with Gauss point distribution for a quarter annulus. Red points are located inside the physical domain and blue points are outside the physical domain. In this example, the refinement depth is equal to 4.

recusion, quadrature points exterior to Ω are discarded. The resulting recursive bi-sectioning process exhibits a quadtree structure in 2D and an octree structure in 3D. The detection of subcell boundary intersections is based on performing an inside-outside check of the subcell vertices on each level of the recursion. We note that for the analytical geometries considered herein the employed top-down approach robustly controls the integration accuracy. For arbitrary geometries this top-down recursion can halt prematurely, leading to geometric inaccuracies [169]. A bottom-up approach can in such cases be employed to retain geometric precision.

In this work we use B-spline basis functions in combination with the aforementioned adaptive integration technique. The integrals in each (sub)cell are evaluated with $p+1$ Gauss quadrature points in each direction. The recursion depth is selected such that the integration error is negligible compared to the discretization error. For higher-order approximations, this implies that the required integration depth generally increases rapidly as the mesh is refined, typically proportional to h^{1-p} where p indicates the order of accuracy of the considered FEM or IGA space (in the energy norm). Although no new degrees of freedom are introduced as the integration depth increases, the computational cost related to the integration of cut cells does increase significantly.

This increase in computational effort can be ameliorated by means of recent, more advanced cut-cell integration techniques, e.g., [143, 170–172].

2.3.3 Computation of boundary integrals

When the FCM is used in combination with IGA, the boundaries of the domain are usually represented by spline curves (in 2D) or spline surfaces (in 3D). These parametrized curves or surfaces can then be used directly for the evaluation of boundary integrals.

To determine the boundary integrals in (2.4), notably, the contribution of the Dirichlet boundary to all functionals and the contribution of the Neumann boundary to l_1^h, we assume that a parametrization of the boundary is available. As illustrated in Fig. 2.3 the intersections of the boundary with the background mesh $\mathcal{T}_{\mathcal{A}}^h$ are located. In this way, the boundary is partitioned into a set of (curved) edge elements, $\mathcal{E}^h$. Each of these edge elements inherits its parameterization from the underlying parameterization of the boundary. For simple boundary geometries, such as lines, circles or conic sections, this step can be efficiently performed, especially in 2D, by virtue of the regularity of the the background mesh. By assigning quadrature points to the edge elements, the boundary integrals can be evaluated. In this work we employ $p + 1$ Gauss points for the edge elements.

In case of complex geometries, one can linearize or approximate the boundary with a more simple/regular parameterization before computing the intersection with the mesh. Alternatively, following [143], an accurate approximation to the boundary can be obtained by connecting the intersection points of the boundary with the integration subgrid, viz. the highest level of bisectioning used in the integration procedure. The latter procedure is also particularly useful if a parametrization of the boundary is not available, e.g., if the boundary is described by means of a level-set function.

2.3.4 Matrix form of the mixed finite cell method

Suppose that $\{\mathbf{N}_i^u\}_{i=1}^{n_u}$ and $\{N_i^p\}_{i=1}^{n_p}$ are basis functions of the finite dimensional velocity space $\mathbf{V}^h$ and pressure space Q^h, respectively, i.e., $\mathbf{V}^h = \mathrm{span}\{\mathbf{N}_i^u\}_{i=1}^{n_u}$, and $Q^h = \mathrm{span}\{N_i^p\}_{i=1}^{n_p}$. These basis functions can be constructed by using

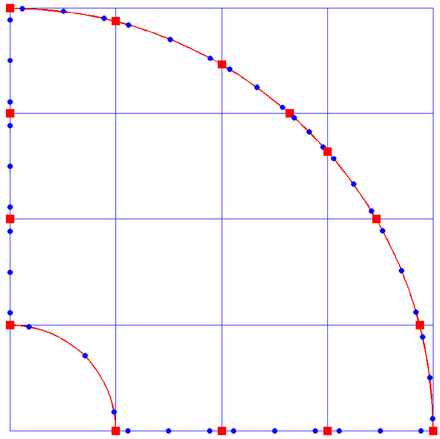

Fig. 2.3: An illustration of the boundary integration for a quarter annulus (here, $p = 2$). Red squares correspond to intersection points, while blue circles correspond to integration points.

finite element technology, isogeometric analysis (e.g., B-spline, NURBS), or possibly with (local) adaptivity [140]. A detailed review can be found in [141].

The approximate velocity $\mathbf{u}^h$ and pressure p^h are then written as

$$\mathbf{u}^h(\mathbf{x}) = \sum_{i=1}^{n_u} \mathbf{N}_i^u(\mathbf{x})\hat{u}_i, \qquad p^h(\mathbf{x}) = \sum_{i=1}^{n_p} N_i^p(\mathbf{x})\hat{p}_i$$

where $\hat{\mathbf{u}} = (\hat{u}_1, \hat{u}_2, \ldots)^T$ and $\hat{\mathbf{p}} = (\hat{p}_1, \hat{p}_2, \ldots)^T$ are vectors of degrees of freedom. The corresponding algebraic form of (2.3) reads

$$\begin{bmatrix} \mathbf{A} & \mathbf{B}^T \\ \mathbf{B} & \mathbf{0} \end{bmatrix} \begin{bmatrix} \hat{\mathbf{u}} \\ \hat{\mathbf{p}} \end{bmatrix} = \begin{bmatrix} \mathbf{f_1} \\ \mathbf{f_2} \end{bmatrix} \tag{2.12}$$

where the matrices $\mathbf{A}$, $\mathbf{B}$, and vectors $\mathbf{f_1}$, $\mathbf{f_2}$ are given by

$$\begin{aligned} \mathbf{A}_{ij} &= a^h(\mathbf{N}_j^u, \mathbf{N}_i^u) & \qquad \mathbf{f_1}_i &= l_1^h(\mathbf{N}_i^u) \\ \mathbf{B}_{ij} &= b(N_j^p, \mathbf{N}_i^u) & \qquad \mathbf{f_2}_i &= l_2(N_i^p) \end{aligned}$$

In our numerical computations, we extract the approximate solution from (2.12). The discrete form of the mixed FCM formulation can also serve to compute the discrete inf-sup constant γ^h in (2.9) for a particular pair of velocity and pressure approximation spaces. The discrete inf-sup constant coincides with the square root of the smallest non-zero eigenvalue of the following generalized eigenvalue problem (see, e.g., [173]):

$$\mathbf{B}\mathbf{M}_{\mathbf{uu}}^{-1}\mathbf{B}^{\mathbf{T}}\mathbf{q} = (\gamma^h)^2\mathbf{M}_{pp}\mathbf{q}, \tag{2.13}$$

where $\mathbf{M}_{\mathbf{uu}}$ and $\mathbf{M}_{pp}$ are the Gramian matrices associated with the inner products in $\mathbf{V}^h$ and Q^h, respectively:

$$(\mathbf{M}_{\mathbf{uu}})_{ij} = (\mathbf{N}_i^u, \mathbf{N}_j^u)_{\mathbf{V}^h} \qquad (\mathbf{M}_{pp})_{ij} = (N_i^p, N_j^p)_{Q^h}$$

The norms associated to $(\cdot,\cdot)_{\mathbf{V}^h}$ and $(\cdot,\cdot)_{Q^h}$ are specified by (2.5).

If the Neumann boundary is not empty, all eigenvalues of (2.13) are strictly positive, and the discrete inf-sup constant corresponds to the smallest eigenvalue. In the case of pure Dirichlet boundary conditions, the smallest eigenvalue is zero and it has algebraic and geometric multiplicity one. The associated eigenvector corresponds to the constant pressure mode. In this case, the discrete inf-sup constant is the second smallest eigenvalue.

The essential advantage of FCM is that it admits regular and structured meshes even for complex geometries. Regular, structured meshes facilitate the definition and evaluation of higher-order bases and bases with increased smoothness compared to standard FEA, viz. C^k-continuous bases with $k \geq 1$. Recently, several inf-sup stable approximation-space pairs have been introduced, based on the increased smoothness provided by B-spline bases. In Section 2.4, we review common pairs of approximation spaces and their construction, while, in Section 2.5, we present a numerical investigation of these spaces in the context of the FCM.

2.4 Isogeometric analysis and mixed elements

In this section we first present a brief overview of the isogeometric analysis concepts relevant to this work; then, we introduce the B-spline pairs of velocity and pressure spaces herein studied.

2.4.1 Fundamentals of B-splines

Given two integers $p \geq 0$ and $n > 0$, n B-spline basis functions of degree p can be defined over a *knot vector* $\Xi = \left[\xi_1, \xi_2, \ldots, \xi_{n+p+1}\right]$, which is a non-decreasing sequence of parametric coordinates, $\xi_i \leq \xi_{i+1}, i = 1, \ldots, n+p$. If all interior knots are equally spaced the knot vector is called uniform; otherwise, it is called non-uniform. If the first and the last knots are repeated $p+1$ times, the knot vector is called open. In what follows, we always employ open knot vectors, and without loss of generality, we also assume the parameter domain to be [0, 1]. Basis functions formed from open knot vectors are interpolatory at the boundaries of the parameter domain.

A B-spline basis function is C^{∞}- continuous inside knot spans and, at most, C^{p-1}-continuous at a knot. If an interior knot value is repeated more than one time, it is called a multiple knot. We introduce the vector $[\zeta_1, \ldots, \zeta_m]$ of knots without repetitions, and the vector $[r_1, \ldots, r_m]$ of their associated multiplicities such that

$$\Xi = [\underbrace{\zeta_1, \ldots, \zeta_1}_{r_1 \text{ times}}, \underbrace{\zeta_2, \ldots, \zeta_2}_{r_2 \text{ times}}, \ldots, \underbrace{\zeta_m, \ldots, \zeta_m}_{r_m \text{ times}}]$$

where $\sum_{i=1}^{m} r_i = n + p + 1$.

At a knot of multiplicity r_i the continuity is C^{α_i} where $\alpha_i = p - r_i$ is the regularity.

The associated knot mesh on the parameter domain [0, 1] is defined as

$$\mathcal{I}_h = \{I = (\zeta_i, \zeta_{i+1}), 1 \leq i \leq m - 1\}$$

For an element $I \in \mathcal{I}_h$, we set $h_I = \operatorname{diam}(I)$, and the global mesh parameter is indicated as $h = \max\{h_I\}_{I \in \mathcal{I}_h}$.

Given a knot vector, the B-spline basis functions $N_{i,p}(\xi)$ are defined starting with the piecewise constants ($p = 0$)

$$N_{i,0}(\xi) = \begin{cases} 1, & \text{if } \xi_i \leq \xi < \xi_{i+1}, \\ 0, & \text{otherwise;} \end{cases} \tag{2.14}$$

and for $p \geq 1$, they are defined recursively by the Cox-de Boor formula [47]

$$N_{i,p}(\xi) = \frac{\xi - \xi_i}{\xi_{i+p} - \xi_i} N_{i,p-1}(\xi) + \frac{\xi_{i+p+1} - \xi}{\xi_{i+p+1} - \xi_{i+1}} N_{i+1,p-1}(\xi). \tag{2.15}$$

We denote the space of open B-splines spanned by the basis functions $N_{i,p}$ with regularity α at all internal knots by

$$S^p_{\alpha,h} \equiv S^p_\alpha(\mathcal{I}_h) := \operatorname{span}\{N_{i,p}\}_{i=1}^n.$$

For each B-spline basis function $N_{i,p}$ we also define the associated *Greville abscissa*, i.e., the knot average

$$\overline{\xi}_{i,p} = \frac{\xi_{i+1} + \ldots + \xi_{i+p}}{p}, \quad i = 1, \ldots, n.$$

When the multiplicity of the internal knots is not greater than p, all the Greville abscissae are distinct, i.e., for each Greville abscissa there is only one associated B-spline basis function.

In two dimensions, we consider the parameter domain $\hat{\Omega} = (0,1)^2 \subset \mathbb{R}^2$ (Fig. 2.4a). Given the integers p_d, α_d, and knot vectors Ξ_d with associated knot mesh $\mathcal{I}_{h,d}$, where $d = 1, 2$, the knot mesh $\mathcal{M}_h$ for the two dimensional parametric domain is defined as

$$\mathcal{M}_h = \otimes_{d=1,2} \mathcal{I}_{h,d}$$

For an element $Q \in \mathcal{M}_h$, we set $h_Q = \mathrm{diam}(Q)$, and the global mesh is indicated as $h = \max\{h_Q\}_{Q\in\mathcal{M}_h}$.

The space of bivariate B-splines is defined as

$$S^{p_1,p_2}_{\alpha_1,\alpha_2,h} \equiv S^{p_1,p_2}_{\alpha_1,\alpha_2}(\mathcal{M}_h) := \otimes_{d=1,2} S^{p_d}_{\alpha_d}(\mathcal{I}_{h,d}) = \mathrm{span}\{N_{i,p_1}(\xi)N_{j,p_2}(\eta)\}^{n_1,n_2}_{i=1,j=1}$$

where $\{N_i(\xi)\}^{n_1}_{i=1}$ and $\{N_j(\eta)\}^{n_2}_{j=1}$ are canonical bases of $S^{p_1}_{\alpha_1}$ and $S^{p_2}_{\alpha_2}$. The Greville abscissae of a bivariate B-spline are defined as $\bar{\gamma}_{ij,\mathbf{p}} = (\overline{\xi}_{i,p_1}, \overline{\eta}_{j,p_2})$ with $\overline{\xi}_{i,p_1}, \overline{\eta}_{j,p_2}$ being respectively the Greville abscissae of N_{i,p_1} and N_{j,p_2}.

B-spline surfaces are obtained from linear combinations of bivariate B-spline basis functions

$$\mathbf{S}(\xi,\eta) = \sum_{i,j} \mathbf{P}_{i,j} N_{i,p_1}(\xi) N_{j,p_2}(\eta)$$

where $\mathbf{P}_{i,j}$ are the so-called control points.

For the regular grids consider herein, the control points and the Greville abscissae have coincident locations.

An illustration of a bivariate B-spline and its associated control points for $p_1 = 3$, $p_2 = 2$, $\alpha_1 = 2$, $\alpha_2 = 1$ is presented in Fig. 2.4.

In order to approximate the unknown fields, isogeometric analysis employs the isoparametric concept as in standard FEM, i.e., the same B-spline basis functions are used for the description of both the geometry and the unknown fields. In the case of mixed formulations, the pressure field and each component of the velocity field possess their own control nets, which are all defined on the same geometry. The basis functions associated with these control nets are then used to approximate the fields; see Section 2.4.2.

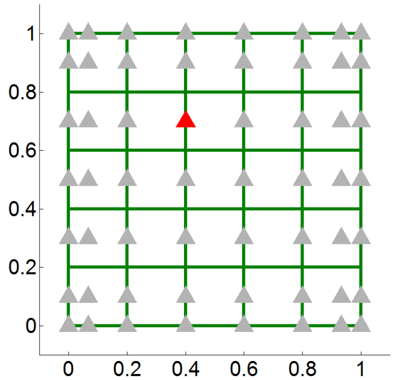

(a) Parameter domain

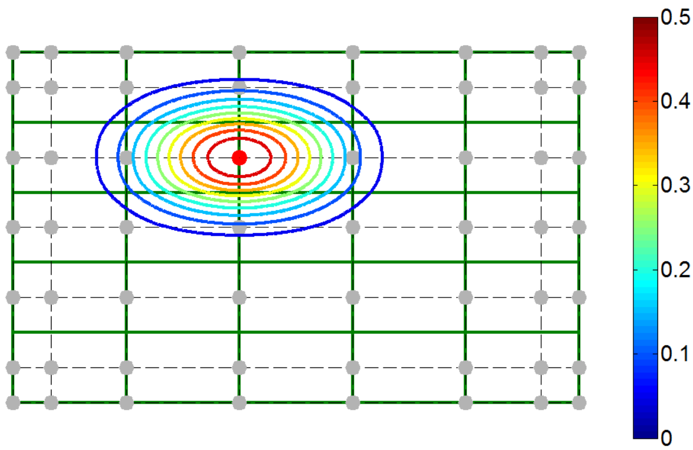

(b) Physical domain

Fig. 2.4: An illustration of a bivariate B-spline basis function on a rectangular domain with $\mathbf{p} = (3, 2)$, $\boldsymbol{\alpha} = (2, 1)$. (a) Parameter domain: The triangles denote the Greville absissae (and the one associated with the considered basis function is marked in red). (b) Physical domain: The dashed line denotes the control net; the solid lines denote the knot lines (i.e., the mesh); the circles denote the control points (and the one associated with the considered basis function is marked in red).

2.4.2 Mixed B-spline discretizations

As mentioned in the previous sections, one important advantage of FCM is that the background mesh of the immersed domain is regular. This allows one to use only B-splines for the approximation instead of NURBS as in standard IGA. The immersed domain is a rectangle (in 2D, or rectangular cuboid in 3D) and therefore the geometry map becomes affine. As a consequence, pull-back mappings such as the Piola transform become trivial. We note that low-order B-splines can be used for the analysis, even if the physical domain is parameterized by high-order splines.

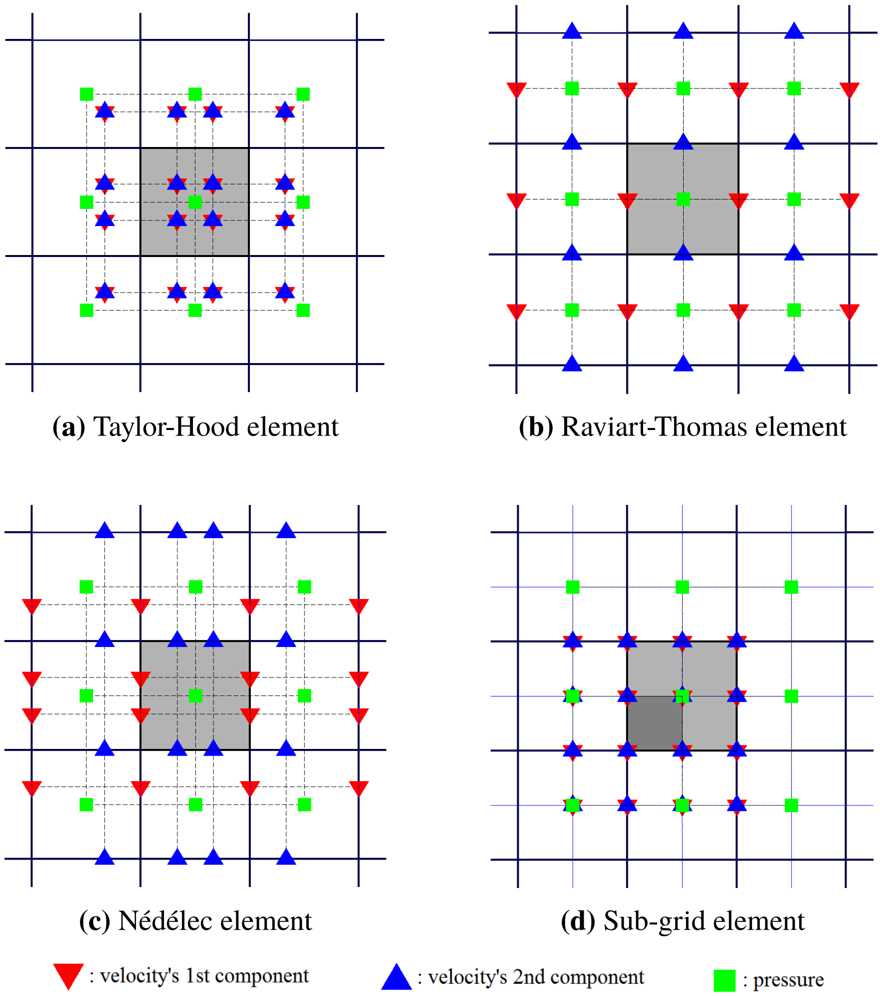

Fig. 2.5: Control nets (dash lines) associated with four families of IGA mixed elements ($p = 2$). Green squares denote control points for pressure, red triangles those for velocity's 1^{st} component, and blue triangles those for velocity's 2^{nd} component.

In this work, we investigate the behavior of the following families of mixed elements in the IGA-FCM setting, which are graphically depicted in Fig. 2.5:

- Taylor-Hood element [94, 118, 119] (Fig. 2.5a):

$$\begin{cases} \mathbf{V}_h^{TH} = (S_{p-1,p-1,h}^{p+1,p+1})^2, \\ Q_h^{TH} = S_{p-1,p-1,h}^{p,p}. \end{cases} \tag{2.16}$$

  The velocity and pressure spaces are defined on the same knot mesh with the same regularity. The two components of velocity are defined with the same space. The velocity space is one order higher than the pressure space. This implies that the multiplicity of the knots of the velocity space is increased by one with respect to that of the pressure space.
- Raviart-Thomas element [118, 121] (Fig. 2.5b):

$$\begin{cases} \mathbf{V}_h^{RT} = S_{p,p-1,h}^{p+1,p} \times S_{p-1,p,h}^{p,p+1}, \\ Q_h^{RT} = S_{p-1,p-1,h}^{p,p}. \end{cases} \tag{2.17}$$

  This is a $H(\text{div})$ conforming element. The velocity space is anisotropic with respect to the degree. Both velocity and pressure spaces are defined on the same knot mesh with their highest regularities.
- Nédélec element [118] (Fig. 2.5c):

$$\begin{cases} \mathbf{V}_h^{ND} = S_{p,p-1,h}^{p+1,p+1} \times S_{p-1,p,h}^{p+1,p+1}, \\ Q_h^{ND} = S_{p-1,p-1,h}^{p,p}. \end{cases} \tag{2.18}$$

  This element “lies" between the Taylor-Hood and the Raviart-Thomas elements. The velocity space uses equal degrees for both components as in the Taylor-Hood element, while maintaining the regularities of Raviart-Thomas element. Both velocity and pressure spaces are define on the same knot mesh.
- Sub-grid element [119, 120] (Fig. 2.5d):

$$\begin{cases} \mathbf{V}_h^{SG} = (S_{p,p,h/2}^{p+1,p+1})^2, \\ Q_h^{SG} = S_{p-1,p-1,h}^{p,p}. \end{cases} \tag{2.19}$$

  The velocity and the pressure spaces are defined on different knot meshes. The velocity knot mesh is obtained by subdividing each element of the pressure knot mesh into four elements (in 2D, and 8 elements in 3D.) Both velocity and pressure spaces have their highest regularities.

Since the velocity mesh is refined with respect to the pressure mesh, the Gauss points are associated with the velocity mesh. Consequently, in order to evaluate the pressure basis functions in these points, a special data structure is needed to allow the determination of the pressure element associated with a particular velocity element.

2.5 Numerical experiments

In this section we investigate the numerical performance of IGA-FCM for mixed formulations. System (2.12) is solved using the four mixed element families discussed in Section 2.4.2. The numerical inf-sup values are computed by solving the generalized eigenvalue problem (2.13).

The accuracy of the IGA-FCM approximation depends on the applied integration depth. If the integration depth is insufficient, the accuracy of the approximation is determined by the integration error, rather than the error in the IGA approximation. This is particularly manifest for higher-order approximations, due the fact that the integration scheme is typically of low order (1 or 2); see Section 2.3.2. In our test cases, we have selected integration depth $k = 13$. This integration depth ensures that for the considered range of polynomial orders and mesh-sizes, the integration error is subordinate to the IGA-approximation error. Hence, it allows to test and compare the different methods in the considered range of mesh-sizes and polynomial orders. We use Jacobi preconditioning in the solution procedure for the discrete systems, to reduce the effect of ill-conditioning and the corresponding solution error on the accuracy of the results. The condition numbers of the linear systems corresponding to the IGA-FCM discretization generally increase as the mesh is refined, because mesh refinement typically leads to the occurrence of cut cells with smaller volume fractions due to the fact that the number of cut cells increases, and as the polynomial order of the approximation is increased [147].

In all computations, we have used a global, uniform p-dependent stabilization parameter according to $\beta = 5(p + 1)^2$. The p-dependence of the stabilization parameter has been selected in accordance with the corresponding dependence of the constant in the underlying discrete trace inequality [167]. It is to be mentioned that on fine meshes and at higher orders of approximation, the convergence results presented in Section 2.5.3 display some minor (non-essential) sensitivity to the stabilization parameter.

2.5.1 Dirichlet quarter-annulus problem

We investigate the properties of the IGA-FCM mixed formulation in combination with the element families in (2.16)–(2.19) on the basis of (2.3) on an open quarter-annulus domain

$$\Omega = \left\{(x, y) \in \mathbb{R}^2_{>0} : 1 < x^2 + y^2 < 16\right\},$$

with inner radius $R_1 = 1$ and outer radius $R_2 = 4$; see Fig. 2.6. Dirichlet boundary conditions are prescribed on the entire boundary $\partial\Omega = \Gamma_D$ and, accordingly, it holds that $\Gamma_N = \emptyset$. The data $\mathbf{f}$ and $\mathbf{g}$ are selected such that

$$\begin{aligned} u_1 &= 10^{-6}x^2y^4(x^2+y^2-1)(x^2+y^2-16)(5x^4+18x^2y^2-85x^2+13y^4-153y^2+80), \\ u_2 &= 10^{-6}xy^5(x^2+y^2-1)(x^2+y^2-16)(102x^2+34y^2-10x^4-12x^2y^2-2y^4-32), \\ p &= 10^{-7}xy(y^2-x^2)(x^2+y^2-16)^2(x^2+y^2-1)^2\exp\left(14(x^2+y^2)^{-1/2}\right) \end{aligned} \tag{2.20}$$

satisfy (2.3). The sample solution (4.20) has been taken from [174]. Note that u_1 and u_2 vanish on $\partial\Omega$ and, hence, $\mathbf{g} = \mathbf{0}$. Moreover, the pressure complies with $\int_\Omega p = 0$. The exact velocity and pressure contours are plotted in Fig. 2.7.

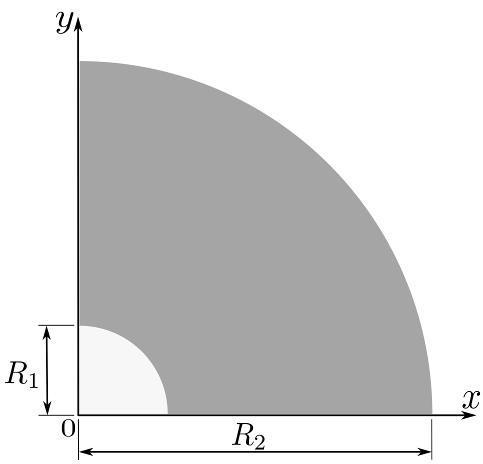

Fig. 2.6: Geometry setup for the quarter annulus problem.

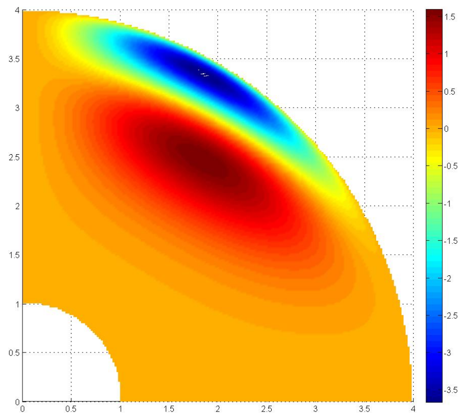

(a) First component of the velocity

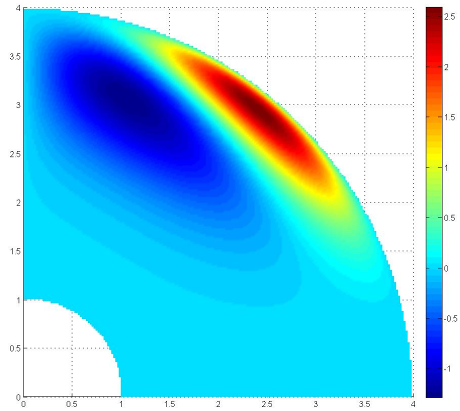

(b) Second component of the velocity

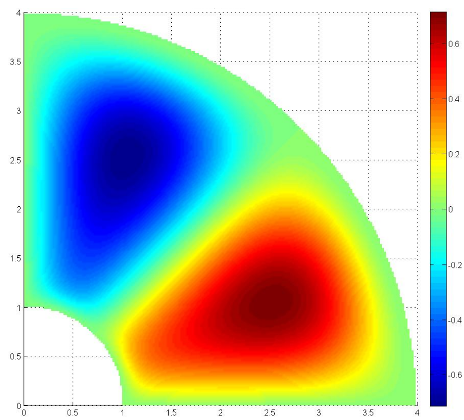

(c) Pressure

Fig. 2.7: Analytical solution of the quarter annulus problem.

2.5.2 Numerical inf-sup test

To test the stability of the IGA-FCM formulation for the four different families of mixed elements, we compute the associated discrete inf-sup values by means of (2.13) for pressure polynomial degrees $p \in \{1, 2, 3\}$ and on a sequence of uniform background meshes with 8×8, 16×16, 32×32, and 64×64 elements. The results are reported in Table 2.1 and visualized in Fig. 2.8. Table 2.1 conveys that for all four families of mixed finite-elements the corresponding discrete inf-sup constants are bounded from below away from 0. In particular, the Taylor–Hood and Sub-grid elements display very

Table 2.1: Discrete inf-sup constants of IGA-FCM for the quarter annulus problem using the four considered mixed elements with polynomial degrees $p \in \{1, 2, 3\}$ for the pressure field.

		Mesh			
	$C_{\text{inf-sup}}$	8×8	16×16	32×32	64×64
$p = 1$	TH	.5551	.5174	.4900	.4703
	RT	.2931	.2860	.2324	.2482
	ND	.5195	.5173	.4899	.4703
	SG	.6393	.5619	.5157	.4861
$p = 2$	TH	.5469	.5137	.4879	.4690
	RT	.2266	.1979	.1995	.1621
	ND	.4303	.4538	.3893	.3964
	SG	.6221	.5562	.5132	.4848
$p = 3$	TH	.5438	.5122	.4870	.4685
	RT	.2110	.1897	.1753	.1696
	ND	.3588	.3701	.3058	.3095
	SG	.6155	.5538	.5121	.4842

similar inf-sup values for all considered polynomial orders. On the finest mesh (64×64), these elements exhibit inf-sup values of approximately $0.47 - 0.49$, essentially independent of p. For the Nédélec element, the inf-sup value tends to decrease as the polynomial order increases. While for $p = 1$ the inf-sup constant of the Nédélec element is comparable to that of the Taylor–Hood and Sub-grid elements, for $p \in \{2, 3\}$ it exhibits smaller values.

The Raviart–Thomas element yields the smallest inf-sup values. This result is consistent with the fact that the divergence of the velocity space is smallest for the Raviart–Thomas elements, in the sense that $\operatorname{div}\mathbf{V}_h^{RT}$ is a proper subset of $\operatorname{div}\mathbf{V}_h^{TH}$, $\operatorname{div}\mathbf{V}_h^{ND}$ and $\operatorname{div}\mathbf{V}_h^{SG}$. One may also note that the inf-sup value of the Nédélec element generally lies between the inf-sup values of the Raviart–Thomas element and of the Taylor–Hood element, which is in agreement with the inclusion relations $\mathbf{V}_h^{RT} \subset \mathbf{V}_h^{ND} \subset \mathbf{V}_h^{TH}$. Fig. 2.8 corroborates that for the considered range of polynomial orders and meshes, all four elements pass the inf-sup test. The numerical results thus suggest that all four elements are stable on uniform meshes, irrespective of the mesh-size and polynomial order. The results in Fig. 2.8 also convey that the inf-sup constant of the Raviart–Thomas element exhibits some fluctuations as the mesh-size varies. This behavior can be attributed to the fact that the Raviart–Thomas element belongs to the $H(\mathrm{div})$-conforming family, i.e., the divergence operator maps $\mathbf{V}_h^{RT}$ into and onto Q_h^{RT}. On account of the compatibility between $\mathrm{div}\mathbf{V}_h^{RT}$ and Q_h^{RT}, the Raviart–Thomas element is sensitive to the manner in which constraints such as Dirichlet conditions are imposed, because such constraints generally interfere with the congruence of $\mathrm{div}\mathbf{V}_h^{RT}$ and Q_h^{RT}.

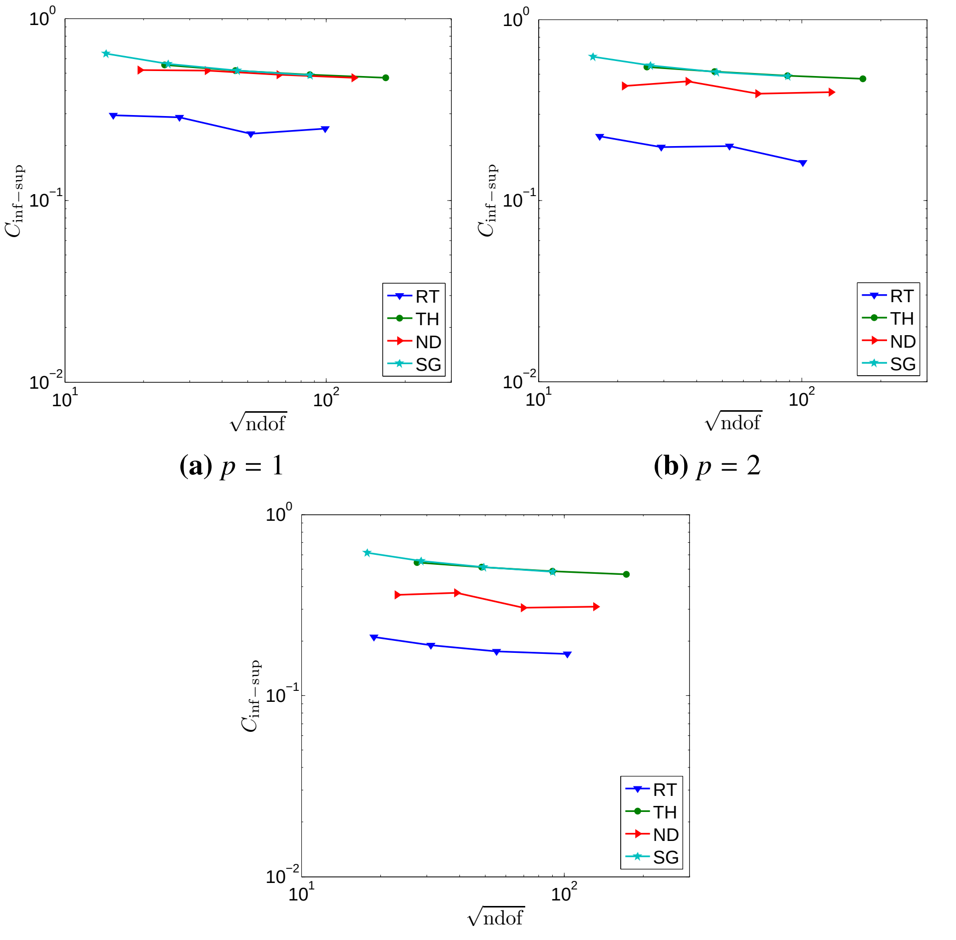

(a) $p = 1$ **(b)** $p = 2$ **(c)** $p = 3$

Fig. 2.8: Discrete inf-sup constants of IGA-FCM for the quarter annulus problem using the four considered mixed elements with polynomial degrees $p \in \{1, 2, 3\}$ for the pressure field.

2.5.3 Convergence study

In this section, we test the convergence of the IGA-FCM formulation for the four considered mixed element families. Table 2.2 presents the relative L^2 and H^1 errors of the velocity field, and the L^2 error of the pressure field, when the degree of the pressure is $p = 1$. For Taylor–Hood, Nédélec and Sub-grid elements, the velocity spaces are isotropic and one order higher than that of the pressure space. The optimal convergence rate for the velocity approximations that can be obtained with these elements is therefore 2 in the H^1-norm and 3 in the L^2-norm. For the Raviart–Thomas element, the velocity approximation space is anisotropic with respect to the degree, and the space is complete only up to degree p. The optimal convergence rates of the velocity approximation in the H^1-norm and the L^2-norm are then restricted to 1 and 2, respectively. Table 2.2 corroborates that the aforementioned optimal convergence rates are indeed obtained.

Considering the convergence of the pressure approximation, the results in Table 2.2 indicate that the Taylor–Hood, Nédélec and Sub-grid element yield optimal convergence rates, in particular, $\|p - p_h\|_{L^2} = O(h^{p+1})$ as $h \to 0$. The Raviart–Thomas element appears to display a suboptimal convergence rate, although the asymptotic convergence rate is not yet fully apparent from the considered sequence of meshes. The following *a-priori* estimate (see [121, Theorem 6.2])

$$\|p - p_h\| \leq \left(1 + \frac{1}{\gamma_h}\right) \inf_{q^h \in Q_h} \|p - q_h\|_{Q_h} + \frac{C_a}{\gamma_h} \|\mathbf{u} - \mathbf{u}_h\|_{\mathbf{V}_h} \tag{2.21}$$

however conveys that the convergence rate of the pressure is potentially restricted by the convergence rate of the velocity in the H^1-norm, which is only of order $p = 1$ for the Raviart–Thomas element, and therefore one order lower than the interpolation error in the pressure. For the Taylor–Hood, Nédélec and Sub-grid elements, the velocity-approximation error decays as $\|\mathbf{u} - \mathbf{u}_h\|_{\mathbf{V}_h} = O(h^{p+1})$ as $h \to 0$, and this rate coincides with the rate of convergence of the pressure-interpolation error.

To facilitate a comparison of the results obtained by means of the four mixed elements in the context of IGA-FCM, Fig. 2.9 plots the relative errors with respect to the total degrees of freedom (of the velocity and pressure spaces). One can observe that the Sub-grid element provides the most efficient approximation, in that it achieves the lowest error per degree of freedom for both pressure and velocity. This result is consistent with the theory of k-refinement, since both the velocity and pressure of the Sub-grid element possess the highest order of continuity that can be attained without degenerating to a single element.

Table 2.2: Relative error of IGA-FCM for the quarter annulus problem for the Taylor–Hood (TH), Raviart–Thomas (RT), Nédélec (ND) and Subgrid (SG) elements with $p = 1$ for the pressure field.

	Mesh			
	8×8	16×16	32×32	64×64
$\|\mathbf{u} - \mathbf{u}_h^{TH}\|_{L^2}$	7.76e-2	1.49e-2	2.24e-3	3.11e-4
order	–	2.38	2.74	2.85
$\|\mathbf{u} - \mathbf{u}_h^{TH}\|_{H^1}$	3.68e-1	1.28e-1	2.98e-2	6.23e-3
order	–	1.53	2.10	2.26
$\|p - p_h^{TH}\|_{L^2}$	7.57e-1	2.27e-1	3.97e-2	8.23e-3
order	–	1.74	2.51	2.27
$\|\mathbf{u} - \mathbf{u}_h^{RT}\|_{L^2}$	3.37e-1	1.29e-1	3.85e-2	1.02e-2
order	–	1.38	1.74	1.92
$\|\mathbf{u} - \mathbf{u}_h^{RT}\|_{H^1}$	6.27e-1	3.62e-1	1.88e-1	9.38e-2
order	–	0.79	0.94	1.01
$\|p - p_h^{RT}\|_{L^2}$	4.00e0	2.78e0	1.69e0	6.01e-1
order	–	0.53	0.71	1.50
$\|\mathbf{u} - \mathbf{u}_h^{ND}\|_{L^2}$	9.46e-2	1.67e-2	2.42e-3	3.23e-4
order	–	2.51	2.78	2.90
$\|\mathbf{u} - \mathbf{u}_h^{ND}\|_{H^1}$	2.86e-1	8.94e-2	2.51e-2	6.41e-3
order	–	1.68	1.83	1.97
$\|p - p_h^{ND}\|_{L^2}$	9.23e-1	2.84e-1	5.73e-2	1.18e-2
order	–	1.70	2.31	2.28
$\|\mathbf{u} - \mathbf{u}_h^{SG}\|_{L^2}$	1.36e-1	2.13e-2	2.82e-3	3.51e-4
order	–	2.68	2.92	3.01
$\|\mathbf{u} - \mathbf{u}_h^{SG}\|_{H^1}$	3.07e-1	9.22e-2	2.49e-2	6.45e-3
order	–	1.73	1.89	1.95
$\|p - p_h^{SG}\|_{L^2}$	8.30e-1	1.77e-1	4.79e-2	7.83e-3
order	–	2.23	1.89	2.61

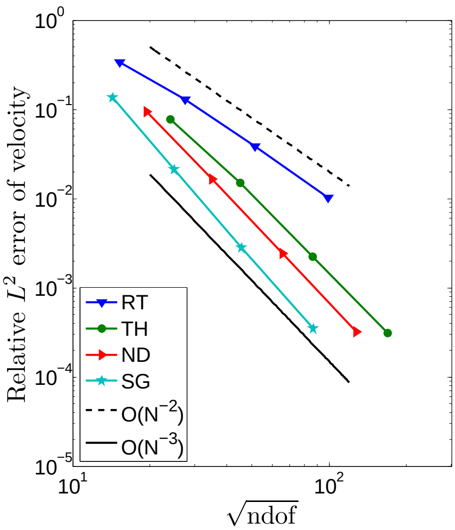

(a) Relative L^2- error of velocity, $p = 1$

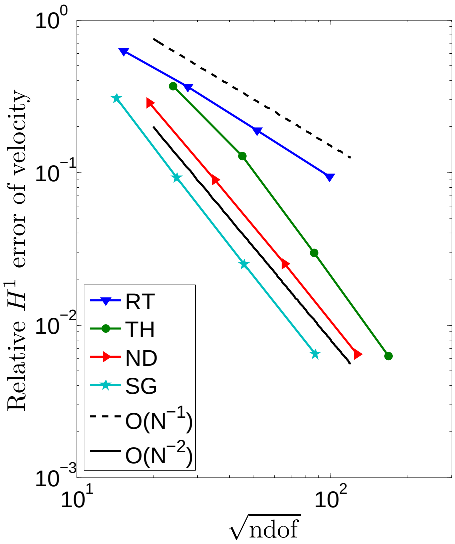

(b) Relative H^1- error of velocity, $p = 1$

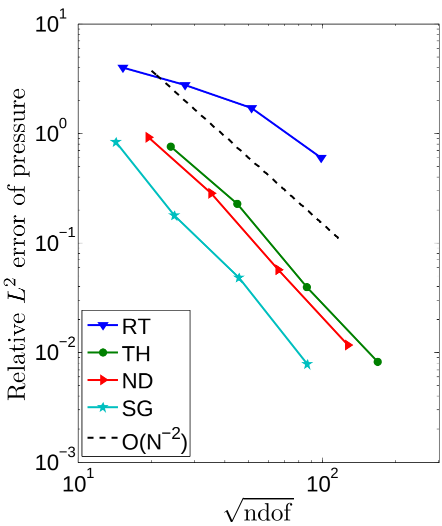

(c) Relative L^2- error of pressure, $p = 1$

Fig. 2.9: Relative error of IGA-FCM for the quarter annulus problem versus the total number of degrees of freedom for the Taylor–Hood (TH), Raviart–Thomas (RT), Nédélec (ND) and Sub-grid (SG) elements with $p = 1$ for the pressure field†.

In a similar manner, we test the four considered mixed elements with pressure spaces of degree $p = 2$ and $p = 3$. The corresponding results are presented in Table 2.3 and Fig. 2.10, and in Table 2.4 and Fig. 2.11, respectively. For $p = 2$, the observed convergence rates for the Taylor–Hood and Nédélec elements are close to the optimal convergence rates. For the Sub-grid element, the results indicate an optimal rate of convergence for the velocity approximation. The results for the pressure approximation are inconclusive. For the Raviart–Thomas element, the velocity approximation displays optimal convergence rates in both the H^1-norm and the L^2-norm. The convergence rate for the pressure approximation again appears to be suboptimal, similar to the case of $p = 1$. Also for $p = 3$, the Raviart–Thomas element exhibits optimal convergence rates for the velocity and a suboptimal convergence rate for the pressure. The results for the Taylor–Hood and Nédélec elements for $p = 3$ suggest optimal convergence rates for these elements. According to Table 2.4, the Sub-grid element exhibits suboptimal convergence rates for $p = 3$. Especially the observed rate of decay of the L^2-norm of the error in the pressure approximation, which is approximately 2.6, falls short of the optimal convergence rate of 4. It appears that this significantly suboptimal convergence rate of the error in the pressure approximation of the Sub-grid element is due to the fact that the FCM acts differently on the micro-elements of the velocity approximation than on the macro-elements of the pressure approximation. However, the precise mechanism and the relation to the polynomial degree p of the approximation remain topics for further study.

[†]It is important to note that, because the velocity space of the RT element in (2.17) is anisotropic with respect to the degree and is only complete up to order p, the corresponding optimal convergence rates for the velocity approximation are one order lower than those for the other elements.

Table 2.3: Relative error of IGA-FCM for the quarter annulus problem for the Taylor–Hood (TH), Raviart–Thomas (RT), Nédélec (ND) and Sub-grid (SG) elements with $p = 2$ for the pressure field.

	Mesh			
	8×8	16×16	32×32	64×64
$\|\mathbf{u} - \mathbf{u}_h^{TH}\|_{L^2}$	1.64e-2	1.79e-3	1.54e-4	1.15e-5
order	–	3.20	3.54	3.74
$\|\mathbf{u} - \mathbf{u}_h^{TH}\|_{H^1}$	5.29e-2	9.93e-3	1.57e-3	2.32e-4
order	–	2.41	2.66	2.76
$\|p - p_h^{TH}\|_{L^2}$ –	9.49e-2	1.26e-2	1.65e-3	2.24e-4
order	–	2.91	2.94	2.88
$\|\mathbf{u} - \mathbf{u}_h^{RT}\|_{L^2}$	1.40e-1	2.00e-2	2.53e-3	3.07e-4
order	–	2.81	2.99	3.04
$\|\mathbf{u} - \mathbf{u}_h^{RT}\|_{H^1}$	2.68e-1	6.94e-2	1.73e-2	4.21e-3
order	–	1.95	2.01	2.04
$\|p - p_h^{RT}\|_{L^2}$	5.08e0	1.93e0	2.38e-1	6.31e-2
order	–	1.40	3.01	1.92
$\|\mathbf{u} - \mathbf{u}_h^{ND}\|_{L^2}$	2.52e-2	2.25e-3	1.72e-4	1.21e-5
order	–	3.48	3.71	3.82
$\|\mathbf{u} - \mathbf{u}_h^{ND}\|_{H^1}$	7.33e-2	1.22e-2	1.74e-3	2.35e-4
order	–	2.59	2.81	2.89
$\|p - p_h^{ND}\|_{L^2}$	2.68e-1	3.47e-2	4.16e-3	4.12e-4
order	–	2.95	3.06	3.34
$\|u - u_h^{SG}\|_{L^2}$	4.07e-2	3.09e-3	2.04e-4	1.35e-5
order	–	3.72	3.92	3.92
$\|\mathbf{u} - \mathbf{u}_h^{SG}\|_{H^1}$	8.99e-2	1.36e-2	1.84e-3	2.43e-4
order	–	2.73	2.88	2.92
$\|p - p_h^{SG}\|_{L^2}$	1.75e-1	3.37e-2	3.68e-3	7.10e-4
order	–	2.37	3.19	2.37

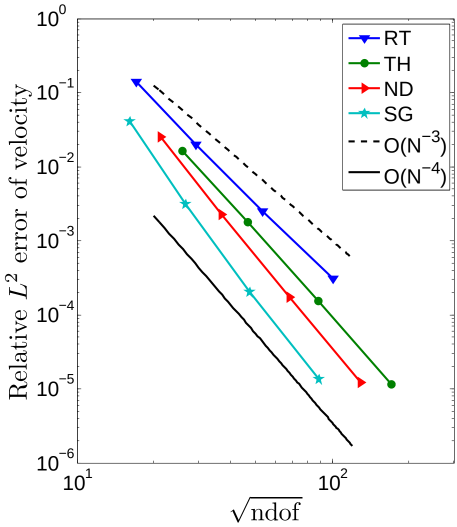

(a) Relative L^2 error of velocity, $p = 2$

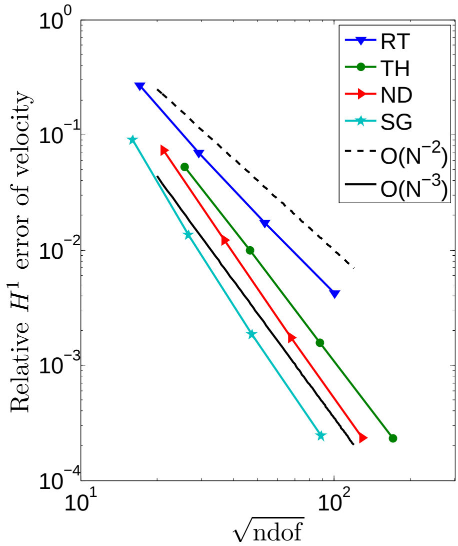

(b) Relative H^1 error of velocity, $p = 2$

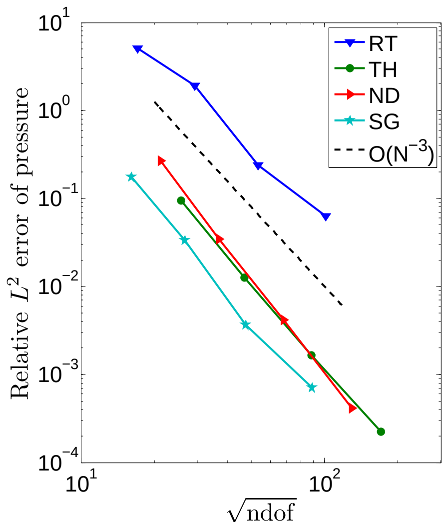

(c) Relative L^2 error of pressure, $p = 2$

Fig. 2.10: Relative error of IGA-FCM for the quarter annulus problem for the Taylor–Hood (TH), Raviart–Thomas (RT), Nédélec (ND) and Sub-grid (SG) elements with $p = 2$ for the pressure field.

Table 2.4: Relative error of IGA-FCM for the quarter annulus problem for the Taylor–Hood (TH), Raviart–Thomas (RT), Nédélec (ND) and Sub-grid (SG) elements with $p = 3$ for the pressure field.

	Mesh			
	8×8	16×16	32×32	64×64
$\|\|\mathbf{u} - \mathbf{u}_h^{TH}\|\|_{L^2}$	3.28e-3	1.99e-4	9.28e-6	3.60e-7
order	–	4.04	4.42	4.69
$\|\|\mathbf{u} - \mathbf{u}_h^{TH}\|\|_{H^1}$	9.96e-3	1.06e-3	9.26e-5	7.50e-6
order	–	3.23	3.52	3.63
$\|\|p - p_h^{TH}\|\|_{L^2}$	1.46e-2	3.37e-3	2.56e-4	2.35e-5
order	–	2.12	3.72	3.44
$\|\|\mathbf{u} - \mathbf{u}_h^{RT}\|\|_{L^2}$	3.98e-2	2.85e-3	1.79e-4	1.14e-5
order	–	3.80	3.99	3.97
$\|\|\mathbf{u} - \mathbf{u}_h^{RT}\|\|_{H^1}$	7.30e-2	9.88e-3	1.25e-3	1.57e-4
order	–	2.88	2.98	3.00
$\|\|p - p_h^{RT}\|\|_{L^2}$	2.59	2.75e-1	4.00e-2	3.25e-3
order	–	3.24	2.78	3.62
$\|\|\mathbf{u} - \mathbf{u}_h^{ND}\|\|_{L^2}$	5.78e-3	2.62e-4	1.05e-5	3.87e-7
order	–	4.46	4.64	4.77
$\|\|\mathbf{u} - \mathbf{u}_h^{ND}\|\|_{H^1}$	1.69e-2	1.45e-3	1.07e-4	7.59e-6
order	–	3.54	3.76	3.82
$\|\|p - p_h^{ND}\|\|_{L^2}$	1.31e-1	7.15e-3	3.75e-4	2.91e-5
order	–	4.19	4.25	3.69
$\|\|\mathbf{u} - \mathbf{u}_h^{SG}\|\|_{L^2}$	9.58e-3	3.91e-4	1.64e-5	9.14e-7
order	–	4.62	4.57	4.17
$\|\|\mathbf{u} - \mathbf{u}_h^{SG}\|\|_{H^1}$	2.13e-2	1.73e-3	1.31e-4	1.28e-5
order	–	3.62	3.73	3.35
$\|\|p - p_h^{SG}\|\|_{L^2}$	6.56e-2	8.77e-3	1.44e-3	2.32e-4
order	–	3.14	2.63	2.63

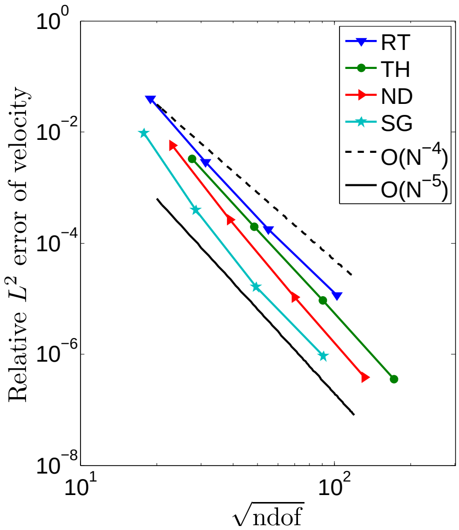

(a) Relative L^2 error of velocity, $p = 3$

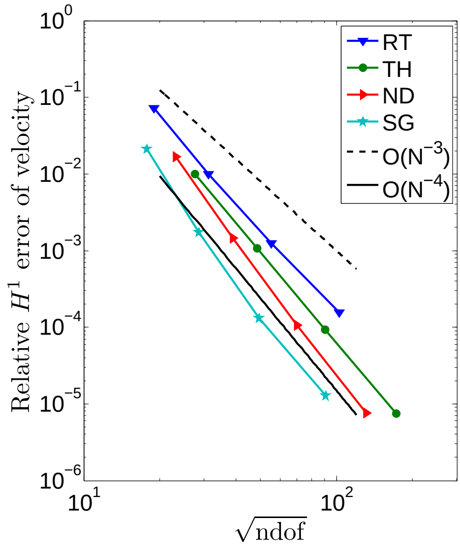

(b) Relative H^1 error of velocity, $p = 3$

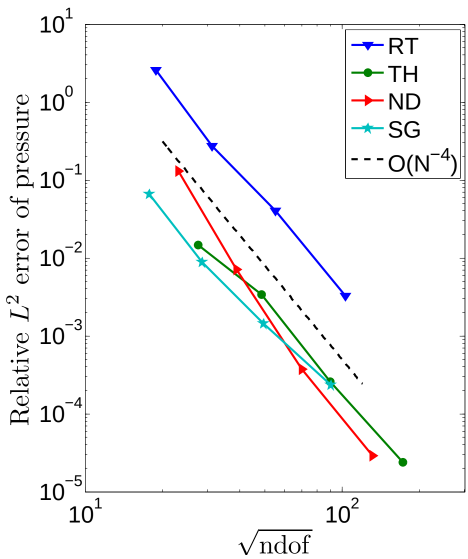

(c) Relative L^2 error of pressure, $p = 3$

Fig. 2.11: Relative error of IGA-FCM for the quarter annulus problem for the Taylor–Hood (TH), Raviart–Thomas (RT), Nédélec (ND) and Sub-grid (SG) elements with $p = 3$ for the pressure field.

Inspection of the pressure approximations reveals that all four elements exhibit pressure oscillations near the cut boundary. These pressure oscillations are particularly manifest on coarse meshes and at low orders of approximation. Fig. 2.12 presents the pressure approximation provided by the Taylor–Hood element for $p = 1$ on a mesh with 32×32 elements. This result is representative of the pressure approximations provided by the other three element families. Moreover, it is noted that the pressure oscillations are insensitive to the type of Nitsche stabilization, in the sense that results obtained with a local stabilization parameter (see Section 2.2.2) or with a (skew-symmetric) parameter-free Nitsche formulation [175] only show non-essential differences with the results obtained using global stabilization as presented here. The pressure oscillations near the cut boundary are clearly discernible. It is to be mentioned that the pressure oscillations decay fast under mesh refinement and order elevation, in accordance with the aforementioned convergence rates for the pressure approximations.

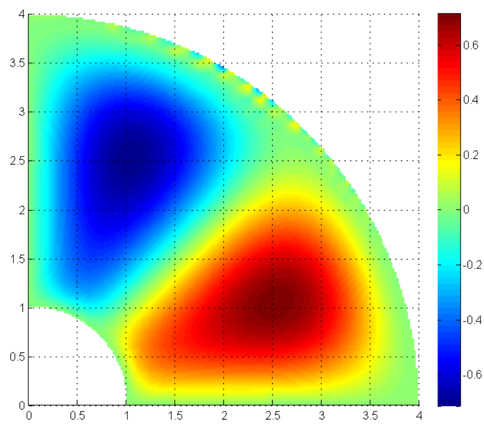

Fig. 2.12: Illustration of pressure oscillations in the vicinity of cut boundary ($p = 1$, 32×32 mesh).

2.6 Conclusions

We investigated the properties of the Isogeometric Finite-Cell Method (IGA-FCM) for mixed formulations, in the context of the Stokes problem. We considered four different families of isogeometric mixed elements, namely, Taylor–Hood, Raviart–Thomas, Nédélec, and Sub-grid elements. For a generic test case corresponding to a quarter-annulus domain, we computed the numerical inf-sup constants for the aforementioned element families for linear, quadratic and cubic pressure approximations. The results convey that all four elements pass the inf-sup stability test in the IGA-FCM setting. We also assessed the convergence behavior of the four element families under mesh refinement for linear, quadratic and cubic approximations. For the Taylor–Hood and Nédélec elements, optimal convergence rates were observed for the velocity approximation in both the H^1-norm and the L^2-norm and for the pressure approximation in the L^2-norm. The Raviart–Thomas element yields an optimal convergence rate for the velocity approximation, but the pressure approximation is generally suboptimal. The convergence behavior of the Sub-grid element depends on the order of approximation. For linear pressure approximations, we observed optimal convergence rates for both velocity and pressure. For quadratic approximations, the convergence rate for the velocity approximation appears optimal, but the observed convergence for the pressure is irregular and inconclusive. For cubic approximations, the observed convergence rates for the Sub-grid element are suboptimal, both for velocity and for pressure.

For the Taylor–Hood and Nédélec element families, the observed optimal convergence rates of IGA-FCM are in agreement with corresponding results in the literature for boundary-fitted approximations. For the Raviart–Thomas elements, the observed optimal convergence rate for the velocity approximation is in accordance with corresponding results for fitted approximations. However, the suboptimal convergence rate for the pressure approximation of the Raviart–Thomas elements in the IGA-FCM context is at variance with the optimal rates that have been observed in the literature for fitted approximations. The suboptimal convergence rates for higher-order Sub-grid elements are also incongruent with corresponding results in the literature for fitted approximations.

Chapter 3

Skeleton-stabilized IsoGeometric Analysis: High-regularity Interior-Penalty methods for incompressible viscous flow problems

Abstract

A Skeleton-stabilized IsoGeometric Analysis (SIGA) technique is proposed for incompressible viscous flow problems with moderate Reynolds number. The proposed method allows utilizing identical finite dimensional spaces (with arbitrary B-splines/NURBS order and regularity) for the approximation of the pressure and velocity components. The key idea is to stabilize the jumps of high-order derivatives of variables over the skeleton of the mesh. For B-splines/NURBS basis functions of degree k with C^{α}-regularity ($0 \leq \alpha < k$), only the derivative of order $\alpha + 1$ has to be controlled. This stabilization technique thus can be viewed as a high-regularity generalization of the (Continuous) Interior-Penalty Finite Element Method. Numerical experiments are performed for the Stokes and Navier-Stokes equations in two and three dimensions. Oscillation-free solutions and optimal convergence rates are obtained. In terms of the sparsity pattern of the algebraic system, we demonstrate that the block matrix associated with the stabilization term has a considerably smaller bandwidth when using B-splines than when using Lagrange basis functions, even in the case of C^0-continuity. This property makes the proposed isogeometric framework practical from a computational effort point of view.

Reproduced from: T. Hoang, C.V. Verhoosel, F. Auricchio, E.H. van Brummelen, A. Reali, *Skeleton-stabilized IsoGeometric Analysis: High-regularity Interior-Penalty methods for incompressible viscous flow problems*, Computer Methods in Applied Mechanics and Engineering, submitted, October 2017

3.1 Introduction

Isogeometric analysis (IGA) was introduced by Hughes *et al.* [44] as a novel analysis paradigm targeting better integration of Computer Aided Design (CAD) and Finite Element Analysis (FEA). The pivotal idea of IGA is that it directly inherits its basis functions from CAD modeling, where Non-uniform Rational B-splines (NURBS) are the industry standard. For analysis-suitable CAD models, geometrically exact analyses can be performed on the coarsest level of the CAD geometry. This contrasts with conventional FEA, which typically uses Lagrange polynomials as basis functions defined on a geometrically approximate mesh. An additional highly appraised property of IGA is that splines allow one to achieve higher-order continuity, in contrast to the C^0-continuity of conventional FEA. We refer to [43, 114] for an overview of established IGA developments.

In the context of viscous flow problems – particularly in the incompressible regime – IGA has been applied very successfully. Within the framework of inf-sup stable spaces for mixed formulations [13], a variety of compatible discretizations has been developed, most notably: Taylor-Hood elements [94, 118, 119], Nédélec elements [118], subgrid elements [119, 120], and H(div)-conforming elements [118, 121–123]. The mixed discretization approach leads to a saddle point system where the discrete velocity and pressure spaces are chosen differently in order to satisfy the discrete inf-sup condition. The advantage of this approach is that a stable discrete system is obtained straightforwardly from the continuous weak formulation (without any modifications) if the pair of discrete spaces is chosen appropriately.

In practice, employing the same discrete space for the velocity and pressure fields can provide advantages in term of implementation and computer resources. These advantages become more pronounced in multi-physics problems with many different field variables, for which the derivation of inf-sup stable discrete spaces can be non-trivial. The data structures required to represent the different spaces can make this approach impractical in terms of implementation and computational expenses. Moreover, in the context of IGA, using the same discretization space for all field variables enables direct usage of the CAD basis functions, which is highly beneficial from the vantage point of CAD/FEA integration.

Although there are merits in using the same discrete space for all field variables, without modification this generally leads to an unstable system in the Babuška-Brezzi sense. A common remedy to circumvent this issue is to use stabilization techniques. Various stabilization techniques have been studied in the IGA setting, most notably: Galerkin-least squares and Douglas-Wang stabilization [94] and variational multiscale stabilization (VMS) [28]. The structure of these approaches is that the stabilization is based on element-by-element residuals. We note that recently a combination of VMS and compatible B-splines is studied in [176]. It is also noteworthy that for incompressible elasticity the use of inf-sup stable discretizations can be circumvented by using stream functions [174], B-bar method [177] and B^D-bar method [178].

In this contribution we propose a novel skeleton-based stabilization technique for isogeometric analysis of viscous flow problems, like those described by the Stokes equations and incompressible Navier-Stokes equations with moderate Reynold's numbers. The skeleton-based stabilization allows utilizing identical finite dimensional spaces for the approximation of the pressure and velocity fields. The central idea is to supplement the variational formulation with a consistent penalization term for the jumps of high-order derivatives of the pressure across element interfaces. By taking into account the local continuity at each element interface, the stabilized formulation can be applied to B-splines/NURBS with varying regularities, including the case of multi-patch geometries.

The proposed stabilization technique only controls the $(\alpha + 1)$-th order derivative in the case of B-splines/NURBS basis functions of degree k with C^α-regularity. Therefore it can be regarded as a generalization of the continuous interior penalty finite element method [40] where C^0 Lagrange basis functions are employed. This generalization enables the consideration of a large class of problems in isogeometric analysis for fluid flows. The present work encompasses a detailed study of the effect of the stabilization operator on the sparsity pattern of the mixed matrix – including an analysis of its complexity with respect to the B-splines/NURBS order – from which it is observed that the proposed technique optimally exploits the higher-order continuity properties of isogeometric analysis. We present a series of detailed numerical benchmark simulations to demonstrate the effectivity of the stabilization technique. In particular we show that oscillation-free solutions are attained, and the method yields optimal convergence rates under mesh refinements.

The outline of the paper is as follows. In Section 3.2 we recall the essential aspects of isogeometric analysis. In particular we introduce the skeleton structure and jump operators, and we discuss the local continuity properties across element interfaces. The skeleton-based isogeometric analysis technique for the Navier-Stokes equations is then introduced in Section 3.3. In Section 3.4 we discuss the matrix form and implementation aspects of the method, along with a study of the effect of the skeleton-stabilization operator on the sparsity pattern of the algebraic system. A series of numerical test cases is considered in Section 3.5 to demonstrate the performance of the proposed method. Conclusions are finally presented in Section 3.6.

3.2 Fundamentals of skeleton-based isogeometric analysis

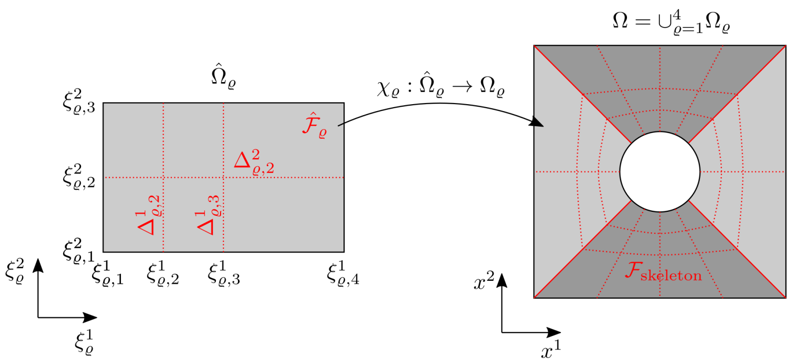

Fig. 3.1: Notations for a parameterization of a multipatch geometry.

To provide a setting for the skeleton-based stabilization proposed in Section 3.3 and to introduce the main notational conventions, we first present multi-patch non-uniform rational B-spline (NURBS) spaces. We consider a domain $\Omega \subset \mathbb{R}^d$ (with $d = 2$ or 3) with Lipschitz boundary $\partial\Omega$ as exemplified in Fig. 3.1. The domain Ω is parameterized by a, possibly multi-patch ($n_{\text{patch}} \geq 1$), non-uniform rational B-spline (NURBS) such that

$$\Omega = \bigcup_{\varrho=1}^{n_{\text{patch}}} \chi_\varrho \circ \widehat{\Omega}_\varrho, \tag{3.1}$$

where $\widehat{\Omega}_\varrho$ and χ_ϱ are the patch-wise geometric maps and parameter domains, respectively, with the parametric map defined as

$$\begin{cases} \chi_\varrho : \widehat{\Omega}_\varrho \rightarrow \Omega_\varrho, \\ \mathbf{x} = \sum_{I=1}^{n_\varrho} \widehat{R}_{\varrho,I}(\boldsymbol{\xi}_\varrho)\mathbf{X}_{\varrho,I}, \end{cases} \tag{3.2}$$

where $\{\widehat{R}_{\varrho,I} : \widehat{\Omega}_\varrho \to \Omega_\varrho\}_{I=1}^{n_\varrho}$ and $\{\mathbf{X}_{\varrho,I} \in \mathbb{R}^d\}_{I=1}^{n_\varrho}$ are the set of NURBS basis functions and the associated set of control points, respectively. The NURBS basis functions are constructed based on a set of non-decreasing knot vectors, $\{\Xi_\varrho^\delta\}_{\delta=1}^d$, with

$$\Xi_\varrho^\delta = [\underbrace{\xi_{\varrho,1}^\delta, \dots, \xi_{\varrho,1}^\delta}_{r_{\varrho,1}^\delta \text{times}}, \underbrace{\xi_{\varrho,2}^\delta, \dots, \xi_{\varrho,2}^\delta}_{r_{\varrho,2}^\delta \text{times}}, \dots, \underbrace{\xi_{\varrho,m_\varrho^\delta}^\delta, \dots, \xi_{\varrho,m_\varrho^\delta}^\delta}_{r_{\varrho,m_\varrho^\delta}^\delta \text{times}}], \tag{3.3}$$

such that the number of basis functions per patch is $n_\varrho = \otimes_{\delta=1}^d \{(\sum_{i=1}^{m_\varrho^\delta} r_{\varrho,i}^\delta) - k_\varrho^\delta - 1\}$, with k_ϱ^δ the degree of the spline in the direction δ ($\delta = 1, \dots, d$). Note that for open B-splines the multiplicity of the first and last knot values is equal to $r_{\varrho,1}^\delta = r_{\varrho,m_\varrho^\delta}^\delta = k_\varrho^\delta + 1$. The regularity of the basis in the parametric directions depends on the order and the multiplicity of the knot value: $\alpha_{\varrho,i}^\delta = k_\varrho^\delta - r_{\varrho,i}^\delta$ for $i = 1, \dots, m_\varrho^\delta$. On every patch the knot vectors partition the domain into a parametric mesh $\widehat{\mathcal{T}}_\varrho$. The corresponding partitioning of the domain Ω follows as

$$\mathcal{T}^h = \bigcup_{\varrho=1}^{n_{\text{patch}}} \chi_\varrho \circ \widehat{\mathcal{T}}_\varrho. \tag{3.4}$$

The superscript h indicates the dependence of the partition on a mesh (resolution) parameter $h > 0$. We associate with the mesh $\mathcal{T}^h$ the skeleton*:

$$\mathcal{F}_{\text{skeleton}}^h = \{\partial K \cap \partial K' \mid K, K' \in \mathcal{T}^h, K \neq K'\}. \tag{3.5}$$

Note that since the skeleton-based stabilization technique considered in this work pertains to inter-element continuity properties, the boundary faces are not incorporated in the skeleton. The skeleton (3.5) can be decomposed in the intra-patch skeleton, $\mathcal{F}_{\text{intra}}^h$, and the inter-patch skeleton, $\mathcal{F}_{\text{inter}}^h$:

$$\mathcal{F}_{\text{intra}}^h := \bigcup_{\varrho=1}^{n_{\text{patches}}} \chi_\varrho \circ \widehat{F}_\varrho \qquad \text{with} \quad \widehat{\mathcal{F}}_\varrho := \left\{\partial\widehat{K} \cap \partial\widehat{K'} \mid \widehat{K}, \widehat{K'} \in \widehat{\mathcal{T}}_\varrho,\ \widehat{K} \neq \widehat{K'}\right\}, \tag{3.6a}$$

$$\mathcal{F}_{\text{inter}}^h := \mathcal{F}_{\text{skeleton}}^h \setminus \mathcal{F}_{\text{intra}}^h. \tag{3.6b}$$

It evidently follows from these definitions that $\mathcal{F}_{\text{skeleton}}^h = \mathcal{F}_{\text{intra}}^h \cup \mathcal{F}_{\text{inter}}^h$ and $\mathcal{F}_{\text{intra}}^h \cap \mathcal{F}_{\text{inter}}^h = \emptyset$.

* This should not be confused with the topological skeleton concept in geometric modeling.

Continuity across a patch interface is achieved by matching the knot vectors associated with the two sides of the interface, and by making the corresponding control points on both patches coincident. In terms of the NURBS basis this is equivalent to linking the NURBS basis functions corresponding to the coincident control points. We denote the set of all basis functions over the domain Ω – where interface functions have been linked – by $\mathcal{R} := \{R_I : \Omega \to \mathbb{R}\}_{I=1}^{n}$. The space spanned by this basis is denoted by $\mathcal{S} := \operatorname{span}(\mathcal{R})$. Let us note that in the general case of a non-conforming muti-patch structure, multi-patch coupling techniques can be used such as the Nitsche's method [98, 165] or the isogeometric mortar method [101].

To define the regularity of the spline space $\mathcal{S}$ we introduce the plane (or line in the two-dimensional case) in the parameter domain of patch ϱ which is perpendicular to the δ-direction, with its coordinate ξ^δ equal to that of the knot value $\xi^\delta_{\varrho,i}$ (see Fig. 3.1):

$$\Delta^\delta_{\varrho,i} := \left\{ \boldsymbol{\xi} = (\xi^1, \ldots, \xi^d) \mid \xi^\delta = \xi^\delta_{\varrho,i} \text{ and } \xi^{\delta'} \in [\xi^{\delta'}_{\varrho,1}, \xi^{\delta'}_{\varrho,m^\delta_\varrho}] \text{ for } \delta' \neq \delta \right\}. \tag{3.7}$$

The regularity of the space $\mathcal{S}$ across an intra-patch face $F \in \mathcal{F}^h_{\text{intra}}$ can then be defined through the unique combination of the patch index ϱ, the direction δ, and the knot index i, such that the associated parametric face $\widehat{F}_\varrho$ resides in the plane $\Delta^\delta_{\varrho,i}$. In combination with the C^0-continuity condition across patch boundaries, the regularity of the faces $F \in \mathcal{F}^h_{\text{skeleton}}$ is then given by:

$$\alpha(F) := \begin{cases} \alpha^\delta_{\varrho,i}, & \exists!(\varrho,\delta,i) : \chi_\varrho^{-1} \circ F \subset \Delta^\delta_{\varrho,i}, \quad F \in \mathcal{F}^h_{\text{intra}}, \\ 0, & \qquad\qquad\qquad\qquad\qquad\quad\; F \in \mathcal{F}^h_{\text{inter}}. \end{cases} \tag{3.8}$$

For all functions $f \in \mathcal{S}$ the jumps of its k-th normal derivatives across an interface vanish in accordance with

$$[\![\partial^k_n f]\!] = 0, \quad 0 \leq k \leq \alpha(F), \tag{3.9}$$

where the jump for some function ϕ is defined as $[\![\phi]\!] \equiv [\![\phi]\!]_F := \phi^+ - \phi^-$, and the superscripts $+$ and $-$ refer to the traces of ϕ on the two opposite sides of F.

From (3.8) it is inferred that in the interior of a patch the regularity per direction is controlled by the knot vector multiplicity, while across patch boundaries merely C^0-continuity of the basis holds. We denote by $\mathcal{S}^k_\alpha$ the spline space with global isotropic degree k and per skeleton face regularity α

in accordance with definition (3.8). In the special case of a global intra-patch regularity $\bar{\alpha} \in \mathbb{N}$, *i.e.*, $\alpha(F) = \bar{\alpha},\ 0 \leq \bar{\alpha} \leq k-1\ \forall F \in \mathcal{F}^h_{\text{intra}}$ we denote the function space by $\mathcal{S}^k_{\bar{\alpha}}$. A special case of this function space is that in which full regularity is achieved, *i.e.*, $\bar{\alpha} = k-1$.

3.3 Skeleton-stabilized Isogeometric Analysis for the Navier-Stokes equations

In this section we introduce the skeleton-penalty formulation for the Navier-Stokes equations in the context of Isogeometric Analysis. We commence with the formulation of the time-dependent Navier-Stokes equations in Section 4.2.1. Next, we introduce the discrete skeleton-penalty formulation in Section 3.3.2.

3.3.1 The time-dependent Navier-Stokes equations

We consider the unsteady incompressible Navier-Stokes equations on the open bounded domain $\Omega \in \mathbb{R}^d$ (with $d = 2$ or 3). The Lipschitz boundary $\partial\Omega$ is split in two complementary open subsets Γ_D and Γ_N (such that $\overline{\Gamma_D} \cup \overline{\Gamma_N} = \partial\Omega$ and $\Gamma_D \cap \Gamma_N = \emptyset$) for Dirichlet and Neumann conditions, respectively. The outward-pointing unit normal vector to $\partial\Omega$ is denoted by $\mathbf{n}$. For any time instant $t \in [0,T)$ the Navier-Stokes equations for the velocity field $\mathbf{u} : \Omega \times [0,T) \to \mathbb{R}^d$ and pressure field $p : \Omega \times [0,T) \to \mathbb{R}$ read:

$$\begin{cases} \text{Find } \mathbf{u} : \Omega \times [0,T) \to \mathbb{R}^d, \text{ and } p : \Omega \times [0,T) \to \mathbb{R} \text{ such that:} & \\ \partial_t \mathbf{u} + \nabla \cdot (\mathbf{u} \otimes \mathbf{u}) - \nabla \cdot (2\mu \nabla^s \mathbf{u}) + \nabla p = \mathbf{f} & \text{in } \Omega \times (0,T), \\ \nabla \cdot \mathbf{u} = 0 & \text{in } \Omega \times (0,T), \\ \mathbf{u} = \mathbf{0} & \text{on } \Gamma_D \times (0,T), \\ 2\mu \nabla^s \mathbf{u} \cdot \mathbf{n} - p\mathbf{n} = \mathbf{h} & \text{on } \Gamma_N \times (0,T), \\ \mathbf{u} = \mathbf{u}_0 & \text{in } \Omega \times \{0\}. \end{cases} \tag{3.10}$$

Here μ represents the kinematic viscosity, and the symmetric gradient of the velocity field is denoted by $\nabla^s \mathbf{u} := \frac{1}{2}\left(\nabla \mathbf{u} + (\nabla \mathbf{u})^T\right)$. The exogenous data $\mathbf{f} : \Omega \times (0,\infty) \to \mathbb{R}^d$ and $\mathbf{h} : \Gamma_N \times (0,\infty) \to \mathbb{R}^d$, represent the body forces and Neumann conditions, respectively. Without loss of generality we herein assume the Dirichlet data to be homogeneous. The initial conditions in (4.1) are denoted by $\mathbf{u}_0 : \Omega \to \mathbb{R}^d$.

For any vector space $\mathcal{V}$, we denote by $\mathcal{L}(0,T;\mathcal{V})$ a suitable linear space of $\mathcal{V}$-valued functions on the time interval $(0,T)$. We consider the following weak formulation of (4.1):

$$\begin{cases} \text{Find } \mathbf{u} \in \mathcal{L}(0,T;\mathcal{V}_{0,\Gamma_D}) \text{ and } p \in \mathcal{L}(0,T;Q) \text{, given } \mathbf{u}(0) = \mathbf{u}_0, \\ \text{such that for almost all } t \in (0,T): \\ (\partial_t \mathbf{u}, \mathbf{w}) + c(\mathbf{u};\mathbf{u},\mathbf{w}) + a(\mathbf{u},\mathbf{w}) + b(p,\mathbf{w}) = \ell(\mathbf{w}) \;\forall \mathbf{w} \in \mathcal{V}_{0,\Gamma_D}, \\ \qquad\qquad\qquad\qquad\qquad\qquad b(q,\mathbf{u}) = 0 \qquad \forall q \in Q. \end{cases} \tag{3.11}$$

The trilinear, bilinear, and linear forms in this formulation are defined as

$$c(\mathbf{v};\mathbf{u},\mathbf{w}) := (\mathbf{v}\cdot\nabla\mathbf{u},\mathbf{w}), \tag{3.12a}$$

$$a(\mathbf{u},\mathbf{w}) := 2\mu\,(\nabla^s\mathbf{u},\nabla^s\mathbf{w}), \tag{3.12b}$$

$$b(q,\mathbf{w}) := -\,(q,\mathrm{div}\mathbf{w}), \tag{3.12c}$$

$$\ell(\mathbf{w}) := (\mathbf{f},\mathbf{w}) + \langle\mathbf{h},\mathbf{w}\rangle_{\Gamma_N}, \tag{3.12d}$$

where $(\cdot,\cdot)$ and $\langle\cdot,\cdot\rangle_{\Gamma_N}$ denote the inner product in $L^2(\Omega)$ and dual product in $L^2(\Gamma_N)$, respectively. The function spaces in (3.11) are defined as

$$\mathcal{V}_{0,\Gamma_D} := \left\{\mathbf{u} \in [H^1(\Omega)]^d : \mathbf{u} = \mathbf{0} \text{ on } \Gamma_D\right\}, \qquad Q := L^2(\Omega).$$

In the case of pure Dirichlet boundary conditions, *i.e.*, if Γ_D coincides with all of $\partial\Omega$, the pressure is determined up to a constant. In that case, the pressure space is subject to the zero average pressure condition:

$$Q := L_0^2(\Omega) \equiv \left\{q \in L^2(\Omega) : \int_\Omega q \,\mathrm{d}\Omega = 0\right\}. \tag{3.13}$$

3.3.2 The Isogeometric Skeleton-Penalty method with identical discrete spaces of velocity and pressure

In this contribution we study the discretization of (3.11) by utilizing identical spline discretizations for the velocity and pressure fields. The global isotropic order of the spline space is denoted by k and its regularity by α (with $0 \le \alpha(F) \le k-1 \;\forall F \in \mathcal{F}^h_{\text{skeleton}}$; see Section 3.2):

$$\mathcal{V}^h := \left[\mathcal{S}^k_\alpha\right]^d \cap \mathcal{V}_{0,\Gamma_D}, \qquad Q^h := \mathcal{S}^k_\alpha \cap Q. \tag{3.14}$$

The semi-discretization in space of the weak form (3.11) then reads:

$$\begin{cases} \text{Find } \mathbf{u}^h \in \mathcal{L}(0,T;\mathcal{V}^h) \text{ and } p^h \in \mathcal{L}(0,T;\mathcal{Q}^h), \text{ given } \mathbf{u}^h(0) = \mathbf{u}^h_0, \\ \text{such that for almost all } t \in (0,T): \\ (\partial_t \mathbf{u}^h, \mathbf{w}^h) + c(\mathbf{u}^h;\mathbf{u}^h,\mathbf{w}^h) + a(\mathbf{u}^h,\mathbf{w}^h) + b(p^h,\mathbf{w}^h) = \ell(\mathbf{w}^h) \; \forall \mathbf{w}^h \in \mathcal{V}^h, \\ \hfill b(q^h,\mathbf{u}^h) = 0 \qquad \forall q^h \in \mathcal{Q}^h. \end{cases} \tag{3.15}$$

The pair of spaces $(\mathcal{V}^h,\mathcal{Q}^h)$ in (4.12) does not satisfy the inf-sup condition, and hence the discretization in (3.15) is unstable. To stabilize the system, we propose to supplement the formulation with the skeleton-penalty term,

$$s(p^h,q^h) := \sum_{F\in\mathcal{F}^h_{skeleton}} \int_F \gamma\mu^{-1} h_F^{2\alpha+3} [\![\partial_n^{\alpha+1} p^h]\!][\![\partial_n^{\alpha+1} q^h]\!] d\Gamma, \tag{3.16}$$

where α is the regularity of the considered spline space at the element interface $F \in \mathcal{F}^h_{skeleton}$, $\gamma > 0$ is a global stabilization parameter, and h_F is a length scale associated with this element interface. Here we define this length scale as

$$h_F := \frac{|K_F^+|_d + |K_F^-|_d}{2|F|_{d-1}}, \tag{3.17}$$

where K_F^+ and K_F^- are two elements sharing the interface F, and $|\cdot|_d$ is the d-dimensional Hausdorff measure. The stabilized semi-discrete system – to which we refer as the *isogeometric skeleton-penalty formulation* for the Navier-Stokes equations – then reads:

$$\begin{cases} \text{Find } \mathbf{u}^h \in \mathcal{L}(0,T;\mathcal{V}^h) \text{ and } p^h \in \mathcal{L}(0,T;\mathcal{Q}^h), \text{ given } \mathbf{u}^h(0) = \mathbf{u}^h_0, \\ \text{such that for almost all } t \in (0,T): \\ (\partial_t \mathbf{u}^h, \mathbf{w}^h) + c(\mathbf{u}^h;\mathbf{u}^h,\mathbf{w}^h) + a(\mathbf{u}^h,\mathbf{w}^h) + b(p^h,\mathbf{w}^h) = \ell(\mathbf{w}^h) \; \forall \mathbf{w}^h \in \mathcal{V}^h, \\ \hfill b(q^h,\mathbf{u}^h) - s(p^h,q^h) = 0 \qquad \forall q^h \in \mathcal{Q}^h. \end{cases} \tag{3.18}$$

Remark 3.1. The power $2\alpha + 3$ associated with the interface length h_F in (4.15b) follows from scaling arguments. The global stabilization parameter γ depends on the utilized spline space S^p_α. For a sufficiently smooth pressure solution, viz. $p \in H^{\alpha+1}(\Omega)$, the stabilized formulation (3.18) is variationally consistent with the weak form (3.11).

Remark 3.2. A special case, which is very common for CAD models, is that in which the highest regularity spline space, S^k_{k-1}, is used within each patch of the domain, while C^0-continuity is established between patches. The skeleton-penalty term (4.15b) in this case reads:

$$
\begin{aligned}
s(p^h, q^h) := &\sum_{F \in \mathcal{F}^h_{intra}} \int_F \gamma \mu^{-1} h_F^{2k+1} [\![\partial_n^k p^h]\!] [\![\partial_n^k q^h]\!] d\Gamma \\
&+ \sum_{F \in \mathcal{F}^h_{inter}} \int_F \gamma \mu^{-1} h_F^{3} [\![\partial_n p^h]\!] [\![\partial_n q^h]\!] d\Gamma.
\end{aligned}
\tag{3.19}
$$

Remark 3.3. The formulation (3.18) based on the skeleton-penalty stabilization term (4.15b) can also be applied to Lagrange bases, which is – in terms of function spaces – equivalent with the special case corresponding to regularity $\alpha = 0$. In this case, only the jump of first order derivatives must be stabilized. This case is known as the continuous interior penalty finite element method [40]. For higher smoothness B-splines, S^k_α, with regularity $\alpha \geq 1$, the jump of first order derivatives vanishes, as a consequence of which the formulation in [40] cannot be applied. Thus, formulation (4.15b) is the high-regularity generalization of the continuous interior penalty finite element method. Note that although the formulation in [40] is equivalent to the special case of $\alpha = 0$, the use of higher-order Bézier elements instead of higher-order Lagrange elements affects the sparsity pattern (see Section 3.4.3).

Remark 3.4. The weak formulation of the steady Stokes problem associated with (3.11) is given by:

$$
\begin{cases}
\text{Find } \mathbf{u} \in \mathcal{V}_{0,\Gamma_D} \text{ and } p \in Q \text{ such that:} \\
a(\mathbf{u}, \mathbf{w}) + b(p, \mathbf{w}) = \ell(\mathbf{w}) \ \forall \mathbf{w} \in \mathcal{V}_{0,\Gamma_D}, \\
\qquad b(q, \mathbf{u}) = 0 \qquad \forall q \in Q.
\end{cases}
\tag{3.20}
$$

Similar to formulation (3.18), the isogeometric skeleton-penalty formulation for the Stokes equations reads:

$$
\begin{cases}
\text{Find } \mathbf{u}^h \in \mathcal{V}^h \text{ and } p^h \in Q^h \text{ such that:} \\
a(\mathbf{u}^h, \mathbf{w}^h) + b(p^h, \mathbf{w}^h) = \ell(\mathbf{w}^h) \ \forall \mathbf{w}^h \in \mathcal{V}^h, \\
\ b(q^h, \mathbf{u}^h) - s(p^h, q^h) = 0 \qquad \forall q^h \in Q^h.
\end{cases}
\tag{3.21}
$$

It is well-known that problem (3.20) is the first-order optimality condition for the saddle point $(\mathbf{u}, p)$ of the Lagrangian functional (see e.g. [13])

$$
\mathcal{L}(\mathbf{v}, q) = \frac{1}{2} a(\mathbf{v}, \mathbf{v}) + b(q, \mathbf{v}) - \ell(\mathbf{v}), \quad (\mathbf{v}, q) \in \mathcal{V}_{0,\Gamma_D} \times Q. \tag{3.22}
$$

Analogously, the stabilized discrete system (3.21) is related to the optimization problem for the modified Lagrangian functional

$$\mathcal{L}^h(\mathbf{v}^h, q^h) = \tfrac{1}{2}a(\mathbf{v}^h, \mathbf{v}^h) + b(q, \mathbf{v}^h) - \ell(\mathbf{v}^h) - J(q^h), \quad (\mathbf{v}^h, q^h) \in \mathcal{V}^h \times \mathcal{Q}^h, \tag{3.23}$$

with

$$J(q^h) = \frac{\gamma}{2} \sum_{F \in \mathcal{F}^h_{skeleton}} \int_F \mu^{-1} h_F^{2\alpha+3} \left| [\![\partial_n^{\alpha+1} q^h]\!] \right|^2 \, d\Gamma. \tag{3.24}$$

The stabilized discrete system (3.21) follows directly from the first-order optimality condition for this modified Lagrangian functional, and the stabilization term (4.15b) appears as the variational derivative of (3.24). From (3.24) it is seen that the stabilization term (4.15b) effectively leads to minimization of the jump of high-order derivatives of the pressure over the skeleton $\mathcal{F}^h_{skeleton}$ in a least-squares sense.

Remark 3.5. For quasi-uniform meshes, the length scale h_F can alternatively be defined as

$$h_F := \frac{|K_F^+|_d^{1/d} + |K_F^-|_d^{1/d}}{2}, \tag{3.25}$$

or, even simpler, as

$$h_F := \begin{cases} length(F) & d = 2, \\ diam(F) & d = 3. \end{cases} \tag{3.26}$$

The numerical results presented in Section 3.5 are based on definition (3.26).

3.4 The algebraic form of Skeleton-stabilized Isogeometric Analysis

In this section we discuss various algorithmic aspects of the proposed skeleton-based stabilization framework. In Section 3.4.1 we briefly discuss the employed solution procedure for the unsteady Navier-Stokes equations, after which the algebraic form of the formulation is introduced in Section 3.4.2. The effect of the proposed stabilization term on the sparsity pattern of the system matrix is then studied in detail in Section 3.4.3.

Input: $\mathbf{u}_0, \Delta t, \mathrm{tol}$ `# initial condition, time step, Picard tolerance`

`# Initialization at` $t = 0$

$\mathbf{u}^0 = \mathbf{u}_0$

`# Time iteration (`$\theta = \frac{1}{2}$`: Crank-Nicolson)`

for $\imath$ **in** $1, 2, \ldots$**:**

`# Picard iteration`

$\mathbf{u}^\imath_0 = \mathbf{u}^{\imath-1}$

$p^\imath_0 = p^{\imath-1}$ **if** $\imath > 1$ **else** 0

for $\jmath$ **in** $1, 2, \ldots$**:**

$$\begin{cases} \text{Find } (\mathbf{u}^\imath_\jmath, p^\imath_\jmath) \in \mathcal{V}^h \times Q^h \text{ such that } \forall (\mathbf{w}, q) \in \mathcal{V}^h \times Q^h: \\ \left(\frac{\mathbf{u}^\imath_\jmath - \mathbf{u}^{\imath-1}}{\Delta t}, \mathbf{w} \right) + \theta \left(c(\mathbf{u}^\imath_{\jmath-1}; \mathbf{u}^\imath_\jmath, \mathbf{w}) + a(\mathbf{u}^\imath_\jmath, \mathbf{w}) \right) \\ +(1-\theta) \left(c(\mathbf{u}^{\imath-1}; \mathbf{u}^{\imath-1}, \mathbf{w}) + a(\mathbf{u}^{\imath-1}, \mathbf{w}) \right) + b(p^\imath_\jmath, \mathbf{w}) = \theta \ell^\imath(\mathbf{w}) + (1-\theta)\ell^{\imath-1}(\mathbf{w}), \\ b(q, \mathbf{u}^\imath_\jmath) - s(p^\imath_\jmath, q) = 0. \end{cases}$$

if $\max\{\|\mathbf{u}^\imath_\jmath - \mathbf{u}^\imath_{\jmath-1}\|, \|p^\imath_\jmath - p^\imath_{\jmath-1}\|\} < \mathrm{tol}$**:**

break

end

end

end

Algorithm 1: Solution procedure for the unsteady Navier-Stokes equations

3.4.1 The unsteady Navier-Stokes solution procedure

We employ a standard solution procedure for the unsteady Navier-Stokes equations. Crank-Nicolson time integration is considered in combination with Picard iterations for solving the nonlinear algebraic problem in each time step. The employed solution strategy is summarized in Algorithm 1. We denote the constant time step size by Δt and the time step index by $\imath$, such that $t = \imath \Delta t$. The solution at time step $\imath$ is denoted by $(\mathbf{u}^\imath, p^\imath)$, and the time-dependence of the non-autonomous linear operator $\ell(\mathbf{w})$ is similarly indicated by a superscript: $\ell^\imath(\mathbf{w})$. The Picard iteration counter is denoted by $\jmath$, and the unresolved solution at iteration $\jmath$ by $(\mathbf{u}^\imath_\jmath, p^\imath_\jmath)$. Note that for the sake of notational brevity we here omit the superscript h from the variables.

3.4.2 The algebraic form

Let $\{\mathbf{R}_i^u\}_{i=1}^{n_u}$ and $\{R_i^p\}_{i=1}^{n_p}$ denote two sets of NURBS basis functions for the velocity and pressure fields, respectively. These basis functions span the discrete velocity and pressure spaces

$$\mathcal{V}^h = \text{span}\{\mathbf{R}_i^u\}_{i=1}^{n_u}, \qquad \mathcal{Q}^h = \text{span}\{R_i^p\}_{i=1}^{n_p}, \tag{3.27}$$

and, accordingly, the approximate velocity field $\mathbf{u}^h(\mathbf{x}, t)$ and pressure field $p^h(\mathbf{x}, t)$ can be written as

$$\mathbf{u}^h(\mathbf{x}, t) = \sum_{i=1}^{n_u} \mathbf{R}_i^u(\mathbf{x})\hat{u}_i(t), \qquad p^h(\mathbf{x}, t) = \sum_{i=1}^{n_p} R_i^p(\mathbf{x})\hat{p}_i(t), \tag{3.28}$$

where $\hat{\mathbf{u}}(t) = (\hat{u}_1, \hat{u}_2, \ldots, \hat{u}_{n_u})^T$ and $\hat{\mathbf{p}}(t) = (\hat{p}_1, \hat{p}_2, \ldots, \hat{p}_{n_p})^T$ are vectors of degrees of freedom. The corresponding algebraic form of (3.18) then reads

$$\begin{cases} \text{For each } t \in (0, T), \text{ find } \hat{\mathbf{u}} = \hat{\mathbf{u}}(t) \in \mathbb{R}^{n_u} \text{ and } \hat{\mathbf{p}} = \hat{\mathbf{p}}(t) \in \mathbb{R}^{n_p}, \\ \text{ given } \hat{\mathbf{u}}(0) = \hat{\mathbf{u}}_0, \text{ such that:} \\ \mathbf{M}\partial_t\hat{\mathbf{u}} + [\mathbf{C}(\hat{\mathbf{u}}) + \mathbf{A}]\,\hat{\mathbf{u}} + \mathbf{B}^T\hat{\mathbf{p}} = \mathbf{f}, \\ \qquad\qquad\qquad\qquad \mathbf{B}\hat{\mathbf{u}} - \mathbf{S}\hat{\mathbf{p}} = \mathbf{0}. \end{cases} \tag{3.29}$$

with the matrix entries given by:

$$A_{ij} = a(\mathbf{R}_j^u, \mathbf{R}_i^u), \tag{3.30a}$$

$$B_{ij} = b(R_i^p, \mathbf{R}_j^u), \tag{3.30b}$$

$$C(\hat{\mathbf{u}})_{ij} = c(\hat{\mathbf{u}}; \mathbf{R}_j^u, \mathbf{R}_i^u), \tag{3.30c}$$

$$S_{ij} = s(R_j^p, R_i^p), \tag{3.30d}$$

$$M_{ij} = (\mathbf{R}_j^u, \mathbf{R}_i^u), \tag{3.30e}$$

$$f_i = \ell(\mathbf{R}_i^u). \tag{3.30f}$$

The algebraic form of the solution Algorithm 1 is presented in Algorithm 2.

We note that computation of the stabilization matrix $\mathbf{S}$ requires a data structure related to the skeleton $\mathcal{F}_{skeleton}^h$ of the mesh $\mathcal{T}^h$. This data structure is constructed such that at each element interface $F \in \mathcal{F}_{skeleton}^h$, the jump of high-order derivatives of the basis functions over F can be evaluated. It should be noted that this skeleton structure is compatible with the recently proposed efficient row-by-row assembly procedure for IGA [117].

```
Input: û_0, Δt, tol                    # initial condition vector, time step, Picard tolerance
# Initialization at t = 0
û^0 = û_0
# Time iteration (θ = 1/2: Crank-Nicolson)
for ι in 1, 2, . . . :
    # Picard iteration
    û^ι_0 = û^{ι−1}
    p̂^ι_0 = p̂^{ι−1} if ι > 1 else 0
    for j in 1, 2, . . . :
        Obtain (û^ι_j, p̂^ι_j) by solving the linear system:
```

$$\begin{bmatrix} \frac{1}{\Delta t}\mathbf{M} + \theta\left((\mathbf{C}(\hat{\mathbf{u}}^{\iota}_{j-1}) + \mathbf{A}\right) & \mathbf{B}^T \\ \mathbf{B} & -\mathbf{S} \end{bmatrix} \begin{bmatrix} \hat{\mathbf{u}}^{\iota}_{j} \\ \hat{\mathbf{p}}^{\iota}_{j} \end{bmatrix} = \begin{bmatrix} \left(\frac{1}{\Delta t}\mathbf{M} - (1-\theta)\left(\mathbf{C}(\hat{\mathbf{u}}^{\iota-1}) + \mathbf{A}\right)\right)\hat{\mathbf{u}}^{\iota-1} + \theta\mathbf{f}^{\iota} + (1-\theta)\mathbf{f}^{\iota-1} \\ \mathbf{0} \end{bmatrix}$$

```
        if max{‖û^ι_j − û^ι_{j−1}‖, ‖p̂^ι_j − p̂^ι_{j−1}‖} < tol:
            break
        end
    end
end
```

Algorithm 2: Algebraic form of the solution procedure for the unsteady Navier-Stokes equations

3.4.3 The k/α-complexity of the skeleton-penalty operator on sparsity pattern

The skeleton-based stabilization operator (4.15b) affects the sparsity pattern of the discretized Navier-Stokes system due to the fact that the jump operators on the (higher-order) derivatives provide additional connectivity between basis functions. To illustrate this effect we consider the spline space $\mathcal{S}^k_\alpha$, for which the derivative of order $\alpha+1$ are stabilized. The top row of Fig. 4.6 shows univariate cubic B-spline bases with C^2, C^1, C^0-regularity, and C^0 Lagrange (from left to right). The second row plots the stabilized (order $\alpha+1$) derivatives for each basis. The third row shows the sparsity pattern of the skeleton-penalty matrix $\mathbf{S}$ associated with the operator $s(p^h, q^h)$.

The bandwidth[†] of the skeleton-penalty matrix $\mathbf{S}$ is equal to $\alpha+2$, which ranges from 2 for C^0-splines (or at patch interfaces) to a maximum of $k+1$ for splines with full continuity (typical for intra patch interfaces). This observed decrease in bandwidth with decrease in regularity stems from the fact that the

[†] The bandwidth is defined as the smallest non-negative integer b such that $S_{ij} = 0$ if $|i-j| > b$.

number of order $\alpha + 1$ derivatives of the basis functions that vanish on the interfaces increases with α. This behavior contrasts with classical C^0 Lagrange basis functions, for which the bandwidth is equal to $2k$ (the last column of Fig. 4.6). The resulting increase in bandwidth of the jump stabilization matrix with increase in Lagrange basis order is an important drawback of the interior penalty method compared to element-based stabilization techniques. By construction, B-spline bases ameliorate this issue in the sense that even at full continuity the bandwidth of the skeleton-penalty matrix is considerably smaller than that of the Lagrange basis of equal order. This advantage – which extends to higher dimensions – makes the proposed stabilization technique computationally practical for a wide range of applications.

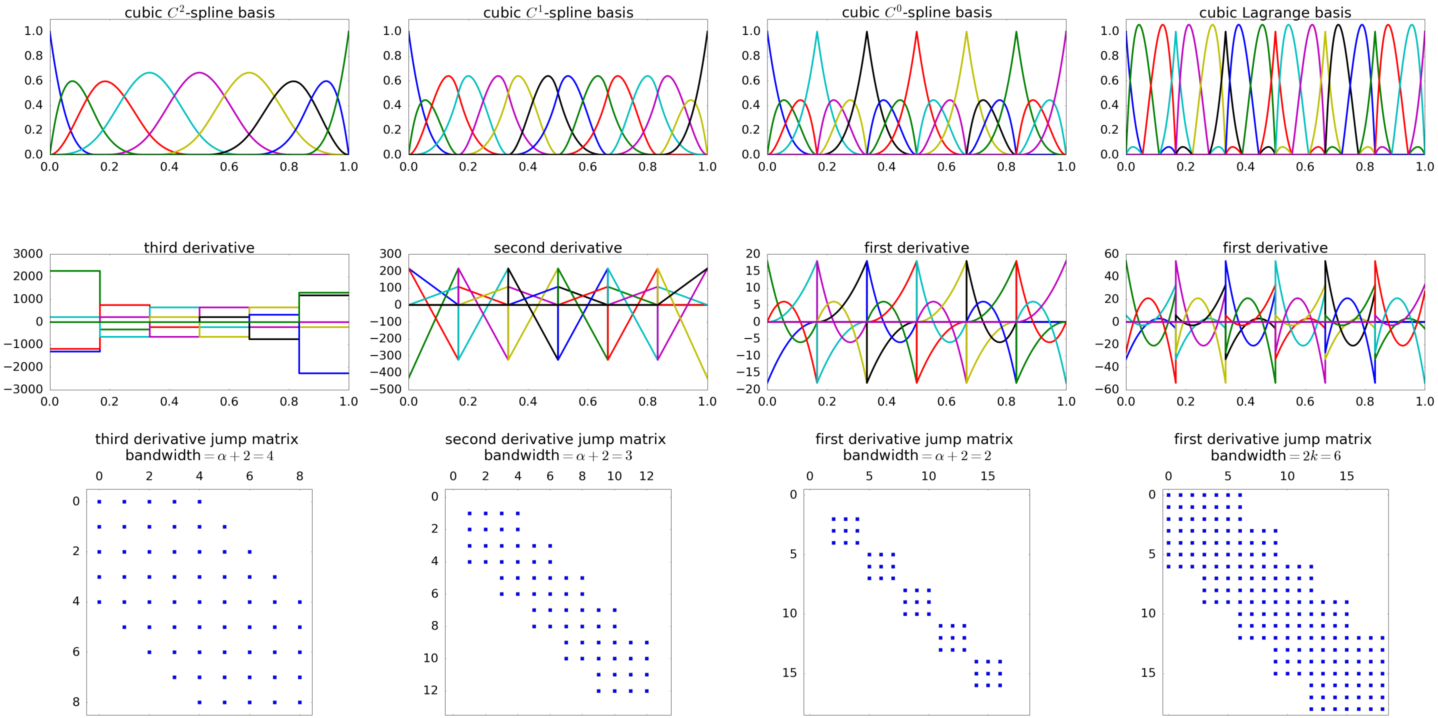

Fig. 3.2: Sparsity pattern of the skeleton-penalty matrix, illustrated with univariate cubic spaces: spline S^3_α space with full regularity $\alpha = 2$ (first column), reduced regularity $\alpha = 1$ (second column), minimal regularity $\alpha = 0$ (third column), and C^0 Lagrange space (last column). The top row shows the basis functions, the second row the stabilized (order $\alpha + 1$) derivatives, and the third row the matrix sparsity pattern of the skeleton-penalty matrix $\mathbf{S}$. The bandwidths of $\mathbf{S}$ in the spline cases are $\alpha + 2$, much smaller than in the Lagrange case $2k$.

3.5 Numerical experiments

In this section we investigate the numerical performance of the Skeleton-stabilized IsoGeometric Analysis framework for a range of numerical test cases for viscous flow problems. These test cases focus on various aspects of the framework, most notably its accuracy and convergence under mesh refinement, its stability, and its robustness with respect to the model parameters.

3.5.1 Steady Stokes flow in a unit square

We consider the steady two-dimensional Stokes problem – *i.e.,* problem (3.11) without time-dependent and convective terms – in the unit square domain $\Omega = (0, 1)^2$. The body force $\mathbf{f}$ is taken in accordance with the manufactured solution [118]:

$$\mathbf{u} = \begin{pmatrix} 2e^x(-1+x)^2x^2(y^2-y)(-1+2y) \\ (-e^x(-1+x)x(-2+x(3+x))(-1+y)^2y^2) \end{pmatrix} \tag{3.31a}$$

$$\begin{aligned} p = {} & (-424 + 156e + (y^2-y)(-456 + e^x(456 + x^2(228 - 5(y^2-y)) \\ & + 2x(-228 + (y^2-y)) + 2x^3(-36 + (y^2-y)) + x^4(12 + (y^2-y))))). \end{aligned} \tag{3.31b}$$

This manufactured solution is visualized in Fig. 3.3a. Note that homogeneous Dirichlet boundary conditions are imposed on the complete boundary $\partial\Omega$, and that a zero average pressure condition, $\int_\Omega p \, d\Omega = 0$, is imposed to establish well-posedness. We use a Lagrange multiplier approach to enforce this condition.

In Fig. 3.3 we study the asymptotic h-convergence behavior of the proposed method for B-splines of degree $k = 1, 2, 3$ with the highest possible regularities, *i.e.* C^{k-1}. The coarsest mesh considered consists of 4×4 elements, which is uniformly refined until a 128×128 mesh is obtained. The stabilization parameter is taken as $\gamma = 1$ ($k = 1$), 5×10^{-2} ($k = 2$), 10^{-3} ($k = 3$). The solution obtained using quadratic splines with 16×16 elements is shown in Fig. 3.3a. One can observe that both the pressure and velocity solutions are oscillation-free for all considered cases. Optimal convergence rates are obtained for both the velocity and the pressure field. For the L^2-norm and H^1-norm of the velocity error, Fig. 3.3b and 3.3c respectively, asymptotic rates of $k + 1$ and k are obtained. For the L^2-norm of the pressure shown in

Fig. 3.3d we observe asymptotic rates of approximately $k + \frac{1}{2}$, which is half an order higher than those of the H^1-norm of the velocity error. For inf-sup compatible discretization pairs where the degrees of the pressure and velocity spaces are $k - 1$ and k respectively, the rate of convergence of the L^2-norm of the pressure error is known to be equal to that of the H^1-norm of the velocity error. We attribute the improved rate for the pressure error using equal order spaces to the fact that compared to the compatible setting the pressure space is one order higher.

In Fig. 3.4 we study the sensitivity of the computed results with respect to the Skeleton-Penalty stabilization parameter γ. The h-convergence behavior of the solution using C^1-continuous quadratic B-splines is studied for a wide range of stabilization parameters, *viz.* $\gamma \in (5 \times 10^{-6}, 1)$. We observe that the stabilization parameter does not affect the accuracy of the velocity field in the L^2-norm and H^1-norm, see Fig. 4.10a and 4.10b, respectively. This is an expected results, as the introduced Skeleton-Penalty term acts only on the pressure field. The pressure solution accuracy is affected by the selection of the stabilization parameter, see Fig. 4.10c. Choosing γ too large will lead to ill-conditioning of the system, while taking γ too small will lead to loss of stability. Fig. 3.4 conveys, however, that the parameter can be selected from a wide range without a significant effect on the accuracy. For the case considered here accuracy deterioration remains very limited in the range $\gamma \in (5 \times 10^{-4}, 5 \times 10^{-2})$. Moreover, for all considered cases we observe the rate of convergence to be independent of the choice of γ.

The performance of the proposed Skeleton-stabilized IsoGeometric Analysis framework is further studied based on the generalized Stokes equations with homogeneous Dirichlet boundary conditions:

$$\begin{cases} \text{Find } \mathbf{u} : \overline{\Omega} \to \mathbb{R}^d, \text{ and } p : \overline{\Omega} \to \mathbb{R} \text{ such that:} \\ \sigma\mathbf{u} - \nabla \cdot (2\mu\nabla^s\mathbf{u}) + \nabla p = \mathbf{f} \quad \text{in } \Omega, \\ \qquad\qquad\qquad\qquad \nabla \cdot \mathbf{u} = 0 \quad \text{in } \Omega, \\ \qquad\qquad\qquad\qquad\quad \mathbf{u} = \mathbf{0} \quad \text{on } \Gamma_D, \end{cases} \tag{3.32}$$

This system – for which the body force $\mathbf{f}$ is selected in accordance with the manufactured solution (3.31) – is characterized by the Damköhler number

$$\mathrm{Da} = \frac{\sigma L^2}{\mu}, \tag{3.33}$$

where σ is the reaction coefficient, and L is a characteristic length scale for the problem (in this case the width/height of the unit square). In Fig. 3.5 we

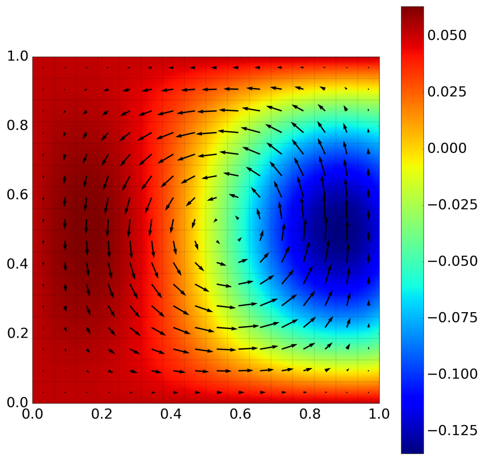

(a) Manufactured solution

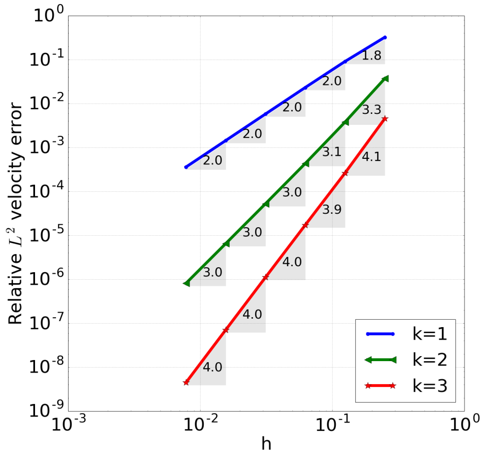

(b) L^2 velocity error

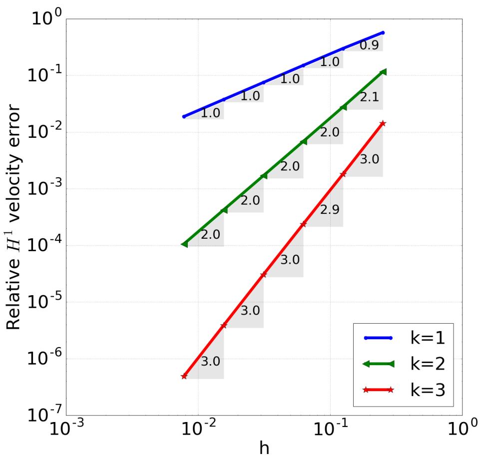

(c) H^1 velocity error

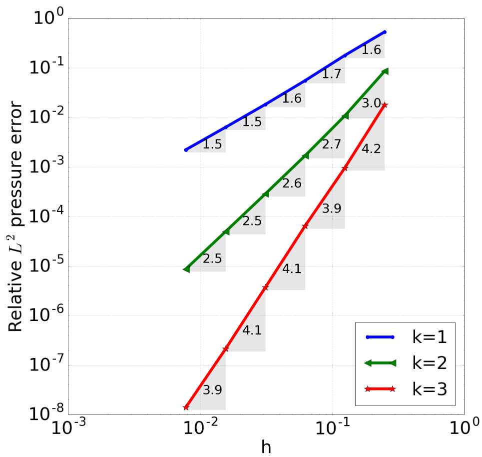

(d) L^2 pressure error

Fig. 3.3: (a) Solution for the steady Stokes problem in Section 3.5.1, pressure (color) and velocity (vector field). (b-d) Mesh convergence results for B-splines of order $k = 1, 2, 3$ and C^{k-1} regularity.

study the h-convergence behavior of C^{k-1}-continuous B-splines for various degrees $k = 1, 2, 3$ and $\mathrm{Da} = 1, 10, 1000$. To control the reaction term, we supplement the stabilization term with a contribution from σ to the scaling ratio, *i.e.*,

$$s(p^h, q^h) = \sum_{F \in \mathcal{F}^h_{skeleton}} \int_F \gamma(\mu + \sigma h_F^2)^{-1} h_F^{2\alpha+3} [\![\partial_n^{\alpha+1} p^h]\!] [\![\partial_n^{\alpha+1} q^h]\!] d\Gamma.$$

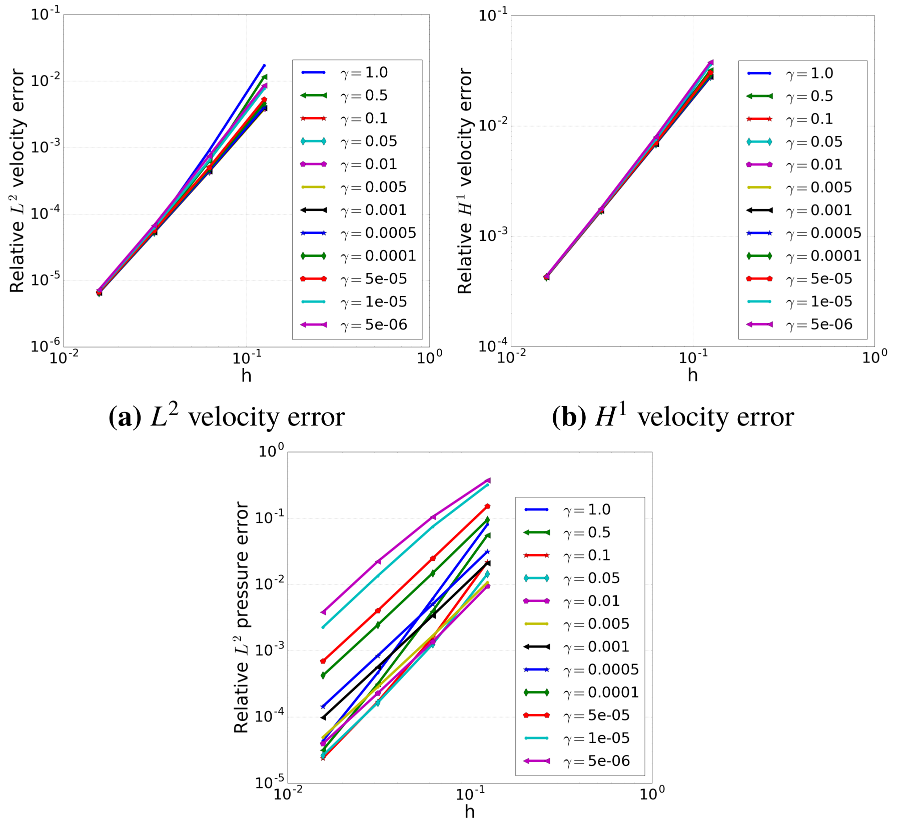

(a) L^2 velocity error **(b)** H^1 velocity error

(c) L^2 pressure error

Fig. 3.4: Sensitivity of the quadratic spline approximation of the Stokes problem on the unit square with respect to the stabilization parameter γ.

The stabilization parameter is now chosen equal to $\gamma = 1$ ($k = 1$), $5e-2$ ($k = 2$), $1e-3$ ($k = 3$). Note that the non-reactive case of Da $= 0$ corresponding to $\sigma = 0$ resembles the case considered above. For all considered cases we observe the approximation of the velocity solution and pressure solution to be virtually independent of the Damköhler number.

To understand the effect of reduced regularity – which is of particular importance in the case of multi-patch models – we first study the B-spline discretization of the Stokes problem on the unit square with varying intra-patch regularities. That is, we consider the spline discretizations S^k_α of order k with regularity $\alpha = 0, \ldots, k-1$. A stabilization parameter of $\gamma = 10^{-\alpha} k^{-4}$ – which effectively decreases the penalty parameter with increasing order and regularity – was found to yield an adequate balance between accuracy and

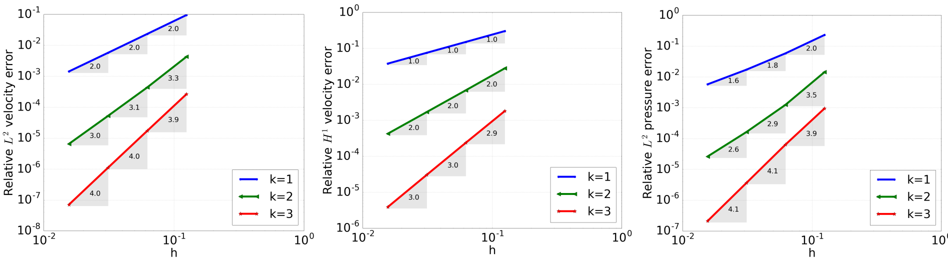

(a) Da = 1

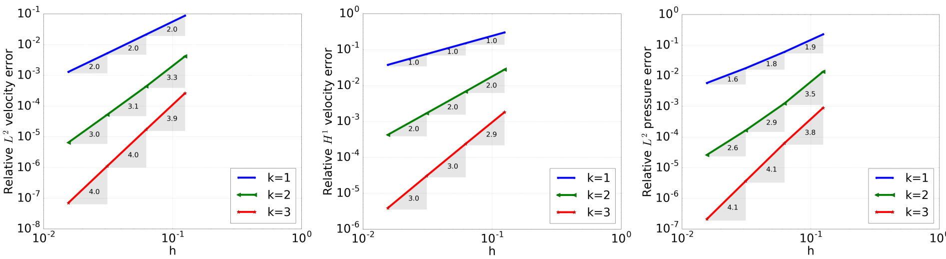

(b) Da = 10

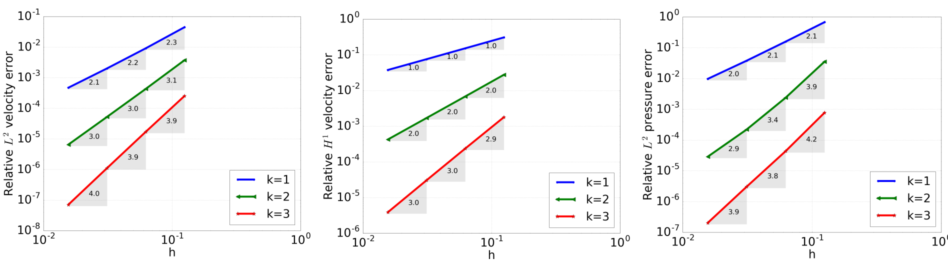

(c) Da = 1000

Fig. 3.5: h-convergence behavior of C^{k-1}-continuous B-spline spaces of degree $k = 1, 2, 3$ for various Damköhler numbers.

stability for the considered simulations. Derivation of a rigorous selection criterion for the penalty parameter is beyond the scope of the current work. Note that because the case of $k = 1$ and $\alpha = 0$ has already been considered above, we here restrict ourselves to the spline degrees $k = 2, 3, 4$. The h-convergence results are collected in Fig. 3.6. Note that we plot the errors versus the square root of the number of degrees of freedom to enable comparison of the various approximations. We observe optimal convergence rates for both the velocity and the pressure approximation for all cases. As anticipated the accuracy per degree of freedom improves with increasing regularity. Note that in the case of S_0^k – which is equivalent to the Lagrange basis – we observe similar approximation behavior as for the continuous interior-penalty method [40].

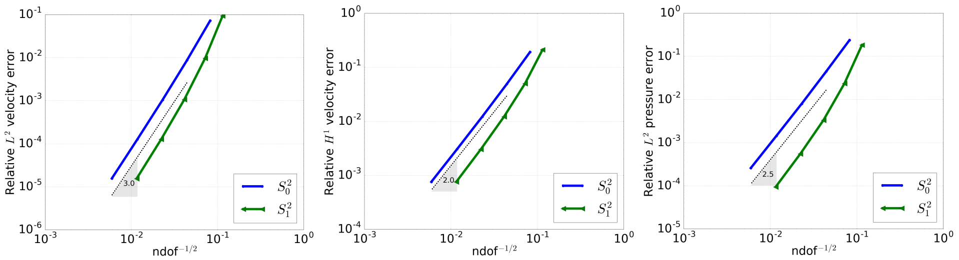

(a) $k = 2,\ \alpha = 0, 1$

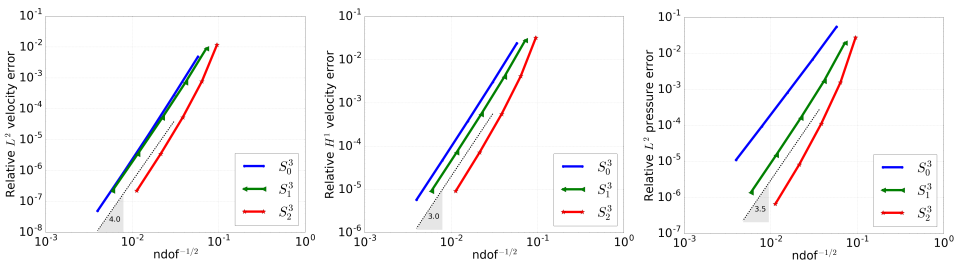

(b) $k = 3,\ \alpha = 0, 1, 2$

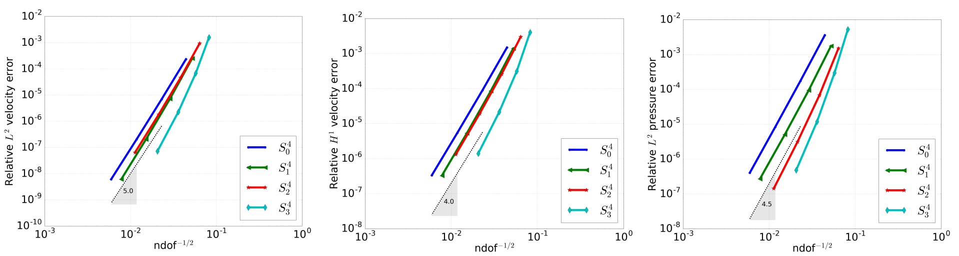

(c) $k = 4,\ \alpha = 0, 1, 2, 3$

Fig. 3.6: h-convergence results for the Stokes problem on a unit square using B-splines spaces S_α^k of various degrees $k = 2, 3, 4$ and regularities $0 \leq \alpha \leq k - 1$.

3.5.2 Steady Stokes flow in a quarter annulus ring

To demonstrate the performance of the proposed Skeleton-Penalty stabilization in the context of IsoGeometric Analysis, we consider the steady Stokes problem in the open quarter annulus domain

$$\Omega = \left\{ \mathbf{x} \in \mathbb{R}^2_{>0} : R_1 < |\mathbf{x}| < R_2 \right\},$$

with inner radius $R_1 = 1$ and outer radius $R_2 = 4$. We parametrize this domain using NURBS. Homogeneous Dirichlet boundary conditions are prescribed on the entire boundary $\partial\Omega = \Gamma_D$ and, accordingly, it holds that $\Gamma_N = \emptyset$. The body force $\mathbf{f}$ is selected in accordance with the manufactured solution [174, 179]

$$\mathbf{u}(\mathbf{x}) = \begin{pmatrix} 10^{-6}x^2y^4(x^2+y^2-1)(x^2+y^2-16)(5x^4+18x^2y^2-85x^2+13y^4-153y^2+80) \\ 10^{-6}xy^5(x^2+y^2-1)(x^2+y^2-16)(102x^2+34y^2-10x^4-12x^2y^2-2y^4-32) \end{pmatrix}, \tag{3.34a}$$

$$p(\mathbf{x}) = 10^{-7}xy(y^2-x^2)(x^2+y^2-16)^2(x^2+y^2-1)^2 \exp\left(14(x^2+y^2)^{-1/2}\right). \tag{3.34b}$$

Note that $\mathbf{u}$ vanishes on $\partial\Omega$ in accordance with the Dirichlet boundary condition. Moreover, the pressure complies with $\int_\Omega p \, d\Omega = 0$. This manufactured solution is illustrated in Fig. 3.7.

In this example we consider B-spline bases of orders $k = 1, 2, 3$ on meshes ranging from 8×8 to 128×128 elements. We divert here from the isoparametric concept in order to also study the performance of linear bases, which are incapable of parametrizing the annulus ring exactly. We will consider NURBS-based isogeometric analysis in later test cases. For the simulation, the stabilization parameter is taken as $\gamma = 1$ ($k = 1$), $5 \cdot 10^{-2}$ ($k = 2$), $1 \cdot 10^{-3}$ ($k = 3$). In Fig. 3.7a the pressure solution obtained using C^1-continuous quadratic B-splines on a 32×32 element mesh is shown, which is observed to be free of oscillations. In Fig. 3.7b and 3.7c we observe optimal convergence rates for the velocity error of $k+1$ for the L^2-norm and k for the H^1-norm, respectively. As for the unit square problem considered above, an asymptotic rate of convergence of approximately $k + \frac{1}{2}$ is observed for the L^2-norm of the pressures.

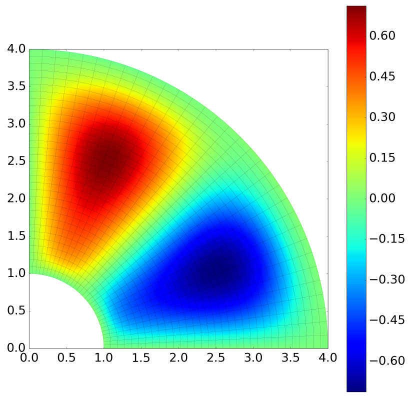

(a) Manufactured solution

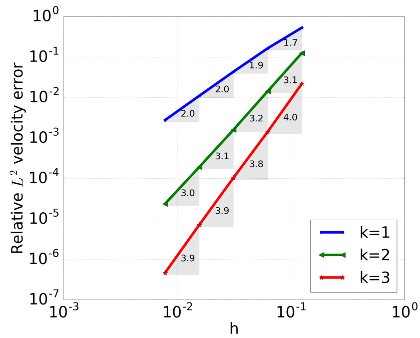

(b) L^2 velocity error

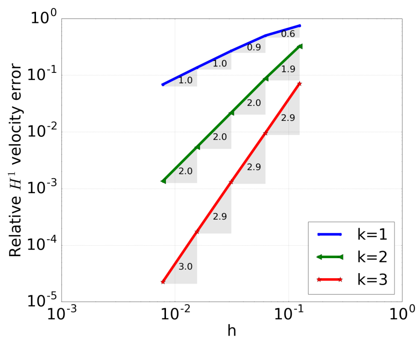

(c) H^1 velocity error

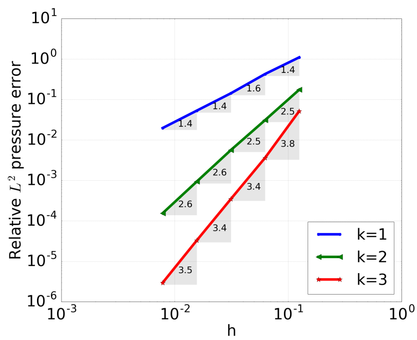

(d) L^2 pressure error

Fig. 3.7: (a) Pressure solution for the steady Stokes problem on a quarter annulus ring in Section 3.5.2. (b-d) h-convergence results for B-splines of order $k = 1, 2, 3$ and C^{k-1} regularity.

3.5.3 Steady Navier-Stokes flow in a full annulus domain

As the baseline test case for the Skeleton-stabilized IsoGeometric analysis of the steady incompressible Navier-Stokes equations we consider the cylindrical Couette flow between two cylinders as shown in Fig. 3.8a, which was studied in the context of compatible spline discretizations in [122]. The outer cylinder is fixed, while the inner cylinder rotates with surface velocity $U = \omega R_1$. For low Reynolds numbers the flow in between the cylinders will remain steady, two-dimensional, and axisymmetric. The analytical velocity solution of the problem is then given by

$$u = \begin{pmatrix} -(Ar + Br^{-1})\sin(\theta) \\ (Ar + Br^{-1})\cos(\theta) \end{pmatrix}, \tag{3.35}$$

where (r, θ) are the polar coordinates originating from the center of the cylinders, and

$$A = -U\frac{\delta^2}{R_1(1-\delta^2)}, \qquad B = U\frac{R_1}{1-\delta^2}, \tag{3.36}$$

with $\delta = R_1/R_2$ the ratio of radii of the inner and outer cylinders. The analytical pressure solution is a constant function, which supplemented with the zero average pressure condition $\int_\Omega p\, d\Omega = 0$ results in a zero pressure field. Here we consider the case of $\omega = 1$, $R_1 = 1$, and $R_2 = 2$. The solution for this case is illustrated in Fig. 3.8c.

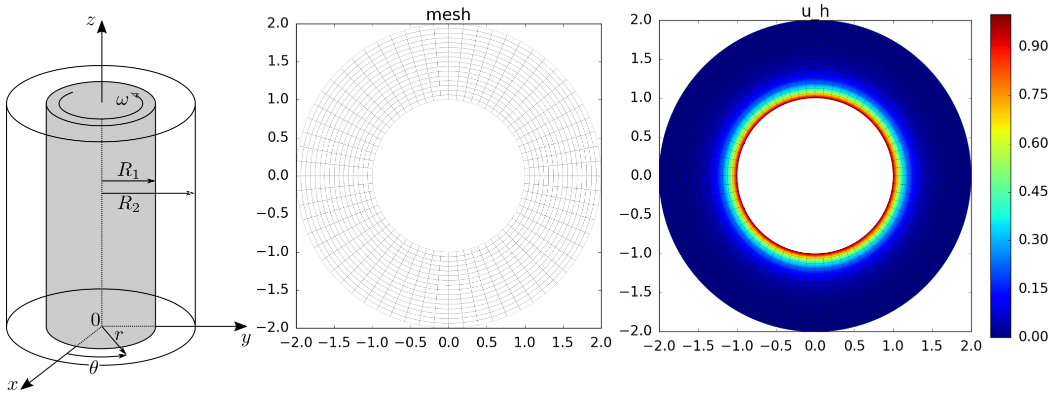

Fig. 3.8: (a) Setup of the cylindrical Couette flow problem. (b) Two-dimensional polar mesh, and (c) a typical solution of the radial velocity component.

For the parametrization of the geometry the polar map

$$(0,1)^2 \ni (\xi_1, \xi_2) \mapsto \mathbf{F}(\xi_1, \xi_2) = \begin{pmatrix} ((R_2 - R_1)\xi_2 + R_1)\sin(2\pi\xi_1) \\ ((R_2 - R_1)\xi_2 + R_1)\cos(2\pi\xi_1) \end{pmatrix} \tag{3.37}$$

is used, where (ξ_1, ξ_2) are the coordinates of the unit square parameter domain. The problem is discretized using B-splines of degree $k = 1, 2, 3$ with C^{k-1}-regularity, which are periodic in the circumferential ξ_1-direction. In Fig. 3.9 we study the mesh convergence behavior of the velocity approximation in the L^2-norm and H^1-norm. The coarsest mesh considered consists of 8×2

elements (two elements in the radial direction), which is uniformly refined until a mesh of 128×32 elements is obtained. We observed optimal rates of convergence for all orders in both the L^2-norm and H^1-norm. The pre-asymptotic behavior observed for the H^1-norm is a result of the fact that the boundary layer near the inner circle is not even remotely resolved by a single element. By virtue of the nature of the problem, the analytical zero pressure field is satisfied identically.

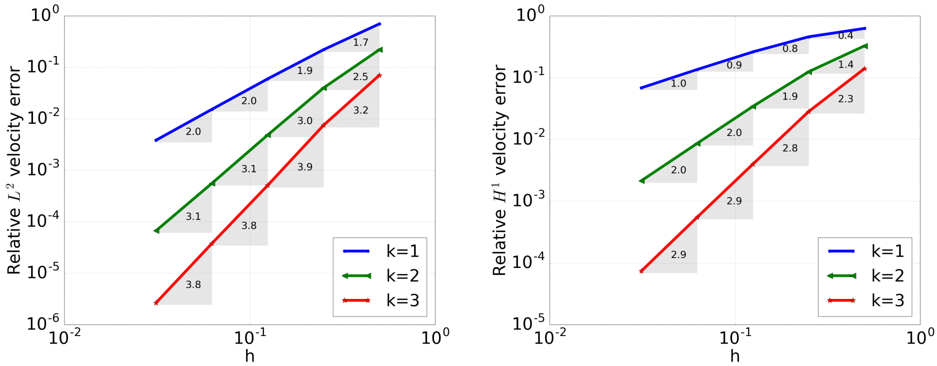

(a) L^2 velocity error

(b) L^2 velocity error

Fig. 3.9: h- convergence study of the cylindrical Couette flow problem using various order B-splines with C^{k-1} regularity.

3.5.4 Navier-Stokes flow around a circular cylinder

To study the performance of the proposed formulation for the Navier-Stokes equations in further detail we consider the benchmark problem proposed by Schäfer and Turek [180]. In this benchmark the flow around a cylinder which is placed in a channel is studied. The geometry of this test case is shown in Fig. 3.10, where the channel length is $L = 2.2\,\mathrm{m}$, the channel height is $H = 0.41\,\mathrm{m}$, and the cylinder radius is $R = 0.05\,\mathrm{m}$. The center of the cylinder is positioned at $\frac{1}{2}(W, W) = (0.2, 0.2)\,\mathrm{m}$, which has an offset of $\frac{1}{2}\delta = 0.005\,\mathrm{m}$ with respect to the center line of the channel (such that $W = H - \delta = 0.4\,\mathrm{m}$). At the inflow boundary ($x = 0$) a parabolic horizontal flow profile is imposed

$$\mathbf{u}(0, y) = \begin{pmatrix} 4U_m y(H - y)/H^2 \\ 0 \end{pmatrix}$$

with maximum velocity U_m. A no slip boundary condition is imposed along the bottom and top boundaries, as well as along the surface of the cylinder. At the outflow boundary ($x = L$) a zero traction boundary condition is used. The density and kinematic viscosity of the fluid are taken as $\rho = 1.0\,\mathrm{kg/m^3}$ and $\mu = 1 \times 10^{-3}\,\mathrm{m^2/s}$, respectively.

We consider two cases, one corresponding to an inflow velocity that results in a steady flow, and one corresponding to an inflow velocity that results in an unsteady flow. These two cases are characterized by the Reynolds number

$$\mathrm{Re} = \frac{2\bar{U}R}{\mu},$$

where $\bar{U} = \frac{2}{3}U_m$ is the mean inflow velocity. As quantities of interest we consider the drag and lift coefficients

$$c_D = \frac{F_D}{\rho \bar{U} R}, \qquad c_L = \frac{F_L}{\rho \bar{U} R},$$

where F_D and F_L are the resultant lift and drag forces acting on the cylinder. These forces are weakly evaluated as (see *e.g.*, [181])

$$F_D = \mathcal{R}(\mathbf{u}, p; \boldsymbol{\ell}_1), \qquad F_L = \mathcal{R}(\mathbf{u}, p; \boldsymbol{\ell}_2),$$

where

$$\mathcal{R}(\mathbf{u}, p; \boldsymbol{\ell}_i) := (\partial_t \mathbf{u}, \boldsymbol{\ell}_i) + c(\mathbf{u}; \mathbf{u}, \boldsymbol{\ell}_i) + a(\mathbf{u}, \boldsymbol{\ell}_i) + b(p, \boldsymbol{\ell}_i),$$

with $\boldsymbol{\ell}_i \in [H^1_{0,\partial\Omega\setminus\Gamma}(\Omega)]^d$ and $\boldsymbol{\ell}_i|_\Gamma = -\mathbf{e}_i$, $i = 1, 2$. We note that these lift and drag evaluations are consistent with the weak formulation (3.18), and are different from the formulations given in [182] and [183] where in the former, the time derivative term is neglected (so only consistent for the steady case), and in the latter, both the convective term and time derivative term are neglected (thus only consistent for the case of steady Stokes equations). For the steady test case, we also consider the pressure drop over the cylinder

$$\Delta p = p(W/2 - R, W/2) - p(W/2 + R, W/2),$$

and for the unsteady test case, we consider the Strouhal number

$$St = \frac{Df}{\bar{U}}$$

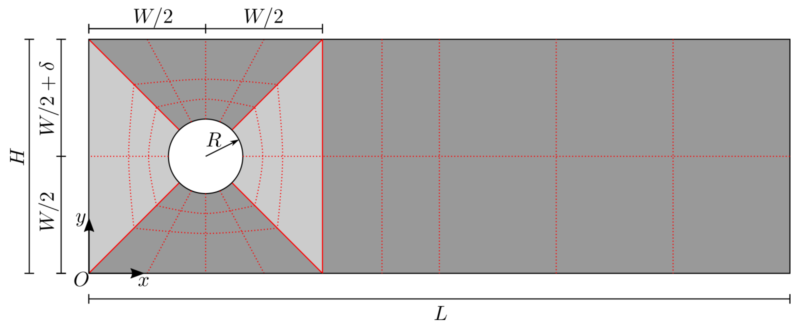

Fig. 3.10: Multi-patch parametrization of the channel flow problem with a circular obstacle.

as additional quantities of interest, where f is the frequency of vortex shedding and D is the diameter of the cylinder.

The geometry is parameterized by a quadratic ($k = 2$) multi-patch NURBS surface, as shown schematically in Fig. 3.10. The boundaries between the five patches are indicated by the solid red lines, while the element boundaries within the patches are marked by dashed red lines. Full C^{k-1}-continuity is maintained at the intra-patch element boundaries. For the coarsest mesh we employ 8×5 elements in the circumferential and radial direction, respectively, for each of the four patches adjacent to the cylinder. The discretization of the downstream patch conforms with its neighboring patch and consists of 8×8 elements in the vertical and horizontal direction, respectively. The employed NURBS are non-uniform as the meshes are locally refined toward the cylinder, and coarsened toward the outflow boundary.

We discretize both the velocity components and the pressure using the NURBS basis employed for the geometry parametrization, making this a true isogeometric analysis. Our coarsest quadratic NURBS mesh is refined uniformly to study the h-convergence behavior of the above-mentioned quantities of interest. Moreover, we elevate the order of our coarsest mesh to a cubic ($k = 3$) multi-patch NURBS surface with C^{k-1}-continuity inside the patches, and subsequently perform uniform mesh refinements to study the h-convergence behavior for the cubic case.

3.5.4.1 Steady flow

We first consider the case of Reynolds number Re $= 20$, for which a steady flow develops. The velocity magnitude and pressure solutions for this case are shown in Fig. 3.11. A two times uniform refinement of the coarsest quadratic NURBS mesh is used to compute this result, which contains $n_{\text{dof}} = 12180$ degrees of freedom. The computed drag and lift coefficients, $c_D = 5.5798$ and $c_L = 0.010605$, are in excellent agreement, respectively, with the benchmark ranges (5.57, 5.59), and (0.0104, 0.0110) reported in [180], as is the computed solution for the pressure drop $\Delta p = 0.117514$.

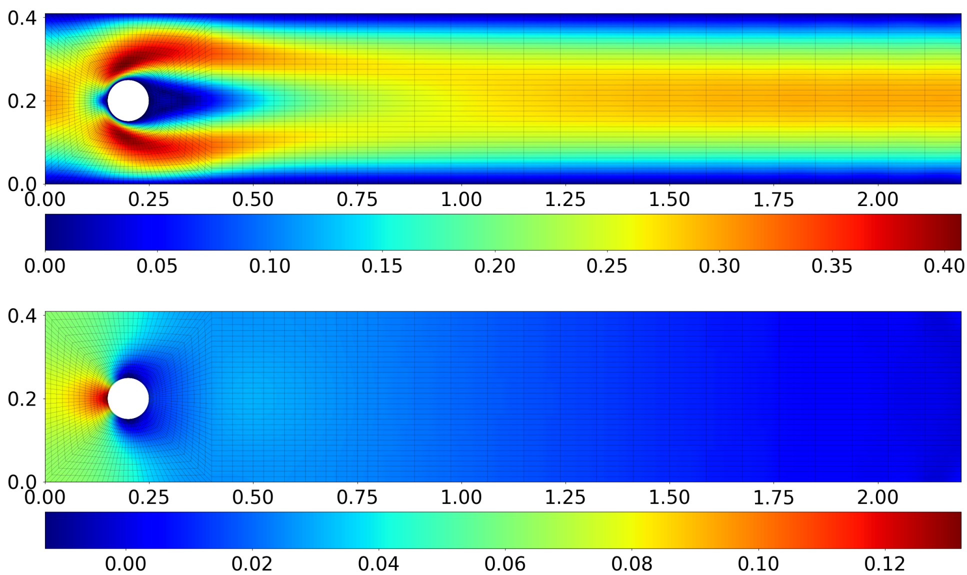

Fig. 3.11: Velocity magnitude (top) and pressure (bottom) solutions of the steady cylinder flow problem using quadratic NURBS with $n_{\text{dof}} = 12180$.

In Fig. 3.12 we present the h-convergence results for the three quantities of interest. For the quadratic case in Fig. 3.12a we consider five meshes, where the coarsest one corresponding to the geometry parameterization, results in 1056 degrees of freedom, and the four times uniformly refined mesh results in 177636 degrees of freedom. The errors are computed with respect to the high-quality reference values proposed in [184]:

$$C_D^{ref} = 5.57953523384, \quad C_L^{ref} = 0.010618948146, \quad \Delta_p^{ref} = 0.11752016697$$

We observe convergence of all three quantities of interest to the benchmark solutions. In particular for the lift coefficient and the pressure drop the observed asymptotic rates match well with the expected optimal rates of $2k$ [185]. In Fig. 3.12b we consider the mesh convergence of the quantities of interest for the cubic NURBS case, for which the coarsest mesh consists of 1356 degrees of freedom, and the finest mesh (4 uniform refinements) consists of 181356 degrees of freedom. As expected we observed improved rates of convergence compared to the quadratic case. Note that in terms of degrees of freedom there is virtually no difference between the finest quadratic mesh and the finest cubic mesh, which conveys that increasing the spline order is favorable from an accuracy per degree of freedom point of view. We expect that the irregular behavior of the convergence rate for the lift coefficient on the finest cubic meshes is related to approaching the accuracy of the reference solution from [184].

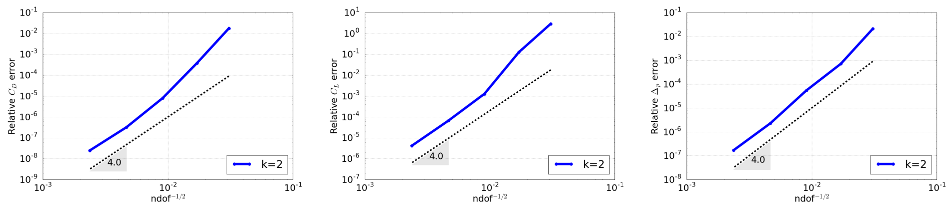

(a) Quadratic ($k = 2$) NURBS

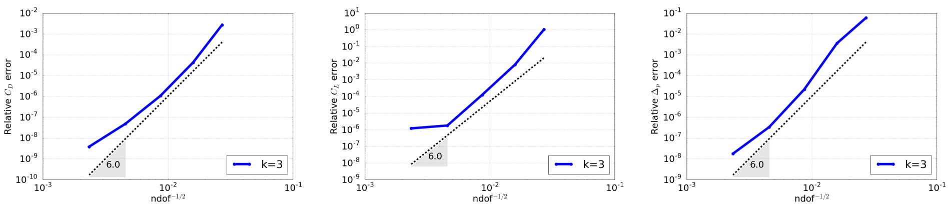

(b) Cubic ($k = 3$) NURBS

Fig. 3.12: h- convergence results for the drag coefficient (left column), lift coefficient (middle column) and pressure drop (right column) of the steady cylinder flow problem for quadratic (top row) and cubic (bottom row) NURBS.

3.5.4.2 Unsteady flow

For the case of Reynolds number $\mathrm{Re} = 100$ there is no longer a steady solution. Instead, once the flow is fully developed, oscillatory vortex shedding occurs, as illustrated by the snapshot shown in Fig. 3.13. For this figure, a two times uniformly refined quadratic NURBS parametrization is used, which results in a total of 12180 degrees of freedom. In order to capture the vortex shedding, the downstream mesh characteristics have been adjusted in comparison to the steady test case, in the sense that the refinement zone stretches out further behind the cylinder. We have used a time step of $\Delta t = 1/20$ s for the first 4 s of the simulations in order to let the flow develop, after which we switch to a smaller time step size of $\Delta t = 1/200$ s to accurately capture the oscillatory behavior of the solution. In Fig. 3.14 the evolution of the drag coefficient, lift coefficient and pressure drop over time is shown for the fully developed vortex shedding flow.

Table 3.1 presents a comparision result for three consecutive uniform mesh refinement levels using quadratic NURBS and $\Delta t = 1/200$ s. The flow is only considered when it is fully developed. The time cycle is arbitrarily chosen such that at the start and end of the interval, the lift coefficients attain two consecutive local minima. The quantities of interest are the minimum and maximum of the lift and drag coefficients, the length of the time cycle, and the Strouhal number. From Table 3.1, we compute Table 3.2, which shows the relative errors of the quantities of interest (and their convergence rates). We observe that these quantities of interest converge very well to the high-quality results reported in [186]. At the first level of refinement with only 3420 degrees of freedom, the results already start to be closed to the reference values, with the relative errors of 5.53×10^{-3} and 8.96×10^{-3} for the minimum and maximum of the drag coefficient, and approximately 8×10^{-2} for the minimum and maximum of the lift coefficient. At the third level of refinement with 45828 degrees of freedom, when the mesh is fine enough to resolve the boundary layer around the cylinder, and to accurately capture the dynamics of the flow, we obtain the convergence rates of $2k$ ($k = 2$) as in the steady test case, with errors of 1.34×10^{-4} and 8.08×10^{-5} for the minimum and maximum of the drag coefficient, and 1.49×10^{-3} and 1.12×10^{-3} for the minimum and maximum of the lift coefficient, respectively.

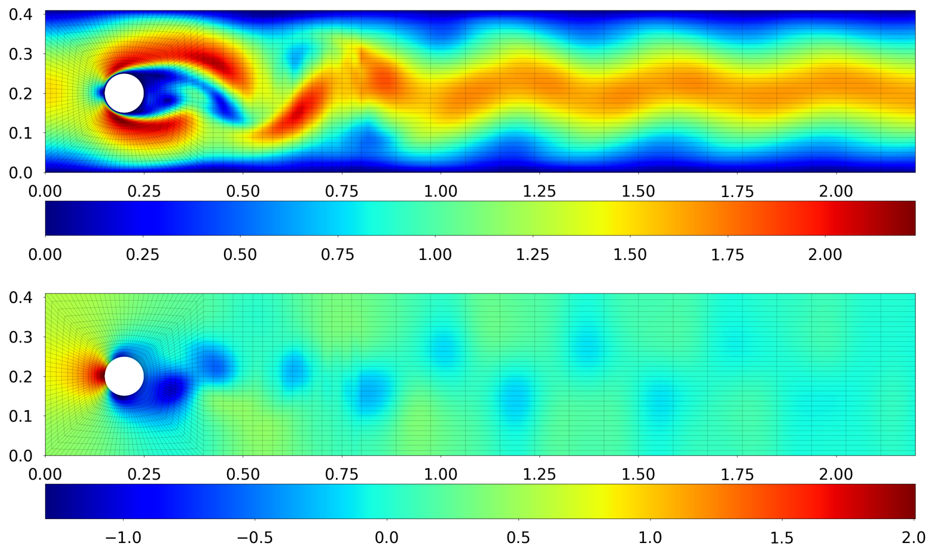

Fig. 3.13: A snapshot of velocity (top) and pressure (bottom) of the unsteady cylinder flow problem (Re=100); A Von Kármán vortex street is clearly visible behind the cylinder.

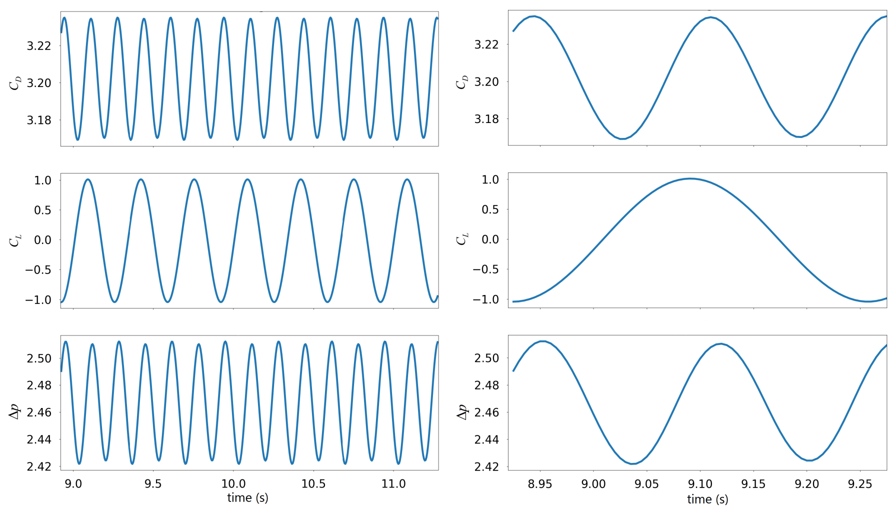

Fig. 3.14: Drag coefficient, lift coefficient and pressure drop over time (left) and a zoom of one period (right) for the unsteady cylinder flow problem. These results are based on a quadratic NURBS $k = 2$ discretization with two levels of refinements from the coarsest mesh.

Table 3.1: Minimum and maximum of the drag and lift coefficients, time cycle length, and the Strouhal number for the unsteady cylinder flow problem. For all cases the degree is $k = 2$ and the time step size is $\Delta t = 1/200$.

Level	n_{dof}	min C_D	max C_D	min C_L	max C_L	$1/f$	St
1	3420	3.18175	3.25632	-1.10535	1.06472	0.34500	0.28986
2	12180	3.16893	3.23507	-1.04482	1.00895	0.33500	0.29851
3	45828	3.16469	3.22765	-1.01977	0.98547	0.33000	0.30303
Ref [186]:	6 667264	3.16426	3.22739	-1.02129	0.98657	0.33125	0.30189

Table 3.2: Relative error convergence of the minimum and maximum of the drag and lift coefficients of the unsteady cylinder flow problem, computed from Table 3.1. For all cases the degree is $k = 2$ and the time step size is $\Delta t = 1/200$. The rate of convergence is here indicated by r.

Level	n_{dof}	error min C_D	error max C_D	error min C_L	error max C_L
1	3420	5.53×10^{-3}	8.96×10^{-3}	8.23×10^{-2}	7.92×10^{-2}
2	12180	1.47×10^{-3} ($r = 2.08$)	2.38×10^{-3} ($r = 2.09$)	2.30×10^{-2} ($r = 2.00$)	2.26×10^{-2} ($r = 1.97$)
3	45828	1.34×10^{-4} ($r = 3.62$)	8.08×10^{-5} ($r = 5.11$)	1.49×10^{-3} ($r = 4.14$)	1.12×10^{-3} ($r = 4.54$)

3.5.5 Three-dimensional Navier-Stokes flow in a sphere

To demonstrate the performance of the Skeleton-Penalty formulation in the three-dimensional case, we consider the 3D benchmark problem of Navier-Stokes flow proposed by Ethier and Steinman in [187] with the domain considered a sphere. We parametrize the spherical geometry by mapping a bi-unit cube parameter domain $\hat{\Omega} = (-1, 1)^3 \ni \boldsymbol{\xi}$ onto the physical domain $\Omega \ni \mathbf{x}$ through

$$\mathbf{x} = \begin{pmatrix} \xi_1\sqrt{1 - \frac{\xi_2^2}{2} - \frac{\xi_3^2}{2} + \frac{\xi_2^2\xi_3^2}{3}} \\ \xi_2\sqrt{1 - \frac{\xi_3^2}{2} - \frac{\xi_1^2}{2} + \frac{\xi_3^2\xi_1^2}{3}} \\ \xi_3\sqrt{1 - \frac{\xi_1^2}{2} - \frac{\xi_2^2}{2} + \frac{\xi_1^2\xi_2^2}{3}} \end{pmatrix}. \tag{3.38}$$

We consider the manufactured solution

$$\mathbf{u}(\mathbf{x}) = \begin{pmatrix} -a[e^{ax}\sin(ay+dz) + e^{az}\cos(ax+dy)] \\ -a[e^{ay}\sin(az+dx) + e^{ax}\cos(ay+dz)] \\ -a[e^{az}\sin(ax+dy) + e^{ay}\cos(az+dx)] \end{pmatrix}, \tag{3.39a}$$

$$\begin{aligned} p(\mathbf{x}) = -\frac{a^2}{2}\big[& e^{2ax} + e^{2ay} + e^{2az} + 2\sin(ax+dy)\cos(az+dx)e^{a(y+z)} \\ & + 2\sin(ay+dz)\cos(ax+dy)e^{a(z+x)} + 2\sin(az+dx)\cos(ay+dz)e^{a(x+y)}\big]. \end{aligned} \tag{3.39b}$$

with parameters $a = 1$ and $d = 1$.

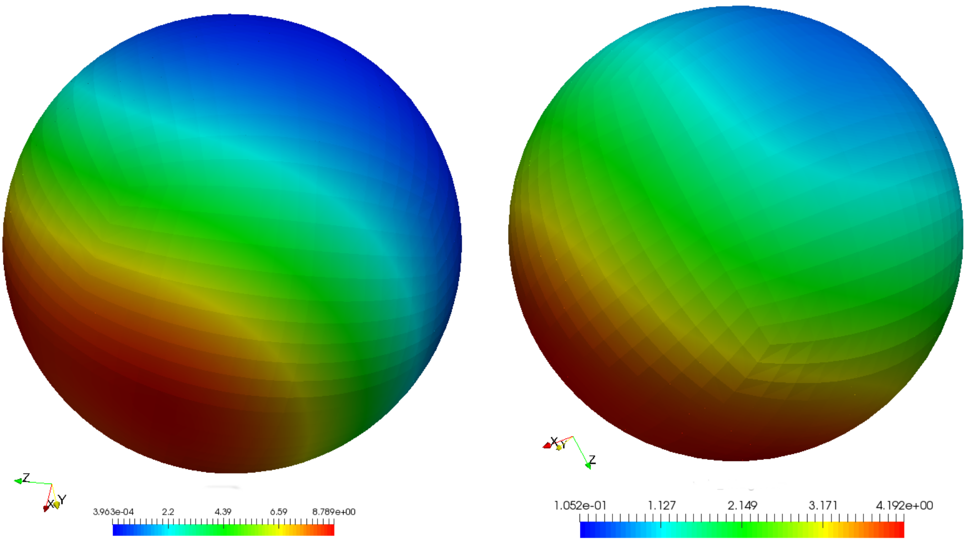

(a) Pressure **(b)** Velocity magnitude

Fig. 3.15: Solution of the Ethier-Steinman Navier-Stokes flow in a 3D sphere using 21^3 quadratic B-spline elements.

We discretize the problem using a uniform B-spline discretization. In Fig. 3.15 we show the solution obtained using 21^3 quadratic B-spline elements, from which we observe that the solution is free of oscillations. In Fig. 3.16 we study the mesh convergence behavior for the orders $k = 1, 2, 3$. The considered meshes consist of 5^3, 8^3, 12^3, and 18^3 elements. We observe optimal rates of converge of $k + 1$ and k for the L^2-error norm and H^1-error norm for the velocity field, respectively. Consistent with the observations of earlier simulations we observe a rate higher than k for the L^2-error norm of the pressure field, which we attribute to the use of identical spaces for the pressures and velocities.

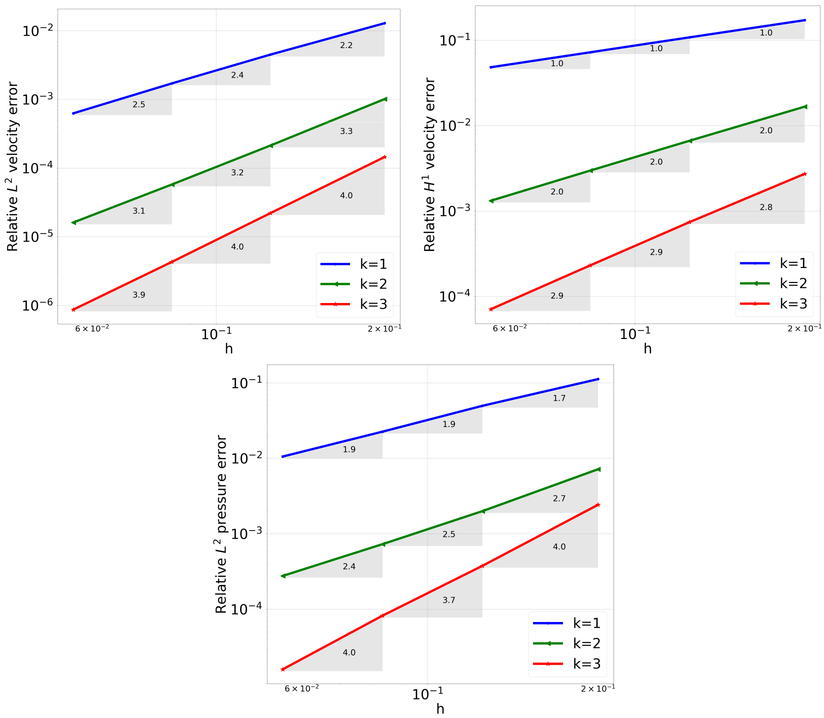

Fig. 3.16: Mesh convergence results for the Ethier-Steinman Navier-Stokes flow in a 3D sphere.

3.6 Conclusions

We proposed a stabilization technique for isogeometric analysis of the incompressible Navier-Stokes equations employing the same discretization space for the pressure and velocity fields. The pivotal idea of the developed technique is to penalize the jumps of higher-order derivatives of pressures over element interfaces. Since this technique leverages the skeleton structure of geometric models, we refer to it as a Skeleton-based IsoGeometric Analysis technique. The proposed Skeleton-stabilization penalizes the order $\alpha+1$ derivative jumps for bases with C^α regularity, and hence can be considered as a generalization of continuous interior penalty finite element methods for traditional C^0 finite elements. An important advantage of this technique in comparison to inf-sup stable approaches is that it allows the usage of the same discretization space for all field variables. In the context of isogeometric analysis this improves the integration between CAD and analysis, since the technique enables direct usage of the CAD basis for the discretization of all fields.

The proposed Skeleton-Penalty stabilization operator is consistent for solutions with smooth pressure fields. The operator is symmetric and acts only on the pressure space. As a result it does not introduce artificial coupling between the pressure space and the velocity space, and it does not destroy symmetry in the case of the Stokes system. Moreover, no modification of the right-hand-side vector is required, in contrast to some of the alternative stabilization techniques. Considering the bandwidth of the Skeleton-Penalty matrix, there is a substantial advantage to the use of splines, as they ameliorate the large bandwidth that emerges for skeleton-based stabilization operators in Lagrange-based continuous interior penalty methods.

We have observed the proposed Skeleton-Penalty method to yield solutions that are free of pressure oscillations and velocity locking for a wide range of test cases. Optimal convergence rates have been observed for all considered spline orders and regularities, including the case of multi-patch splines. Although a detailed study of the selection of the penalization parameter is beyond the scope of this manuscript, we have observed robustness of the method within a sufficiently large range of penalization parameters. We note that this observation does not necessarily extend to extreme cases, such as flows with very high Reynolds number.

In this manuscript we have restricted ourselves to the case of moderate Reynolds numbers. Extension to high Reynolds numbers needs a further investigation, as it is anticipated that additional stabilization of the velocity space is then required. We note that in the case of discontinuous spaces – which we have omitted in this work – the proposed stabilization technique fits into the discontinuous Galerkin methodology. We have relied on standard finite element data structures, and we have not considered optimizations that are possible within the isogeometric analysis framework.

Chapter 4

Skeleton-stabilized ImmersoGeometric Analysis for incompressible viscous flow problems

Abstract

A Skeleton-stabilized ImmersoGeometric Analysis technique is proposed for incompressible viscous flow problems with moderate Reynolds number. The proposed formulation fits within the framework of the finite cell method, where essential boundary conditions are imposed weakly using a Nitsche-type method. The key idea of the proposed formulation – which was considered in the conforming isogeometric analysis setting by Hoang *et.al.* [188] – is to stabilize the jumps of high-order derivatives of variables over the skeleton of the background mesh. The formulation allows the use of identical finite-dimensional spaces for the approximation of the pressure and velocity fields in immersed domains. The stability issues observed for inf-sup stable discretizations of immersed incompressible flow problems [179] are avoided with this formulation. For B-spline basis functions of degree k with highest regularity, only the derivative of order k has to be controlled, which requires specification of only a single stabilization parameter. The Stokes and Navier-Stokes equations are studied numerically in two and three dimensions using various immersed test cases. Oscillation-free solutions and optimal convergence rates can be obtained.

Reproduced from: T. Hoang, C.V. Verhoosel, C. Qin, F. Auricchio, A. Reali, E.H. van Brummelen, *Skeleton-stabilized ImmersoGeometric Analysis for incompressible viscous flow problems*, in preparation

4.1 Introduction

Finite Element Analysis (FEA) of incompressible flow problems has been an active topic of research over the last decades, with research interests ranging from theoretical aspects to engineering applications. In recent years, IsoGeometric Analysis (IGA) – a spline-based finite element simulation paradigm proposed by Hughes *et al.* [44] with the aim of establishing a better integration between Computer-Aided Design (CAD) and FEA – has been studied in the context of incompressible flow problems. Isogeometric analysis of mixed formulations for incompressible flow problems based on *inf-sup* stable velocity-pressure pairs has been studied in detail in the literature, which has led to the development of a range of isogeometric element families, namely: Taylor-Hood elements [94, 118, 119], Sub-grid elements [119, 120], H(div)-conforming elements [118, 121–123], and Nédélec elements [118]. These element families have been demonstrated to be suitable for the discretization of incompressible flow problems, by virtue of the fact that they leverage the advantageous mathematical properties of the spline basis functions used in isogeometric analysis [114].

The Finite Cell Method (FCM) – an immersed finite element method introduced by Rank *et al.* [137] – has been found to be a natural companion to isogeometric analysis. The key idea of the FCM is to embed a geometrically complex physical domain of interest into a geometrically simple embedding domain, on which a regular mesh can be built easily. The framework in which IGA and FCM are integrated – first considered by Schillinger, Rank *et al.* [138–140] – is also referred to as immersogeometric analysis [144, 145]. On the one hand immersogeometric analysis facilitates consideration of CAD trimming curves in the context of isogeometric analysis. On the other hand, it enables the construction of high-regularity spline spaces over geometrically and topologically complex volumetric domains, for which analysis-suitable spline parametrizations are generally not available. The isogeometric finite cell method has been applied to various problems in solid and structural mechanics (see [141, 189] for comprehensive reviews), in image-based analysis [142, 143], in fluid-structure interaction problems [144, 145], and in various other application areas.

In Hoang *et.al* [179] we have found that when the inf-sup stable isogeometric element families for incompressible flow problems are applied in the finite cell setting, local pressure oscillations generally occur in the vicinity of cut boundaries. An illustration of this oscillatory behavior is shown in Fig. 4.1a.

When employing the Galerkin-Least square (GLS) method, we observe similar behavior, as shown in Fig. 4.1b. The occurrence of such oscillations on cut elements with relatively large volume fractions implies that this problem is related to the inf-sup stability of the discrete problem, rather than to conditioning issues related to cut elements with small volume fractions. It is important to note that although the inf-sup stable discretization pairs (and GLS) lead to close-to-optimal converge behavior of global error measures, the oscillations in the pressure field near the immersed boundaries persist under mesh refinement. As a consequence, the approximation of quantities of interest related to the immersed boundaries is below standard, which makes the inf-sup stable (and GLS) isogeometric approach less attractive for a large class of immersed incompressible flow problems.

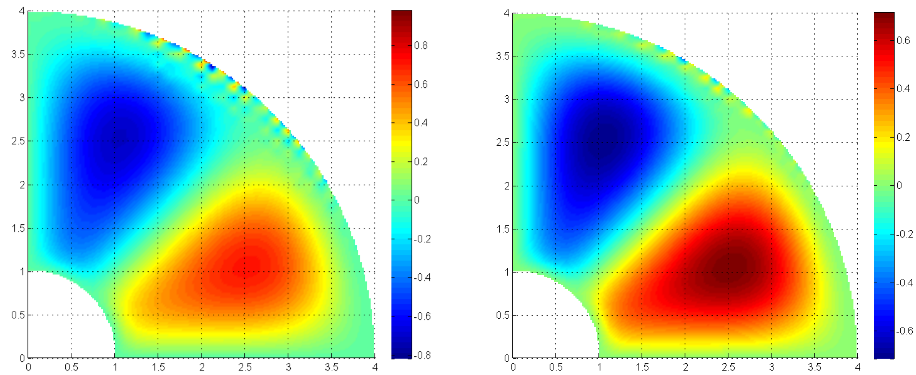

(a) **(b)**

Fig. 4.1: Unphysical pressure oscillations are observed when the Stokes problem is solved in the standard finite cell setting using *(a)* inf-sup stable isogeometric elements, shown here for Taylor-Hood (see Ref. [179] for details), and *(b)* using a Galerkin Least-squares method.

In this manuscript we propose an alternative formulation – based on the skeleton-based stabilization technique developed by Hoang *et.al* [188] in the context of conforming isogeometric analysis – to resolve the stability problems associated with immersed inf-sup isogeometric discretization pairs. In this formulation – which can be regarded as a high-regularity generalization of the continuous interior penalty method by Burman and Hansbo [40] – we rely on stabilization of the mixed form problem by amending the formulation with a skeleton-based penalty term. This alternative form of stabilization relaxes the compatibility constraints on the function spaces to be used, which allows us to consider identical discretization spaces for both the velocity and the pressure fields. Our work is related to developments that have been made in the context of XFEM and CutFEM [149–153], and is particularly inspired by the Ghost penalty stabilization technique of Burman and Hansbo [146, 190]. A novelty of our work is that we fully exploit the maximum regularity of the B-spline basis functions used in IGA, as a consequence of which the introduced stabilization operator only acts on the interface jumps of the highest order derivative of the basis functions. As a result we only require a single stabilization term to control both the inf-sup stability of the mixed problem and its related pressure-space conditioning issues. We herein propose to supplement the skeleton-based stabilized formulation in [188] with a ghost-penalty term for the velocity space, which is not required from the inf-sup stability point of view, but which is essential to control the conditioning of the discretized problem.

This paper is outlined as follows. In Section 4.2 we commence with the introduction of the unsteady incompressible Navier-Stokes equations and the essentials of the finite cell method. In Section 4.3 we then present the skeleton-stabilized formulation developed and studied in this work. In Section 4.4 we discuss the algebraic form of of the developed stabilized formulation, and its effect on the sparsity structure of the system to be solved. The proposed formulation is studied by a series of numerical test cases in Section 4.5, including the case of a three-dimensional image-based analysis of a microstructural porous medium flow. Conclusions are finally presented in Section 4.6.

4.2 Preliminaries

Before we introduce the skeleton-based stabilized formulation in Section 4.3, we here first introduce the problem setting for the unsteady Navier-Stokes equations, and the fundamental concepts of the isogeometric finite cell method.

4.2.1 The unsteady incompressible Navier-Stokes equations

We consider the unsteady incompressible Navier-Stokes equations on the open bounded domain $\Omega \in \mathbb{R}^d$, where $d = 2, 3$ denotes the spatial dimension of the domain. The Lipschitz boundary $\partial\Omega$ is split in the Dirichlet boundary, Γ_D, and the Neumann boundary, Γ_N, such that $\overline{\Gamma_D} \cup \overline{\Gamma_N} = \partial\Omega$ and $\Gamma_D \cap \Gamma_N = \emptyset$. The unit normal vector to $\partial\Omega$, which points out of the domain, is denoted by $\mathbf{n}$. For any time instant $t \in [0, T)$ the Navier-Stokes equations for the velocity field $\mathbf{u} : \Omega \times [0, T) \to \mathbb{R}^d$ and pressure field $p : \Omega \times [0, T) \to \mathbb{R}$ read:

$$\begin{cases} \text{Find } \mathbf{u} : \Omega \times [0,T) \to \mathbb{R}^d, \text{ and } p : \Omega \times [0,T) \to \mathbb{R} \text{ such that:} \\ \partial_t \mathbf{u} + \nabla \cdot (\mathbf{u} \otimes \mathbf{u}) - \nabla \cdot (2\mu \nabla^s \mathbf{u}) + \nabla p = \mathbf{f} \quad \text{in } \Omega \times (0,T), \\ \qquad \nabla \cdot \mathbf{u} = 0 \quad \text{in } \Omega \times (0,T), \\ \qquad \mathbf{u} = \mathbf{g} \quad \text{on } \Gamma_D \times (0,T), \\ \qquad 2\mu \nabla^s \mathbf{u} \cdot \mathbf{n} - p\mathbf{n} = \mathbf{h} \quad \text{on } \Gamma_N \times (0,T), \\ \qquad \mathbf{u} = \mathbf{u}_0 \quad \text{in } \Omega \times \{0\}. \end{cases} \tag{4.1}$$

In this problem formulation the symmetric gradient of the velocity field is denoted by $\nabla^s \mathbf{u} := \frac{1}{2}\left(\nabla \mathbf{u} + (\nabla \mathbf{u})^T\right)$ and μ represents the kinematic viscosity. The exogenous data $\mathbf{f} : \Omega \times (0, \infty) \to \mathbb{R}^d$, $\mathbf{g} : \Gamma_D \times (0, \infty) \to \mathbb{R}^d$, and $\mathbf{h} : \Gamma_N \times (0, \infty) \to \mathbb{R}^d$ represent body forces, prescribed velocity, and traction data, respectively. The initial data in the strong form (4.1) are denoted by $\mathbf{u}_0 : \Omega \to \mathbb{R}^d$.

To provide a framework for the derivation of the immersed formulation introduced in the next section, we here first present the weak formulation in the conforming setting. For any vector space $\mathcal{V}$, we denote by $\mathcal{L}(0, T; \mathcal{V})$ a suitable linear space of $\mathcal{V}$-valued functions on the time interval $(0, T)$. The weak formulation of the initial boundary value problem (4.1) then follows as:

$$\begin{cases} \text{Find } \mathbf{u} \in \mathcal{L}(0,T;\boldsymbol{\mathcal{V}}_{\mathbf{g},\Gamma_D}) \text{ and } p \in \mathcal{L}(0,T;\mathcal{Q}), \text{ subject to } \mathbf{u}(0) = \mathbf{u}_0, \\ \text{such that for almost all } t \in (0,T): \\ (\partial_t \mathbf{u}, \mathbf{w}) + c(\mathbf{u}; \mathbf{u}, \mathbf{w}) + a(\mathbf{u}, \mathbf{w}) + b(p, \mathbf{w}) = \ell_1(\mathbf{w}) \ \forall \mathbf{w} \in \boldsymbol{\mathcal{V}}_{\mathbf{0},\Gamma_D}, \\ \qquad b(q, \mathbf{u}) = 0 \qquad \forall q \in \mathcal{Q}. \end{cases} \tag{4.2}$$

The linear operators in this formulation are defined as

$$c(\mathbf{v}; \mathbf{u}, \mathbf{w}) := (\mathbf{v} \cdot \nabla \mathbf{u}, \mathbf{w}), \tag{4.3a}$$

$$a(\mathbf{u}, \mathbf{w}) := 2\mu\,(\nabla^s \mathbf{u}, \nabla^s \mathbf{w}), \tag{4.3b}$$

$$b(q, \mathbf{w}) := -\,(q, \mathrm{div}\mathbf{w}), \tag{4.3c}$$

$$\ell_1(\mathbf{w}) := (\mathbf{f}, \mathbf{w}) + \langle \mathbf{h}, \mathbf{w} \rangle_{\Gamma_N}, \tag{4.3d}$$

where $(\cdot, \cdot)$ denotes the inner product in $L^2(\Omega)$ and $\langle \cdot, \cdot \rangle_{\Gamma_N}$ denotes the inner product in $L^2(\Gamma_N)$. The function spaces in (4.2) are defined as

$$\mathcal{V}_{\mathbf{g},\Gamma_D} := \left\{\mathbf{u} \in [H^1(\Omega)]^d : \mathbf{u} = \mathbf{g} \text{ on } \Gamma_D\right\}, \qquad \mathcal{Q} := L^2(\Omega), \tag{4.4}$$

and the velocity test space, $\mathcal{V}_{\mathbf{0},\Gamma_D}$, is taken as the homogeneous version of $\mathcal{V}_{\mathbf{g},\Gamma_D}$. In the case of pure Dirichlet boundary conditions the pressure is determined up to a constant, which then requires supplementation of the additional pressure condition:

$$\mathcal{Q} := L^2_0(\Omega) \equiv \left\{q \in L^2(\Omega) : \int_\Omega q \, \mathrm{d}\Omega = 0\right\}. \tag{4.5}$$

4.2.2 The finite cell method

In the finite cell method, the physical domain of interest, Ω, is immersed into a geometrically simple ambient domain, $\mathcal{A} \supset \Omega$, as illustrated in Fig. 4.2a. In this manuscript we consider the ambient domain to be rectangular, so that it can be partitioned by a regular grid with uniform spacing $h > 0$. We refer to this partitioning as the ambient domain mesh, $\mathcal{T}^h_{\mathcal{A}}$. Elements in this ambient domain mesh that do not intersect the physical domain are discarded in the finite cell analysis, which leads to the definition of the finite cell background mesh:

$$\mathcal{T}^h := \{K \in \mathcal{T}^h_{\mathcal{A}} : K \cap \Omega \neq \emptyset\} \tag{4.6}$$

The ambient domain mesh and background mesh are illustrated in Fig. 4.2.

The conceptual idea of the finite cell method is to construct a suitable discretization space on the background mesh, and to use that basis in a Galerkin formulation pertaining to the physical domain. Dirichlet boundary conditions on non-conforming edges are typically enforced weakly, most commonly by means of Nitsche's method [163]. We will introduce the Nitsche formulation for the problem (4.1) in Section 4.3. In the remainder of this section we introduce the B-spline basis defined over the background mesh, and the integration procedure employed to evaluate volume and (immersed) surface integrals over elements that are cut by the immersed boundary.

4.2.2.1 B-spline basis

By virtue of the fact that in the finite cell method basis functions are constructed on a regular background mesh, it enables the isogeometric analysis

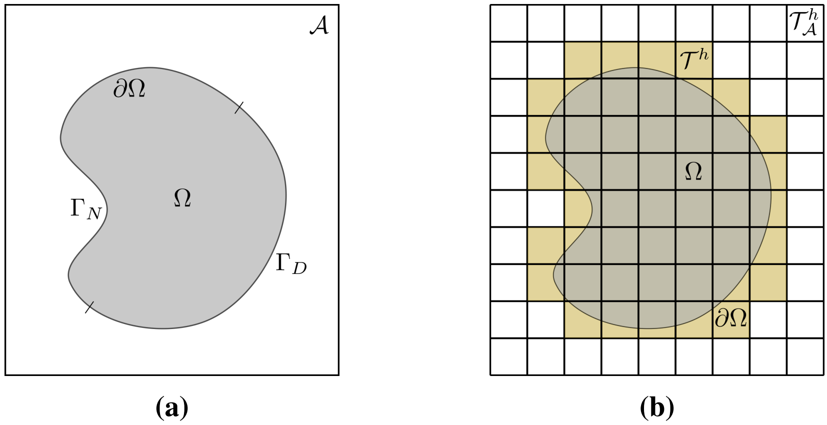

Fig. 4.2: Schematic representation of *(a)* the physical domain Ω and ambient domain $\mathcal{A}$ as considered in the finite cell method, and *(b)* the ambient domain mesh, $\mathcal{T}^h_{\mathcal{A}}$ (covering the complete ambient domain), and background mesh, $\mathcal{T}^h$ (marked by the yellow background shading).

of complex-shaped physical domains. In this manuscript we restrict ourselves to a single patch open B-spline basis over the ambient domain mesh, defined by non-decreasing knot vectors in all spatial directions $\delta = 1, \ldots, d$,

$$\Xi^\delta = [\underbrace{\xi_1^\delta, \ldots, \xi_1^\delta}_{(k+1)-\text{time}}, \xi_2^\delta, \ldots, \xi_{m^\delta-1}^\delta, \underbrace{\xi_{m^\delta}^\delta, \ldots, \xi_{m^\delta}^\delta}_{(k+1)-\text{time}}], \tag{4.7}$$

In accordance with the definition of open B-splines the first and last knot values are repeated $k+1$ times, where k denotes the global isotropic polynomial degree of the basis. We align the knot vectors with the ambient domain, which essentially implies that the we have an identity geometric map between the parameter domain and the ambient domain. The spacing between two consecutive knots is therefore equal to the global isotropic mesh parameter h.

Using the knot vectors (4.7) a B-spline basis of degree k can be constructed over the ambient domain by means of the recursive Cox-De Boor formula [47]. We denote this B-spline basis by $\mathcal{N}^k_{\mathcal{A}} = \{N^k_{\mathcal{A},I} : \mathcal{A} \to \mathbb{R}\}_{I=1}^{n_{\mathcal{A}}}$, where the total number of basis functions is equal to $n_{\mathcal{A}} = \otimes_{\delta=1}^d \{m^\delta + k - 1\}$, with m^δ the number of unique knot values per direction. In the finite cell analysis we discard the basis function that are not supported on the background mesh $\mathcal{T}^h$, so that the B-spline basis follows as:

$$\mathcal{N}^k := \{N \in \mathcal{N}^k_{\mathcal{A}} : \text{supp}(N) \cap \mathcal{T}^h \neq \emptyset\} \tag{4.8}$$

Note that, by definition, all basis functions in $\mathcal{N}^k$ have positive support over the physical domain Ω. The cardinality of $\mathcal{N}^k$ is denoted by $n \leq n_{\mathcal{A}}$. We herein consider maximum regularity B-spline bases – as indicated by the non-repeated internal knot values in (4.7) – so that the basis functions are C^{k-1} continuous. The B-spline function space $\mathcal{S}^k$ spanned by the basis $\mathcal{N}^k$ is therefore a finite dimensional subspace of the Sobolev space $H^k(\Omega^h)$, where $\Omega^h = int(\bigcup_{K \in \mathcal{T}^h} \overline{K})$.

4.2.2.2 Cut cell integration

For elements in the background mesh that are intersected by the boundaries of the physical domain, standard quadrature rules are inaccurate, since effectively discontinuous functions are integrated over such cut cells. The FCM therefore generally employs an advance numerical-integration technique for cut cells. Herein we use the bisectioning-based segmentation scheme proposed in [143] in the context of the isogeometric finite cell analysis of image-based geometric models, which also enables us to extract a parametrization and quadrature rules for the immersed boundaries.

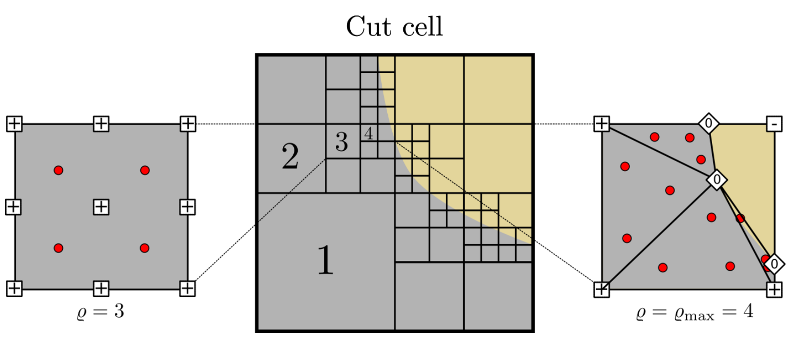

Fig. 4.3: Illustration of the bisection-based tessellation scheme used to generate quadrature rules for the cells that are cut by the immersed boundary. The vertex markers indicate whether the employed interpolant of the level set function is zero (on the boundary), positive (inside the domain), or negative (outside the domain). The red points in the sub-cell zooms are an illustration of the distribution of the integration points in such cells.

We illustrate the bisection-based tessellation scheme in Fig. 4.3 for completeness. The element-by-element routine commences with the evaluation of a level set function in the vertices associated with a $\varrho_{\max}$-times uniform refinement of the element. This level set can either be derived from voxel data in a scan-based analysis, or a signed-distance function can be considered in the case that the geometry is provided by a CAD model. The integration points for a cut cell are assembled by traversing the levels of uniform refinement, where for each sub-cell in that level it is determined whether the interface passes through it. If all vertices of a sub-cell exceed a specified threshold value (zero in the case of a signed-distance function) the sub-cell is kept as an integration sub-cell. Otherwise a further subdivision of the sub-cell is considered, and the same check is performed on the next level. On the lowest level this recursion is closed with a tessellation procedure. From an implementation perspective the integration points and weights on all sub-cells are collected on the level of the cut-element, which essentially provides us with an integration scheme tailored to the cut element.

The tessellation procedure used on the deepest level of integration refinement provides us with the possibility to extract a parametrization of the boundary. In essence, the immersed boundary is reconstructed on an element-by-element basis by identifying the faces of the integration sub-cells that coincide with the immersed boundary. The collection of sub-cell faces that approximates the immersed boundary provides a piece-wise linear parametrization of this boundary. Using this piece-wise parametrization, quadrature rules can be constructed. Evidently, the refinement parameter $\varrho_{\max}$ controls the accuracy with which the geometry is approximated.

4.3 Skeleton-stabilized immersogeometric analysis for the Navier-Stokes equations

In this section we introduce the skeleton-stabilized immersed isogeometric analysis formulation for the Navier-Stokes equations. We commence with the definition of the topological structures on which this stabilization technique is based, after which we present the two stabilization aspects in our formulation, *viz.* the Ghost penalty stabilization of the velocity components at the cut boundaries, and the pressure stabilization on the skeleton of the background mesh.

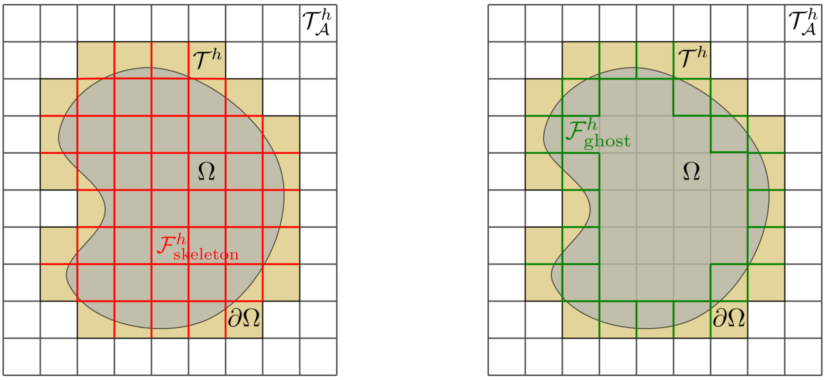

Fig. 4.4: Schemtatic representation of *(a)* the skeleton structure, and *(b)* the ghost interface structure.

4.3.1 The background mesh: skeleton structure and ghost structure

We consider the background mesh $\mathcal{T}^h$ as defined in Section 4.2.2. The stabilized formulation presented herein is based on the skeleton of this background mesh, which is defined as

$$\mathcal{F}^h_{\text{skeleton}} = \{\partial K \cap \partial K' \mid K, K' \in \mathcal{T}^h, K \neq K'\}. \tag{4.9}$$

This skeleton, for which the mesh parameter h is associated with that of the background mesh, is illustrated in Fig. 4.4a. Note that the boundary faces of the mesh $\mathcal{T}^h$ are not a part of this skeleton mesh.

Besides the skeleton structure (4.9) we also consider that part of the skeleton which coincides with the faces of all cut cells in the domain, to which we refer as the ghost skeleton:

$$\mathcal{F}^h_{\text{ghost}} = \mathcal{F}^h_{\text{skeleton}} \cap \left\{F \mid F \subset \partial K : K \in \mathcal{T}^h, K \cap \partial\Omega \neq \emptyset\right\} \tag{4.10}$$

This ghost skeleton structure is illustrated in Fig. 4.4b, where the mesh parameter h is still associated with that of the background mesh. Note that this structure does also contain some faces that do not intersect the boundary of the physical domain.

Since we herein consider single patch discretizations of the ambient domain with maximal regularity the basis functions are C^{k-1} continuous over all faces in the skeleton mesh $\mathcal{F}_{\text{skeleton}}$. Therefore, the jumps in the normal derivative up to order $k-1$ of all functions in $\mathcal{S}^k = \text{span}(\mathcal{N}^k)$ vanish:

$$[\![\partial_n^i f]\!]_F = 0, \quad 0 \leq i \leq k-1, \qquad \forall f \in \mathcal{S}^k, \tag{4.11}$$

where the jump operator $[\![\cdot]\!]$ associates to any function f in the broken Sobolev space $\{f \in L^2(\Omega) : f|_K \in H^1(K),\ \forall K \in \mathcal{T}^h\}$ the $L^2(\mathcal{F}^h_{\text{skeleton}})$-valued function:

$$[\![f]\!] = f^+ - f^-$$

The superscripts $(\cdot)^{\pm}$ refer to the traces of f on the two opposite sides of each face $F \in \mathcal{F}^h_{\text{skeleton}}$, with an arbitrary allocation of $+$ and $-$.

4.3.2 The Skeleton-stabilized finite cell formulation

In this contribution we study the discretization of problem (4.1) using identical highest smoothness spline discretizations for the velocity and pressure fields:

$$\mathcal{V}^h := \left[\mathcal{S}^k\right]^d, \qquad \mathcal{Q}^h := \mathcal{S}^k. \tag{4.12}$$

The Skeleton-stabilized finite cell formulation for the system (4.1) reads:

$$\begin{cases} \text{Find } \mathbf{u}^h \in \mathcal{L}(0,T;\mathcal{V}^h) \text{ and } p^h \in \mathcal{L}(0,T;\mathcal{Q}^h), \text{ subject to } \mathbf{u}^h(0) = \mathbf{u}_0^h, \\ \text{such that for almost all } t \in (0,T), \text{ for all } (\mathbf{w}^h, q) \in \mathcal{V}^h \times \mathcal{Q}^h: \\ (\partial_t \mathbf{u}^h, \mathbf{w}^h) + c(\mathbf{u}^h; \mathbf{u}^h, \mathbf{w}^h) + a^h(\mathbf{u}^h, \mathbf{w}^h) + s^h_{\text{ghost}}(\mathbf{u}^h, \mathbf{w}^h) + b^h(p^h, \mathbf{w}^h) = \ell_1^h(\mathbf{w}^h), \\ \hfill b^h(q, \mathbf{u}^{\mathbf{h}}) - s^h_{\text{skeleton}}(p^h, q^h) = \ell_2^h(q^h), \end{cases} \tag{4.13}$$

where $\mathbf{u}_0^h$ corresponds to a projection of the initial data on $[\mathcal{S}^k]^d$, and where the linear operators as introduced in the conforming setting in equation (4.3) are supplemented with additional terms for Nitsche's imposition of the boundary conditions [163]:

$$a^h(\mathbf{u}^h, \mathbf{w}^h) := a(\mathbf{u}^h, \mathbf{w}^h) - 2\mu \left[\langle \nabla^s \mathbf{u}^h \cdot \mathbf{n}, \mathbf{w}^h \rangle_{\Gamma_D} + \langle \nabla^s \mathbf{w}^h \cdot \mathbf{n}, \mathbf{u}^h \rangle_{\Gamma_D} \right] + \mu \langle \beta h^{-1} \mathbf{u}^h, \mathbf{w}^h \rangle_{\Gamma_D}, \tag{4.14a}$$

$$b^h(q^h, \mathbf{w}^h) := b(q^h, \mathbf{w}^h) + \langle q^h, \mathbf{w}^h \cdot \mathbf{n} \rangle_{\Gamma_D}, \tag{4.14b}$$

$$\ell_1^h(\mathbf{w}^h) := \ell_1(\mathbf{w}^h) - 2\mu \langle \nabla^s \mathbf{w}^h \cdot \mathbf{n}, \mathbf{g} \rangle_{\Gamma_D} + \mu \langle \beta h^{-1} \mathbf{g}, \mathbf{w}^h \rangle_{\Gamma_D}, \tag{4.14c}$$

$$\ell_2^h(q^h) := \langle q^h \mathbf{n} \cdot \mathbf{g} \rangle_{\Gamma_D}, \tag{4.14d}$$

where $\langle\cdot,\cdot\rangle_{\Gamma_D}$ denotes the inner product in $L^2(\Gamma_D)$. The two stabilization operators that are appended to the weak form (4.13) are defined as:

$$s^h_{\text{ghost}}(\mathbf{u}^h,\mathbf{w}^h) := \sum_{F\in\mathcal{F}_{\text{ghost}}} \int_F \widetilde{\gamma}\mu h^{2k-1} [\![\partial_n^k \mathbf{u}_h]\!] \cdot [\![\partial_n^k \mathbf{v}_h]\!] \,\mathrm{ds}, \tag{4.15a}$$

$$s^h_{\text{skeleton}}(p^h,q^h) := \sum_{F\in\mathcal{F}^h_{\text{skeleton}}} \int_F \gamma\mu^{-1} h^{2k+1} [\![\partial_n^k p^h]\!][\![\partial_n^k q^h]\!] \,\mathrm{ds}, \tag{4.15b}$$

where $\widetilde{\gamma}$ and γ denote certain suitable positive stabilization parameters; see Remark 4.2 below.

The operator $s_{\text{ghost}}(\mathbf{u}^h,\mathbf{w}^h)$ is referred to as the Ghost-penalty operator [146, 190]. This term – which penalizes the (non-vanishing) jump in the k-th order normal derivative on the ghost skeleton, enables scaling of the Nitsche penalty term by the reciprocal mesh size parameter h^{-1} of the *background mesh*, independent of the cut-element configurations. Without the ghost-penalty term, the Nitsche term would have to be based on the reciprocal of the *cut-element* size to ensure stability. However, this would result in configuration-sensitive stability and severe ill-conditioning in critical cases such as sliver cut configurations. The ghost-penalty stabilization hence effectively controls the conditioning of the velocity contributions to the formulation. The condition numbers then scale as in the case of conforming discretizations, and are independent of the configuration of the cut cells [146, 190].

The operator $s_{\text{skeleton}}(p^h,q^h)$ in (4.13) is referred to as the Skeleton-penalty operator, which was developed for conforming isogeometric discretizations of the unsteady incompressible Navier-Stokes equations in [188], and is applied here without any modification to the immersed setting. This term allows to use identical pairs of spaces for the velocity and pressure fields, as defined in equation (4.12). It should be emphasized that the skeleton structure is defined not only inside the physical domain but in the whole background mesh. In this way, the pressure-stabilization not only ensures inf-sup stability over the complete domain but also resolves the conditioning issue related to the pressure field in the case of pathological cut configurations.

Remark 4.1. We note that the stabilization parameters γ and $\widetilde{\gamma}$, and the viscosity parameter μ, in the operators (4.15a) and (4.15b) are kept inside the integrand for the sake of generality. For the simulations considered herein – where we focus on moderate Reynolds numbers flows – these scalings are defined globally. This global scaling may not extend to, *e.g.*, the more general case of convection-dominated flows.

Remark 4.2. The positive parameters γ and $\widetilde{\gamma}$ are selected in an ad hoc manner, where an important guideline is that they should decrease with increasing regularity. In the full regularity setting considered herein, this implies that they decrease with increasing order of the discretization. Since we are using identical highest-regularity B-spline spaces for velocity and pressure fields, we have found that for our test cases acceptable results are generally obtained by assigning the same value to both parameters, *i.e.* $\gamma = \widetilde{\gamma}$.

Remark 4.3. The pressure skeleton-stabilization term and the ghost penalty stabilization term scale differently with the mesh size, *viz.* with h^{2k+1} and h^{2k-1}, respectively. This difference stems from the fact that the velocity field resides in H^1, while the pressure resides in L^2. Note that although we have restricted ourselves herein to regular meshes with global and isotropic size h, there is no fundamental restriction to the application of the formulation (4.13) in the context of non-uniformly spaced grids.

The rationale behind the skeleton-stabilized formulation – which for sufficiently smooth velocity and pressure solutions ($\mathbf{u} \in [H^k(\Omega)]^d$ and $p \in H^k(\Omega)$) is consistent with (4.1) – is that it effectively targets the shortcomings observed using inf-sup stable spaces. The skeleton stabilization operator (4.15b) is tied to the background domain, in the sense that it is completely independent of the shape and volume fraction of the cut cells it pertains to. As a consequence, the stabilizing effect of the operator does not decrease with decreasing volume fractions. This contrasts the situation in which inf-sup stable pairs are considered, since in that setting the cut cell characteristics have been observed to impact the inf-sup stability [179]. Moreover, the stabilization operator (4.15b) can be conceived of as a weakly imposed constraint on the highest-order non-vanishing derivative of the pressure field, which essentially means that it controls the smoothness of the extension of the interior domain into the exterior domain. In [188] we have demonstrated that the operator (4.15b) is related to the least squares minimization problem for the highest-order derivative jumps. Thereby the operator effectively suppresses oscillations in the pressure field near the immersed boundaries.

4.4 The algebraic form

Using the B-spline basis functions as defined in Section 4.2.2, the velocity and pressure field can be expressed as

$$\mathbf{u}^h(\mathbf{x},t) = \sum_{i=1}^{n_u} \mathbf{N}_i(\mathbf{x})\hat{u}_i(t), \qquad p^h(\mathbf{x},t) = \sum_{i=1}^{n_p} N_i(\mathbf{x})\hat{p}_i(t). \tag{4.16}$$

Note that the basis functions for the velocity field are printed in bold font to indicate that these are vector-valued. The coefficients corresponding to these basis functions are assembled in the vector $\hat{\mathbf{u}}(t) = (\hat{u}_1, \hat{u}_2, \ldots, \hat{u}_{n_u})^T$. The basis functions for the pressure are evidently scalar-valued, with associated coefficient vector $\hat{\mathbf{p}}(t) = (\hat{p}_1, \hat{p}_2, \ldots, \hat{p}_{n_p})^T$. In the absence of constraints, the number of velocity-degrees of freedom, n_u, is d times that of pressure degrees of freedom, n_p.

Consistent with (4.16) the discrete approximation spaces can be defined as $\mathcal{V}^h = \operatorname{span}\{\mathbf{N}_i\}_{i=1}^{n_u}$ and $\mathcal{Q}^h = \operatorname{span}\{N_i\}_{i=1}^{n_p}$, so that the formulation (4.13) can be cast into a time-dependent algebraic system of equations of size $n = n_u + n_p$:

$$\begin{cases} \text{For each } t \in (0,T), \text{ find } \hat{\mathbf{u}} = \hat{\mathbf{u}}(t) \in \mathbb{R}^{n_u} \text{ and } \hat{\mathbf{p}} = \hat{\mathbf{p}}(t) \in \mathbb{R}^{n_p}, \\ \text{given } \hat{\mathbf{u}}(0) = \hat{\mathbf{u}}_0, \text{ such that:} \\ \mathbf{M}\partial_t\hat{\mathbf{u}} + \left[\mathbf{C}(\hat{\mathbf{u}}) + \mathbf{A} + \mathbf{S}_{\text{ghost}}\right]\hat{\mathbf{u}} + \mathbf{B}^T\hat{\mathbf{p}} = \mathbf{f}_1, \\ \qquad\qquad\qquad\qquad\qquad \mathbf{B}\hat{\mathbf{u}} - \mathbf{S}_{\text{skeleton}}\hat{\mathbf{p}} = \mathbf{f}_2. \end{cases} \tag{4.17}$$

We employ Crank-Nicolson time integration with Picard iterations to solve this nonlinear algebraic problem in time. See Ref. [188] for details regarding the solution algorithm.

The matrices and vectors in (4.17) pertaining to the standard volume and boundary surface terms can be expressed in terms of the operators (4.14) as:

$$C(\hat{\mathbf{u}})_{ij} := c(\hat{\mathbf{u}}; \mathbf{N}_j, \mathbf{N}_i), \tag{4.18a}$$

$$A_{ij} := a^h(\mathbf{N}_j, \mathbf{N}_i), \tag{4.18b}$$

$$B_{ij} := b(N_i, \mathbf{N}_j), \tag{4.18c}$$

$$f_{1,i} := \ell_1^h(\mathbf{N}_i) \tag{4.18d}$$

$$f_{2,i} := \ell_2(N_i). \tag{4.18e}$$

The stabilization matrices in (4.17) pertain to the skeleton and ghost structure of the background mesh, $\mathcal{F}^h_{\text{skeleton}}$ and $\mathcal{F}^h_{\text{ghost}}$, respectively, and hence require data structures to evaluate the jump of high-order derivatives of the basis functions across the background mesh element interfaces through the operators in (4.15) as:

$$
\begin{aligned}
S_{\text{skeleton},ij} &= s^h_{\text{skeleton}}(N_j, N_i), && (4.19a)\\
S_{\text{ghost},ij} &= s^h_{\text{ghost}}(\mathbf{N}_j, \mathbf{N}_i). && (4.19b)
\end{aligned}
$$

Due to the fact that the jump operators on the highest-order derivatives of the B-spline basis functions provide additional connectivity between basis functions, the stabilization matrices (4.19) have an effect on the sparsity pattern of the algebraic problem. In Fig. 4.5 we present a comparison of the sparsity patterns of the system matrices for the cases of a second-order ($k = 2$) B-spline basis as considered herein and a second-order ($k = 2$) Lagrange basis (closely resembling the continuous interior penalty method). Note that since both bases are constructed over the same background mesh, the number of Lagrange basis functions is significantly larger (approximately k-times) than the number of B-spline basis functions, by virtue of the fact that, as opposed to Lagrange basis functions, for full-regularity B-splines the number of basis functions does not scale proportionally with the degree of the basis to the power d.

Inspection of the velocity-velocity and pressure-pressure blocks reveals that the footprint of the stabilization operators have a different effect for the two bases, in the sense that for the $k = 2$ case $2k = 4$ off-diagonal bands are observed for the Lagrange basis, and $k + 1 = 3$ for the B-spline basis. This difference – which becomes more pronounced when the degree k increases – was also observed in the mesh conforming case in Ref. [188], with the difference that in the immersed setting both the velocity and pressure space are stabilized, thereby making the impact of the stabilization operators on the computational effort larger in the immersed setting. Following the arguments in Ref. [188], the difference in number of off-diagonal bands can be explained by comparison of the one-dimensional B-spline and Lagrange bases, as shown for the cubic ($k = 3$) case in Fig. 4.6. This Figure corroborates that in the case of full-regularity B-splines all derivative jumps up to order $k - 1$ vanish across element interfaces, as a result of which only the k-th derivative jump operator impacts the sparsity pattern. The number of off-diagonal bands for the stabilization operators is therefore in this case equal to $k + 1$. In contrast, for Lagrange bases, the lower-order derivative jumps are non-vanishing, as a result of which $2k$ off-diagonal bands appear.

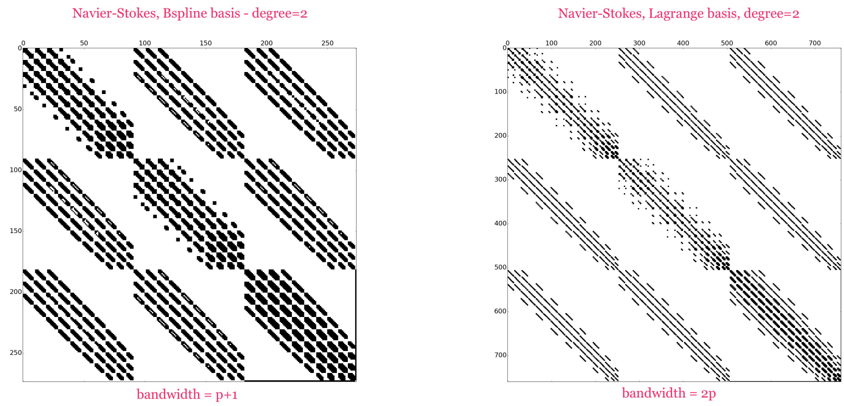

(a) B-spline basis **(b)** Lagrange basis

Fig. 4.5: Illustration of the sparsity patterns of the system matrix corresponding to (4.17) for *(a)* a second-order B-spline basis, and *(b)* a second-order Lagrange basis. The stencil of the B-spline case is smaller than that of the Lagrange case. See Fig. 4.6 for more elaborations. Note that here both bases are constructed over the same background mesh and therefore result in different numbers of degrees of freedom; the figure sizes are thus not of the same scale.

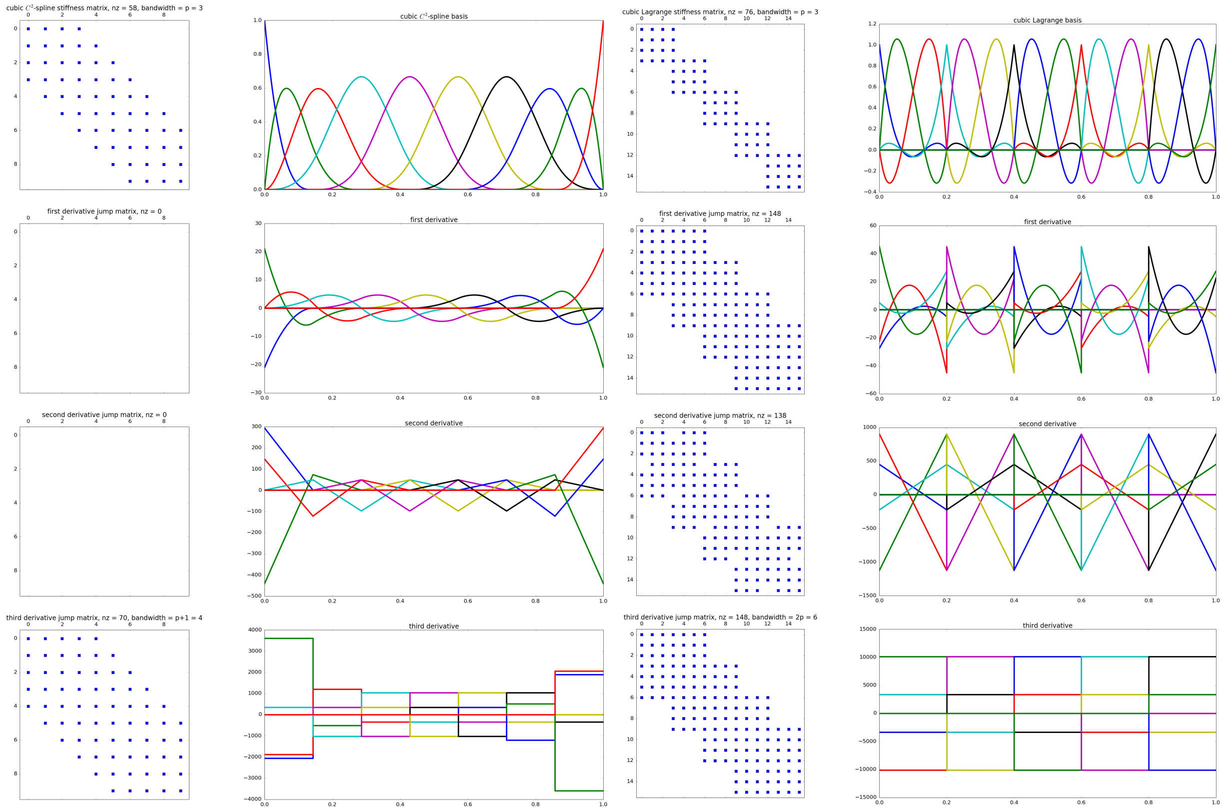

(a) B-spline case **(b)** Lagrange case

Fig. 4.6: Comparison of the *(a)* univariate cubic B-spline basis of full regularity, and *(b)* univariate cubic Lagrange basis. Due to the C^{k-1} continuity of the B-spline basis only the k-th derivative jump is non-vanishing, this in contrast to the case of the C^0 continuous Lagrange basis. Moreover, the bandwidth in the B-spline case is $k+1$, much smaller than in the Lagrange case which is $2k$.

4.5 Numerical experiments

In this section we investigate the numerical performance of the proposed immersed skeleton-stabilized formulation. In all cases, the system (4.13) is solved using identical highest-regularity B-spline spaces for the approximations of the velocity and pressure fields. Unless stated otherwise, the number of bi-sectioning levels that determines the accuracy of the geometry representation is taken equal to six in the two-dimensional simulations, and equal to five in the three-dimensional case. Evidently, when studying higher-order approximations, one ideally wants to resolve the geometry as closely as possible. The above-mentioned selected levels of bi-sectioning are chosen such that the simulations remain computationally tractable.

4.5.1 Steady Navier-Stokes flow in a quarter annulus domain

We consider the steady Navier-Stokes equations on an open quarter-annulus domain

$$\Omega = \left\{(x, y) \in \mathbb{R}^2_{>0} : R_1^2 < x^2 + y^2 < R_2^2\right\},$$

with inner radius $R_1 = 1$ and outer radius $R_2 = 4$; see Fig. 4.7. Dirichlet boundary conditions are prescribed on the entire boundary $\partial\Omega = \Gamma_D$. The body force $\mathbf{f}$ and Dirichlet data $\mathbf{g}$ are selected in accordance with the manufactured solution

$$\begin{aligned}
u_1 &= 10^{-6}x^2y^4(x^2+y^2-1)(x^2+y^2-16)(5x^4+18x^2y^2-85x^2+13y^4-153y^2+80),\\
u_2 &= 10^{-6}xy^5(x^2+y^2-1)(x^2+y^2-16)(102x^2+34y^2-10x^4-12x^2y^2-2y^4-32),\\
p &= 10^{-7}xy(y^2-x^2)(x^2+y^2-16)^2(x^2+y^2-1)^2\exp\left(14(x^2+y^2)^{-1/2}\right),
\end{aligned} \tag{4.20}$$

of problem (4.1) without the inertia term and with viscosity $\mu = 1$. This manufactured solution is adopted from Refs. [174, 179]. Note that u_1 and u_2 vanish on $\partial\Omega$, and hence $\mathbf{g} = \mathbf{0}$. Moreover, the manufactured pressure solution complies with the zero-average pressure condition $\int_\Omega p = 0$, which is imposed here by means of a Lagrange multiplier.

We tested this problem for the Stokes case ($\mu = 0$) in Ref. [179] with different families of inf-sup stable isogeometric spaces. A representative result for that setting is shown in Fig. 4.1a, from which unphysical pressure oscillations in the vicinity of the cut elements are clearly observed. Using inf-sup stable pairs, similar oscillations are also observed in the Navier-Stokes case.

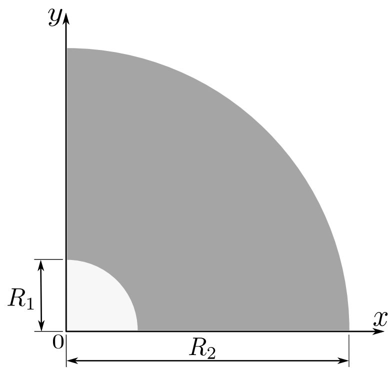

Fig. 4.7: Geometry definition of the quarter-annulus ring problem.

In contrast, the pressure field computed using the skeleton-stabilized formulation (4.13) – illustrated in Fig. 4.8 for the case of quadratic B-splines with a 21×21 elements ambient domain mesh – is free of oscillations. Note that the physical domain is completely immersed in the ambient domain, in the sense that none of the boundaries conform to the background mesh.

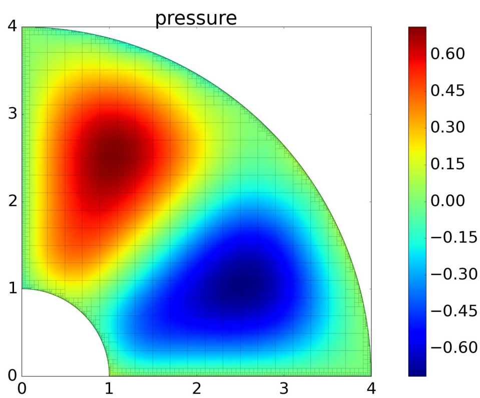

Fig. 4.8: Pressure solution of the steady Navier-Stokes equations in the quarter annulus domain with $\mu = 1$, computed using the skeleton-stabilized formulation with quadratic B-splines. The original ambient domain mesh consists of 21×21 elements.

In Fig. 4.9 we present mesh convergence results for the proposed stabilized formulation, where a sequence of uniformly refined background meshes is generated starting from the 11×11 elements coarsest ambient domain mesh. The finest level ambient domain mesh contains 176×176 elements. We consider $k = 1, 2, 3$ full-regularity B-splines with stabilization parameters

$\gamma = 10$ for $k = 1$, $\gamma = 0.1$ for $k = 2$, $\gamma = 5 \times 10^{-4}$ for $k = 3$ and $\widetilde{\gamma} = 10^{-k-1}$ for all k. We observe optimal rates of convergence of $k+1$ and k for the L^2-norm and H^1-norm of the velocity field, respectively. For the L^2-norm of the pressure we observe the optimal rate of k. It is notable that the convergence behavior of the stabilized formulation considered here is highly regular on all considered meshes, as opposed to the convergence behavior of the non-stabilized FCM formulation; cf. [179].

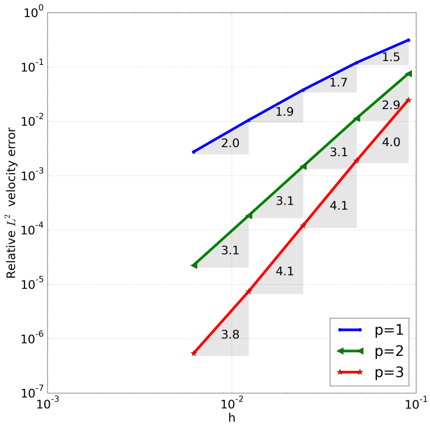

(a) L^2 velocity error

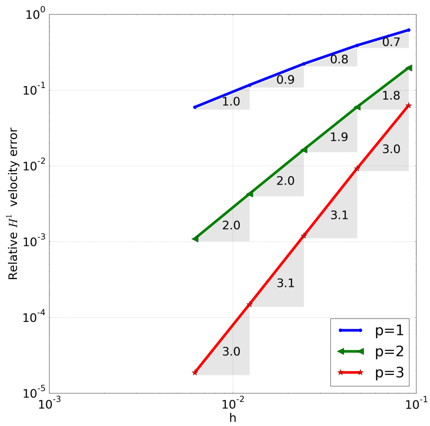

(b) H^1 velocity error

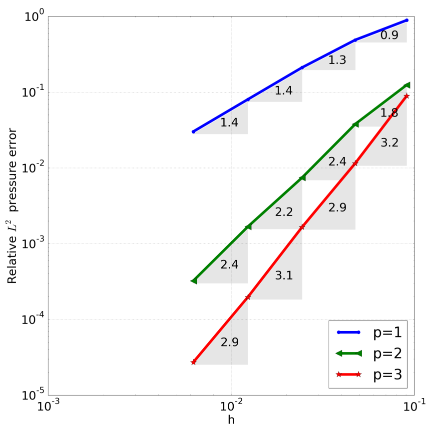

(c) L^2 pressue error

Fig. 4.9: Mesh convergence study of the steady Navier-Stokes equations with $\mu = 1$ in a quarter annulus ring using the skeleton-stabilized formulation with linear, quadratic and cubic full-regularity B-splines.

In Fig. 4.10 we study the solution sensitivity with respect to the skeleton stabilization parameter γ, where the ghost-penalty parameter is fixed at $\widetilde{\gamma} = 5 \times 10^{-3}$. The h-convergence behavior of the solution using C^1-continuous quadratic B-splines is studied for a wide range of stabilization parameters, *viz.* $\gamma \in (5\times10^{-5}, 10)$. We observe that the pressure stabilization parameter γ does not affect the accuracy of the velocity field in the L^2-norm and H^1-norm. This behavior is expected, as the Skeleton-penalty term acts only on the pressure field, similar as in the conforming isogeometric analysis setting considered in Ref. [188]. The pressure solution accuracy is affected by the selection of the stabilization parameter, but Fig. 4.10 conveys that the parameter can be selected from a wide range (approximately $\gamma \in (5 \times 10^{-4}, 5 \times 10^{-1})$) with minor influence on the accuracy. The convergence rate remains optimal for all considered choices of the stabilization parameter.

4.5.2 Navier-Stokes flow around a cylinder

We revisit the benchmark problem proposed by Schäfer and Turek [180], which we considered in the mesh-conforming isogeometric analysis setting in Ref. [188]. In this test case a cylinder of radius $R = 0.05\,\mathrm{m}$ is placed in a channel of height $H = 0.41\,\mathrm{m}$ and length $L = 2.2\,\mathrm{m}$. The center of the cylinder is positioned at a horizontal distance of $W = 0.2\,\mathrm{m}$ from the inflow boundary at $x = 0$, and at a vertical distance of $W = 0.2\,\mathrm{m}$ from the bottom channel wall at $y = 0$. Note that the cylinder has a small offset with respect to the center line of the channel, introducing a non-symmetry in the problem. At the inflow boundary the parabolic flow profile

$$\mathbf{u}(0, y) = \begin{pmatrix} 4U_m y(H - y)/H^2 \\ 0 \end{pmatrix}$$

with maximum velocity U_m is imposed. There is no slip at the bottom and top boundaries, as well as along the surface of the cylinder, and a natural boundary condition is used at the outflow boundary ($x = L$). The kinematic viscosity of the fluid is taken as $\mu = 1 \times 10^{-3}\,\mathrm{m}^2/\mathrm{s}$.

We consider the case of $\mathrm{Re} = 20$ – with the Reynolds number defined as $\mathrm{Re} = 2\bar{U}R/\mu$ (with mean inflow velocity $\bar{U} = \frac{2}{3}U_m$ – for which a steady flow is obtained. We consider a sequence of uniform refinements of a relatively coarse ambient domain mesh consisting of 36×22 elements. This coarsest level mesh is a non-uniformly spaced full-regularity B-spline patch, with

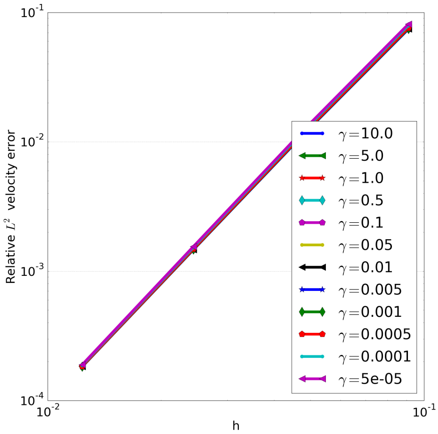

(a) L^2 velocity error

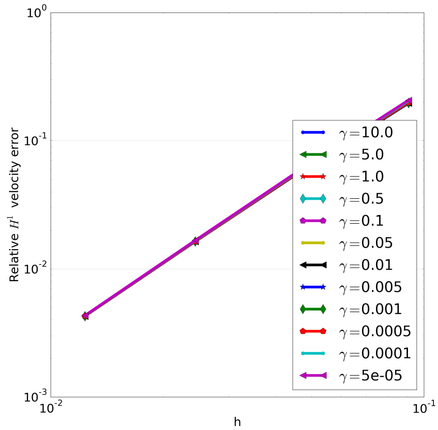

(b) H^1 velocity error

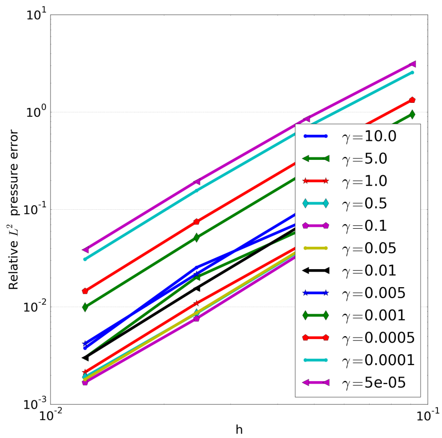

(c) L^2 pressure error

Fig. 4.10: Sensitivity of the quadratic spline approximation of the Navier-Stokes problem with $\mu = 1$ on the quarter annulus ring with respect to the stabilization parameter γ.

the knot values selected so that relatively small elements are obtained in the neighborhood of the cylindrical inclusion. The outer boundaries of the ambient domain mesh coincide with the boundaries of the physical domain. The essential boundary conditions are, however, still enforced weakly by Nitsche's method. Fig. 4.11 shows the speed and pressure computed on the three times refined second-order B-spline mesh, which results in a system of $n_{\mathrm{dof}} = 148476$ degrees of freedom. The obtained result is visually in good agreement with the benchmark result, and is free of pressure oscillations near the immersed boundary of the cylinder.

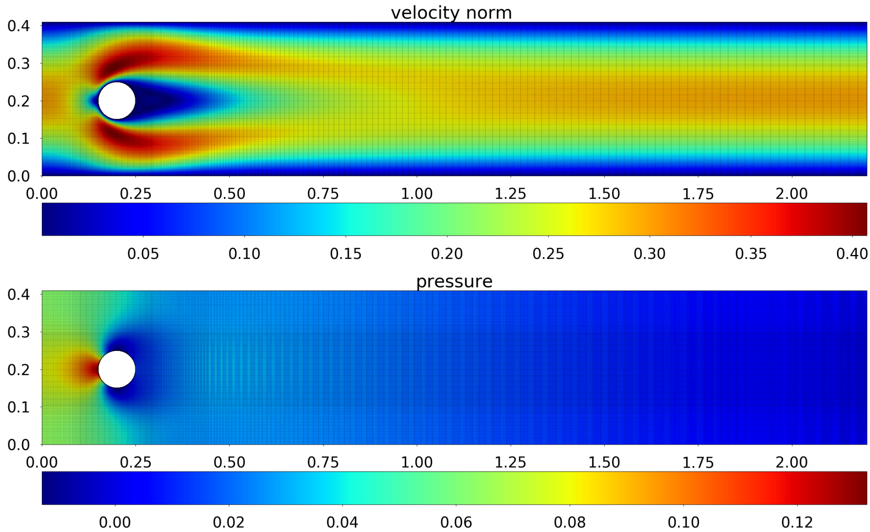

Fig. 4.11: Velocity magnitude (top) and pressure (bottom) solutions of the steady cylinder flow problem using quadratic B-splines with $n_{\mathrm{dof}} = 148476$.

In Table 4.1 we present the mesh converge results for various quantities of interest, *viz.* the lift and drag coefficients, c_L and c_D, respectively, and the pressure drop over the cylinder, Δp. The drag and lift coefficients are defined as

$$c_D = \frac{F_D}{\rho \bar{U} R} = \frac{\mathcal{R}(\mathbf{u}, p; \boldsymbol{\ell}_1)}{\rho \bar{U} R}, \qquad c_L = \frac{F_L}{\rho \bar{U} R} = \frac{\mathcal{R}(\mathbf{u}, p; \boldsymbol{\ell}_2)}{\rho \bar{U} R},$$

where F_D and F_L are the resultant drag and lift forces acting on the cylinder, which are evaluated weakly as (see *e.g.,* [181, 191, 192])

$$\mathcal{R}(\mathbf{u}^h, p^h; \boldsymbol{\ell}_i) := (\partial_t \mathbf{u}^h, \boldsymbol{\ell}_i) + c(\mathbf{u}^h; \mathbf{u}^h, \boldsymbol{\ell}_i) + a(\mathbf{u}^h, \boldsymbol{\ell}_i) - 2\mu\langle \nabla^s \boldsymbol{\ell}_i \cdot \mathbf{n}, \mathbf{u}^h - \mathbf{g}\rangle_{\Gamma_D} + b(p^h, \boldsymbol{\ell}_i),$$

with $\boldsymbol{\ell}_i \in [H^1_{0,\partial\Omega\setminus\Gamma}(\Omega)]^d$ and $\boldsymbol{\ell}_i|_\Gamma = -\mathbf{e}_i$, $i = 1, 2$. The pressure drop is defined as

$$\Delta p = p(W/2 - R, W/2) - p(W/2 + R, W/2).$$

From Table 4.1 it is observed that on the finest mesh all quantities of interest are in excellent agreement with the benchmark result [184]. We note that –

despite the fact that we here have selected the bi-sectioning integration depth to ten – with the higher-order approximation of these quantities of interest we anticipate deterioration of the approximation properties associated with the reduced geometric regularity of the immersed boundary approximation. We expect that the loss of convergence rate especially observed for the drag coefficient can be attributed to this, but further investigation of this aspect is warranted.

Level	n_{dof}	h_{cylinder}	C_D	C_L	Δp
0	2724	0.0142857	5.85317738567	0.009231742514	0.18749814772
1	9984	0.0071428	5.57503959343	0.011002907897	0.12424885895
2	38052	0.0035714	5.57961186549	0.010542479971	0.11504949327
3	148476	0.0017857	5.57989543774	0.010575002816	0.11703150638
Ref. [184]			5.57953523384	0.010618948146	0.11752016697

Table 4.1: Computed values of the drag and lift coefficients and pressure drop on four refinement levels using the skeleton-stabilized formulation with quadratic B-splines. The mesh resolution in the proximity of the cylinder is indicated by h_{cylinder}, and the total number of degrees of freedom by n_{dof}.

4.5.3 Scan-based analysis of a porous medium flow

To demonstrate the potential of the proposed formulation for geometrically and topologically complex three-dimensional domains, we consider a creeping flow through a porous medium. The porous medium under consideration is made of sintered glass beads. Three-dimensional gray-scale voxel data of the specimen is obtained by a μCT-scanner with a voxel resolution of 25 μm. We here consider a representative domain of $50 \times 50 \times 50$ voxels.

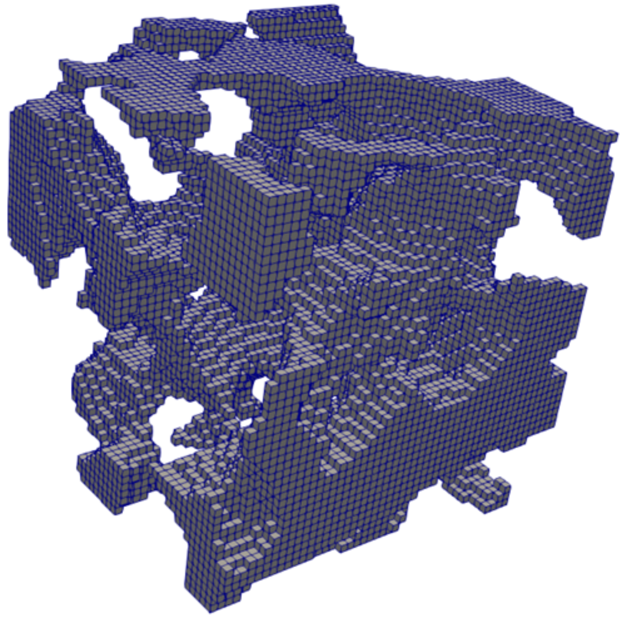

(a) Voxel domain

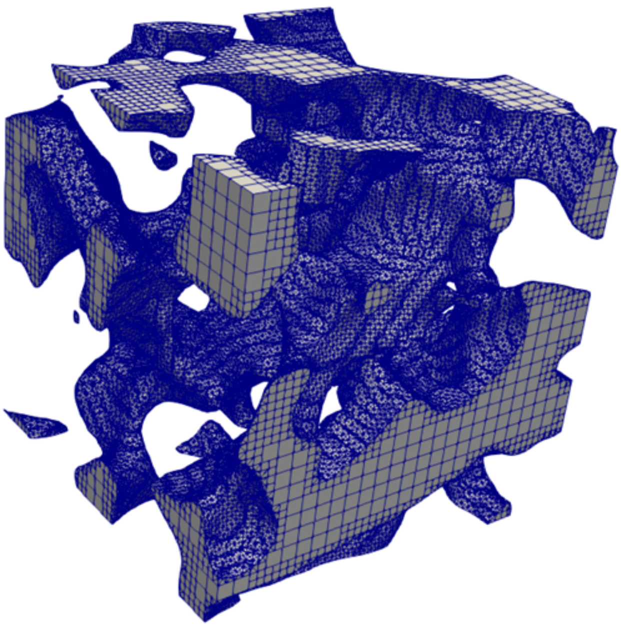

(b) Immersogeometric domain

Fig. 4.12: Two μCT-based geometric models of a sintered glass beads porous medium specimen. The original scan data consists of 125000 gray-scale voxels with a resolution of 25 μm.

In this numerical simulation we compare the immersogeometric approach considered in this work with a voxel-based analysis, which is commonly the method of choice for this type of analyses. The geometric model for the voxel-based analysis is obtained by direct segmentation of the gray-scale data, where all gray-scale values larger than a specified threshold are eliminated from the domain. The voxel model of the segmented void space – with a porosity of 28% – is shown in Fig. 4.12a. The B-spline based finite cell domain is obtained using the procedure proposed in Ref. [143]. First the gray-scale voxel data is smoothened by convolution of that data with a (second-order) B-spline basis constructed over the voxel grid, an operation that bears resemblance with Gaussian blurring. Then a relatively coarse (second-order) B-spline mesh, *i.c.* consisting of $12 \times 12 \times 12$ elements, is created over the ambient domain matching the scan size, so that the outer boundaries of the pore space reside in the boundaries of the scan domain. The smooth B-spline level set function is then segmented using the bi-sectioning procedure described in Section 4.2.2 with a bi-sectioning depth of two, where the threshold is calibrated based on the porosity of the voxel model. The corresponding integration mesh – again with a porosity of 28% – is shown in Fig. 4.12b.

Comparison of the two geometric models reveals that both models are visually very similar in terms of micro-structural features, which is expected based on the calibrated porosity. Evidently, the surface representation of the models is completely different. Whereas a staircase representation is obtained in the voxel model, a piecewise linear representation of the surface is obtained in the immersogeometric model, where it is noted that the intra-element curvature of the surface is partially recovered by the bi-sectioning operation (*i.e.*, the geometric linearization error is associated with the size of the integration sub-cells, and not with that of the size of the computational background mesh). This difference in surface representation translates directly in a significant difference of the internal surface area, which is equal to $15.5\,\mathrm{mm}^2$ for the voxel model, and to $9.45\,\mathrm{mm}^2$ for the immersogeometric model. Indeed, a significantly higher surface area is expected in the voxel representation. Adequate representation of the surface is critical in many situations, for example when surface reactions are considered such as in the case of biofilm growth and mineral dissolution/precipitation in porous media [193], or when one is interested in contact line dynamics for multi-phase porous media flows or elasto-capillarity [194–196].

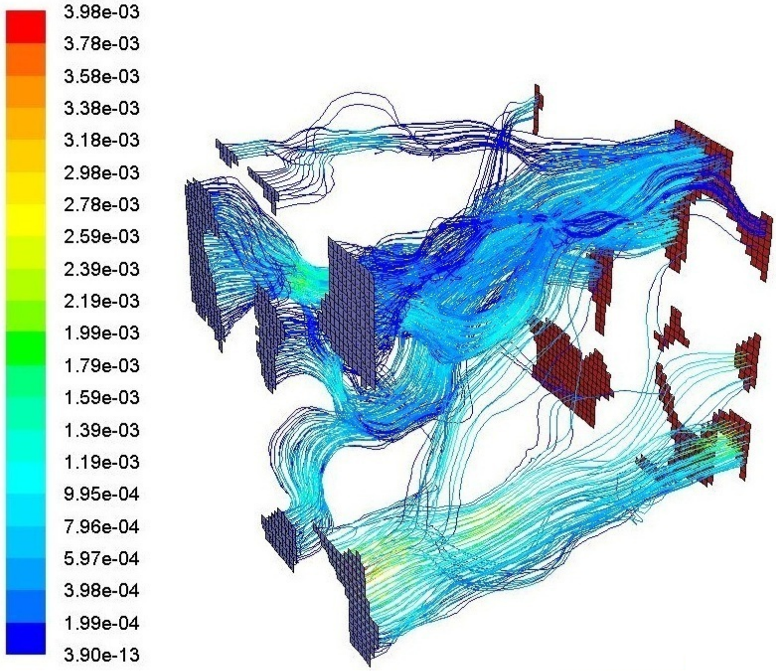

(a) FLUENT: Velocity streamlines

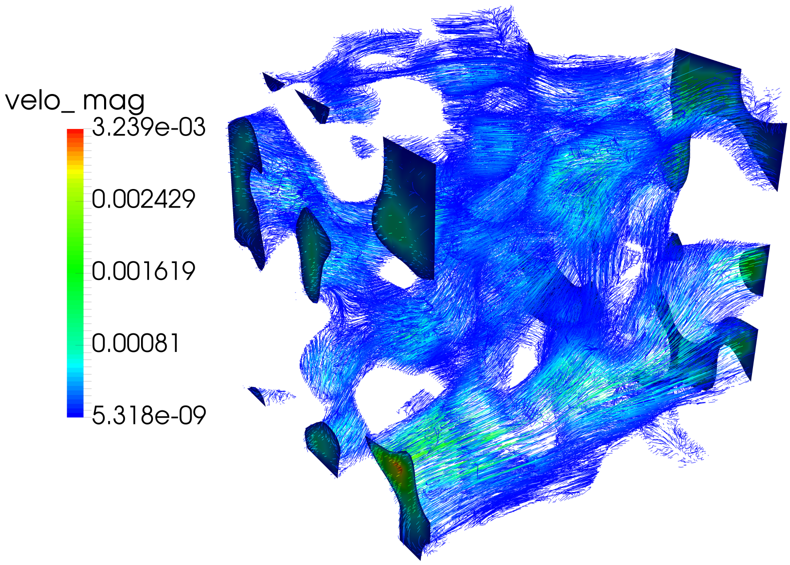

(b) Skeleton-stabilized ImmersoGeometric: Velocity streamlines

Fig. 4.13: Comparison of the voxel method and the skeleton-stabilized immersogeometric analysis results for the sintered glass beads specimen. The unit of velocity is m/s and Pa.

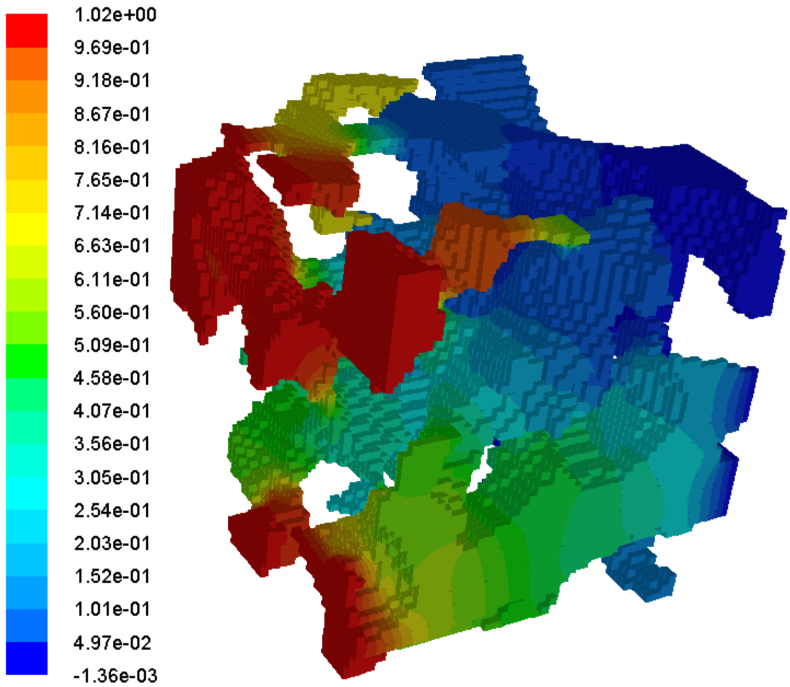

(c) FLUENT: Pressure

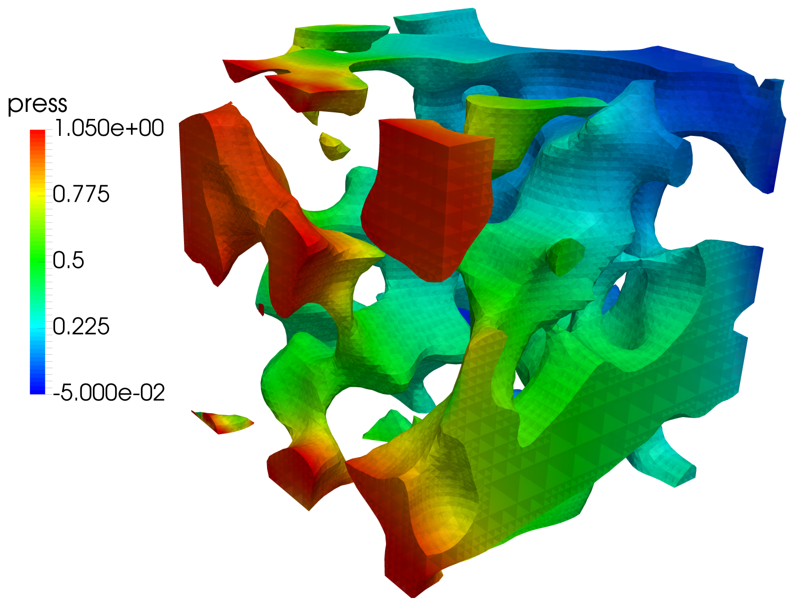

(d) Skeleton-stabilized ImmersoGeometric: Pressure

Fig. 4.13: (cont) Comparison of the voxel method and the skeleton-stabilized immersogeometric analysis results for the sintered glass beads specimen. The unit of pressure is Pa.

In Fig. 4.13 we compare the analysis results obtained using the two approaches for a creeping flow governed by the Stokes equations with viscosity $\mu = 10^{-3}$ Pa · s. The flow through the porous medium is forced by imposition of a pressure difference of 1 Pa between the inflow (left) and outflow (right) boundaries. All velocity components are zero on the other lateral boundaries, and no slip conditions are imposed on the interior surface. The voxel method results are obtained using FLUENT, which is essentially a finite volume method where the degrees of freedom are closely related with the 35383 pore space voxels. The immersogeometric results are obtained on the above-mentioned mesh using a second-order ($k = 2$) B-spline space, which contains approximately 13 times fewer degrees of freedom than the FLUENT mesh. The skeleton-penalty and ghost-penalty parameters are taken as $\gamma = 10^{-2}$ and $\widetilde{\gamma} = 10^{-4}$, respectively. From Fig. 4.13 we observe the results of both models to be in good correspondence, despite the difference in computational resolution. Let us note that although, because of post-processing artefacts, the streamline patterns for the two simulations are visually distinct, the flow fields are in fact very similar. It is important to note, however, that in terms of computational accuracy the two methods are fundamentally different. In the case of the voxel method, the computational resolution is closely tied to the geometric model, whereas for the immersogeometric approach, the computational mesh resolution can be controlled independent of the geometric model. As demonstrated in Ref. [143] for an elasticity problem, the decoupling of the computational resolution from the geometric model opens the doors to preforming (goal-)adaptive analyses with optimized meshes. In our future work we aim at applying a similar strategy to optimally compute homogenized permeability coefficients. Further optimization of the employed cut cell integration procedures in terms of computational effort – which, per-element, is significantly smaller for the voxel method – is required to allow upscaling to large scale specimens.

4.6 Conclusions

A stabilized formulation is proposed for the (immersed) finite cell simulation of unsteady incompressible flow problems using identical B-spline bases for the velocity and pressure fields. This formulation extends the developments in Ref. [188], where mesh-conforming isogeometric analysis of incompressible flow problems using identical pressure and velocity bases was considered. The pivotal idea behind the considered stabilization technique – which can be regarded as the isogeometric extension of the continuous interior penalty method – is that the inf-sup condition is bypassed by supplementing a penalty term for basis function derivative jumps across element interfaces, thereby effectively penalizing oscillatory pressure behavior. The mesh-conforming formulation is amended with a ghost-penalty stabilization to resolve ill-conditioning issues associated with small volume fraction cut cells in the immersed finite cell setting. This ghost-penalty term bears close resemblance with the pressure-stabilization operator, but acts on the velocity field in the vicinity of the immersed boundaries only.

An important aspect of this work is that we fully leverage the smoothness properties of the full-regularity B-spline basis functions constructed over the background mesh, in the sense that the stabilization operators only act on the highest-order normal derivatives of the basis functions via their interface jumps. All lower order derivatives vanish as a result of the continuity properties of the B-spline basis. One advantage of this isogeometric approach in comparison to the case of a Lagrange-based analysis is that it only requires a penalty parameter for the highest-order derivative jump. Moreover, the impact of the stabilization term on the sparsity pattern of the system matrix is significantly reduced when full-regularity B-splines are considered instead of Lagrange finite elements. This is an important benefit of the considered isogeometric approach from the perspective of computational effort.

In a series of two-dimensional benchmarks problems we have observed optimal rates of convergence for the L^2 and H^1-norms of the velocity field and the L^2 norm of the pressure field. In comparison to the immersed simulation results based on inf-sup stable isogeometric finite element pairs considered in Ref. [179], we observe oscillation-free pressure fields near the cut boundaries. As a result, using the skeleton-based stabilization technique considered herein, quantities of interest pertaining to the immersed boundaries can be computed reliably. It is noteworthy, however, that such quantities of interest are affected by the regularity of the immersed boundary representation, which in this work was based on a piece-wise linear representation corresponding to the bi-section based tessellation scheme used to construct quadrature rules for cut cells and their immersed boundaries.

An image-based three-dimensional analysis of a flow through a porous medium was presented, where the geometry is defined by segmentation of the smoothened μCT-scan voxel data. This simulation result demonstrates that the proposed stabilization technique scales to the three-dimensional setting, which opens the door to applying B-spline discretizations to topologically and geometrically complex volumetric domains.

The simulations considered herein were restricted to moderate Reynolds number flows on uniform background meshes. In this setting satisfactory results are obtained when the skeleton penalty parameter and ghost penalty parameter are taken equal. The rates of convergence have been observed to be insensitive to the choice of the penalization parameters for a wide range of considered values. Consistent with observation in the conforming case, the magnitude of the L^2 pressure error is observed to be influenced by the choice of the parameters, but a significant range of parameters exists for which this error is insensitive to the precise values of the parameters. This makes ad hoc selection of the parameters practical. The development of more specific selection criteria – preferably in the form of rigorously derived explicit expressions – is an import aspect of the further development of the proposed simulation framework.

As part of the further development of the mathematical analysis of the proposed formulation, in our future work we aim at obtaining a more fundamental understanding of the influence of geometric irregularities on the approximation quality. In relation to this, we also aim at exploiting the locally refined spline discretizations that can be constructed over the regular background mesh, and to use these refinements in a mesh-adaptive analysis. Extension to convection-dominated problems – which is a non-trivial extension in the sense that an additional convection-stabilization technique must be combined with the stabilization techniques already considered – is also an important topic of further study.

Chapter 5
Conclusions & Future prospects

5.1 Conclusions

In this thesis we set out to develop an immersed isogeometric finite element method for incompressible fluid flow problems. The point of departure for our study was to assess the applicability of inf-sup compatible spline discretizations for the Stokes problem – which have been demonstrated to yield excellent results in mesh-conforming isogeometric analysis – to an immersed finite cell setting. We found that the most prominent isogeometric families of inf-sup stable discretizations for the Stokes equation lose some of their attractiveness in the immersed setting. From the perspective of stability, this conclusion is motivated by the fact that we observe local oscillations in the pressure field near the cut boundaries, despite the fact that – at least for the geometrically simple problems considered herein – the numerical inf-sup constants are bounded below away from zero. Unphysical pressure oscillations are observed even on shape-regular cells with relatively large volume fractions. This observation suggests that the issue is more likely related to the local loss of inf-sup stability in the cut regions, rather than to ill-conditioning effects associated with small volume fraction cells. It is important to note that although for all element families quasi-optimal convergence rates (in the worst case, loss of about half an order) are observed for the H^1-norm and L^2-norm of the velocity and the L^2-norm for the pressure, oscillations on cut boundaries persist under mesh refinement for all considered families of mixed elements.

The oscillatory pressure field near the boundaries implies that quantities of interest that pertain to the boundary cannot be approximated reliably. This behavior impedes application of the method to moving-boundary and coupled problems such as fluid-structure interactions (FSI) and multi-phase problems, because in such scenarios the quality of the solution at the boundary is essential for the accuracy of the approximation of coupled systems. These accuracy complications worsen with increasing geometric complexity, particularly when the relative number of cut cells increases, which, from our point of view, makes these methods impractical for high-fidelity simulations in complex three-dimensional problems.

From this assessment we concluded that without modification of the formulation, inf-sup stable discretizations would lose their merits when applied in an immersed setting. This conclusion extends to Galerkin least-square type of stabilization techniques, in the sense that such stabilization techniques would also result in pressure oscillations near cut boundaries. This motivated us to develop an alternative formulation that is capable of exploiting the benefits of isogeometric analysis for immersed fluid flow problems. From our observations we infered that a satisfactory handling of pressure oscillations requires an approach that maintains its effectivity on cut cells, which motivated us to develop a stabilization technique based on the untrimmed background mesh. Conceptually, such a stabilization technique should be insensitive with respect to the cut cell volume fractions and configurations. The skeleton-based approach technique developed herein is inspired by the (continuous) interior-penalty method and ghost-penalty technique, which are known to effectively treat instabilities.

Although it would be sufficient to amend the inf-sup stable discretization of the mixed formulation with a stabilizing pressure term on the skeleton faces in the vicinity of the cut boundaries, we considered it more elegant and practical to apply the skeleton stabilization on the complete skeleton of the background mesh. This approach then treats the stabilization of the formulation for the interior part of the domain and the part associated with the cut boundary cells in a uniform manner, which effectively makes it possible to consider discretization of the pressure field and velocity field using the same spaces. The fact that the pressure stabilization is applied on the background mesh essentially implies that the cut cells are stabilized in exactly the same manner as the internal cells. In this approach it is furthermore natural to also supplement the skeleton of the cut cell boundaries with a ghost penalty term for the velocity field, thereby resolving ill-conditioning problems associated with small volume fraction cells within the same skeleton-based stabilization framework.

From the vantage point of practicality it is advantageous that our stabilization techniques enables consideration of the same space for the discretization of both the pressure and velocity fields. This possibility is not only useful in the immersed setting, but is also beneficial in the conforming isogeometric analysis setting, since it allows the direct usage of the CAD geometry parametrization basis (provided that it is analysis-suitable) for the discretization of all fields. In this sense our stabilization technique contributes to the integration of CAD and analysis for mixed form problems. An illustrative example of this benefit is provided in this thesis by the simulation of Navier-Stokes flow around a cylinder using a multi-patch NURBS geometry, for which results with a precision surpassing that of the state-of-the-art methods are obtained.

An elegant novelty of our stabilization approach – which can be regarded as the higher-regularity generalization of the (continuous) interior penalty stabilization technique – – is that it optimally benefits from the higher-order continuity of splines, since, in the full-regularity setting, only the highest order derivative jump is non-vanishing. A practical consequence of this is that only two stabilization parameters are required, *viz.* one for the background skeleton pressure stabilization, and one for the ghost cell velocity stabilization. From a computation-effort point of view, the higer-order continuity of splines leads to more sparse stabilization matrices, in comparison to interior penalty formulations for higher-order Lagrange finite elements.

The suitability of the proposed stabilized formulation for simulating immersed incompressible fluid flow problems with moderate Reynolds numbers has been demonstrated using a wide range of numerical test cases. The approach fully exploits the advantages associated with the higher-order smoothness of spline discretizations in the immersed setting, and fits seamlessly in the isogeometric analysis paradigm when considered in the mesh conforming setting.

5.2 Future prospects

In this thesis we have restricted ourselves to Stokes flows and moderate Reynolds numbers Navier-Stokes flows, for which convection-stabilization is not required. Extension of our skeleton-based stabilization technique to convection-dominated flows is non-trivial, in the sense that we anticipate that the current formulation needs to be supplemented with additional stabilization terms. Evidently, considering the structure of the developed stabilization framework, we wish to pursue a skeleton-based convection-stabilization method. This extension appears to be feasible, as such a skeleton-based stabilization of convective flows bears resemblance with (continuous) interior penalty methods. Moreover, the fact that established convection-stabilization techniques such as Variational Multiscale Methods (VMS) have already been applied in the immersed isogeometric setting, suggests that there are no fundamental roadblocks that would hinder combination of our stabilization technique with convection-stabilization. Further study on this topic is, however, required to develop an appropriate method, where a particular challenge will be to select the parameters for the various means of stabilization.

The mathematical analysis of the skeleton-stabilization framework developed herein, most notably its well-posedness, was beyond the scope of this thesis. Although our detailed numerical studies unambiguously indicate that the formulation can be applied successfully to a broad range of problems, a precise mathematical footing of the stabilization is indispensable to ensure stability in a general setting. We therefore consider further work on the mathematical analysis of the formulation essential. This analysis should also encompass the influence of the stabilization parameters. Although we have experienced selection of these parameters to be practical in the sense that a wide range of values can be chosen without having a significant influence on the approximation, it would be desirable if analysis-based guidelines for the parameter selection would be available.

The simulations considered in this work were all based on structured meshes. These meshes are typically graded toward regions that require high resolutions. Such refinements evidently propagate throughout tensor-product patches, which, in general, leads to unnecessary refinements. Considering the structure of the stabilization technique proposed herein, extension to hierarchical, locally refined meshes appears to be within reach. A future prospect of our developments is therefore to employ our stabilization technique in an adaptive setting, for which an additional challenge arises in the form of the construction of appropriate error estimators. Another extension that would improve the range of applicability of the proposed method is to enhance the formulation with high-regularity multi-patch coupling techniques. This extension would have the potential to couple geometrically incompatible patches, which would make it more practical from the point of view of CAD and analysis integration.

Finally, we note that the skeleton-based stabilization framework developed herein is anticipated to be applicable to a broad range of problems in computational physics and engineering. Evidently, incompressible and nearly-incompressible elasticity problems fit neatly in the developed framework, but extension to other multi-field problems is possible. One of the most interesting extensions in this sense would be to apply the formulation to fluid-structure interaction problems, since in such problems, in particular for flexible structures, the use of immersed techniques is commonly attractive. Another interesting extension is to consider (immersed) coupled problems with more than two fields. Our stabilization technique has the potential to significantly ease the discretization and implementation of such problems, by virtue of the fact that identical approximation spaces can be used for all fields. Also, the use of a high-order geometry representation in order to optimally approximate sensitive quantities of interests defined at the cut-boundaries is a topic of further study.

References

[1] C.L. Fefferman. Existence and smoothness of the navier-stokes equation. *The millennium prize problems*, pages 57–67, 2006.

[2] P. G. Ciarlet. *The finite element method for elliptic problems*, volume 4. North Holland, 1978.

[3] T. J. R. Hughes. *The finite element method: linear static and dynamic finite element analysis*, volume 65. Dover Publications, 2000.

[4] K.J. Bathe. *Finite element procedures*. Klaus-Jurgen Bathe, 2006.

[5] I. Babuška. The finite element method with lagrangian multipliers. *Numerische Mathematik*, 20(3):179–192, 1973.

[6] F. Brezzi. On the existence, uniqueness and approximation of saddle-point problems arising from lagrangian multipliers. *Revue française d'automatique, informatique, recherche opérationnelle. Analyse numérique*, 8(2):129–151, 1974.

[7] O. A. Ladyzhenskaya. *The mathematical theory of viscous incompressible flow*. Second English edition, revised and enlarged. Translated from the Russian by Richard A. Silverman and John Chu. Mathematics and its Applications, Vol. 2. Gordon and Breach, Science Publishers, New York-London-Paris, 1969.

[8] J. Nečas. Sur une méthode pour résoudre les équations aux dérivées partielles du type elliptique, voisine de la variationnelle. *Annali della Scuola Normale Superiore di Pisa - Classe di Scienze*, 16(4):305–326, 1962.

[9] V. Girault and P.A. Raviart. Finite element approximation of the navier-stokes equations, vol. 749 of lecture notes in mathematics. *Springer-Verlag, Berlin*, 4:12, 1979.

[10] V. Girault and P.A. Raviart. Finite element approximations of the navier-stokes equations, theory and algorithms, 1986.

[11] V. Girault and P.A. Raviart. *Finite element methods for Navier-Stokes equations: theory and algorithms*, volume 5. Springer Science & Business Media, 2012.

[12] F. Brezzi and M. Fortin. Mixed and hybrid finite element methods, no. 15 in springer series in computational mathematics, 1991.

[13] D. Boffi, F. Brezzi, and M. Fortin. *Mixed finite element methods and applications*. Springer, 2013.

[14] Douglas N Arnold and Anders Logg. Periodic table of the finite elements. *SIAM News*, 47(9):212, 2014.

[15] D.N. Arnold, R.S. Falk, and R. Winther. Finite element exterior calculus, homological techniques, and applications. *Acta numerica*, 15:1–155, 2006.

[16] D.N. Arnold, R. Falk, and R. Winther. Finite element exterior calculus: from hodge theory to numerical stability. *Bulletin of the American mathematical society*, 47(2):281–354, 2010.

[17] R. Hiptmair. Finite elements in computational electromagnetism. *Acta Numerica*, 11:237–339, 2002.

[18] F. Brezzi and J. Pitkäranta. On the stabilization of finite element approximations of the stokes equations. In *Efficient solutions of elliptic systems*, pages 11–19. Springer, 1984.

[19] T.J.R. Hughes, L.P. Franca, and M. Balestra. A new finite element formulation for computational fluid dynamics: V. circumventing the babuška-brezzi condition: a stable petrov-galerkin formulation of the stokes problem accommodating equal-order interpolations. *Computer Methods in Applied Mechanics and Engineering*, 59(1):85–99, 1986.

[20] T.J.R. Hughes and L.P. Franca. A new finite element formulation for computational fluid dynamics: Vii. the stokes problem with various well-posed boundary conditions: symmetric formulations that converge for all velocity/pressure spaces. *Computer Methods in Applied Mechanics and Engineering*, 65(1):85–96, 1987.

[21] T.J.R. Hughes, L.P. Franca, and G.M. Hulbert. A new finite element formulation for computational fluid dynamics: Viii. the galerkin/least-squares method for advective-diffusive equations. *Computer Methods in Applied Mechanics and Engineering*, 73(2):173–189, 1989.

[22] J. Douglas and J.P. Wang. An absolutely stabilized finite element method for the stokes problem. *Mathematics of computation*, 52(186):495–508, 1989.

[23] T.E. Tezduyar. Stabilized finite element formulations for incompressible flow computations. *Advances in applied mechanics*, 28:1–44, 1991.

[24] T.J.R. Hughes. Multiscale phenomena: Green's functions, the dirichlet-to-neumann formulation, subgrid scale models, bubbles and the origins of stabilized methods. *Computer methods in applied mechanics and engineering*, 127(1-4):387–401, 1995.

[25] T.J.R. Hughes, G.R. Feijóo, L. Mazzei, and J.B. Quincy. The variational multiscale method—a paradigm for computational mechanics. *Computer methods in applied mechanics and engineering*, 166(1-2):3–24, 1998.

[26] T.J.R. Hughes, L. Mazzei, and K.E. Jansen. Large eddy simulation and the variational multiscale method. *Computing and Visualization in Science*, 3(1):47–59, 2000.

[27] T.J.R. Hughes, A.A. Oberai, and L. Mazzei. Large eddy simulation of turbulent channel flows by the variational multiscale method. *Physics of fluids*, 13(6):1784–1799, 2001.

[28] Y. Bazilevs, V.M. Calo, J.A. Cottrell, T.J.R. Hughes, A. Reali, and G.Scovazzi. Variational multiscale residual-based turbulence modeling for large eddy simulation of incompressible flows. *Computer Methods in Applied Mechanics and Engineering*, 197(1-4):173–201, 2007.

[29] A. Campion-Renson and M.J. Crochet. On the stream function-vorticity finite element solutions of navier-stokes equations. *International Journal for Numerical Methods in Engineering*, 12(12):1809–1818, 1978.

[30] T.E. Tezduyar, R. Glowinski, and J. Liou. Petrov-galerkin methods on multiply connected domains for the vorticity-stream function formulation of the incompressible navier-stokes equations. *International journal for numerical methods in fluids*, 8(10):1269–1290, 1988.

[31] W.F. Spotz and G.F. Carey. High-order compact scheme for the steady stream-function vorticity equations. *International Journal for Numerical Methods in Engineering*, 38(20):3497–3512, 1995.

[32] F. Dubois, M. Salaün, and S. Salmon. Vorticity–velocity-pressure and stream function-vorticity formulations for the stokes problem. *Journal de mathématiques pures et appliquées*, 82(11):1395–1451, 2003.

[33] R. Codina. Stabilization of incompressibility and convection through orthogonal sub-scales in finite element methods. *Computer methods in applied mechanics and engineering*, 190(13):1579–1599, 2000.

[34] R. Codina. A stabilized finite element method for generalized stationary incompressible flows. *Computer Methods in Applied Mechanics and Engineering*, 190(20):2681–2706, 2001.

[35] R. Codina. Pressure stability in fractional step finite element methods for incompressible flows. *Journal of Computational Physics*, 170(1):112–140, 2001.

[36] R. Codina and J. Blasco. Stabilized finite element method for the transient navier–stokes equations based on a pressure gradient projection. *Computer Methods in Applied Mechanics and Engineering*, 182(3):277–300, 2000.

[37] C.R. Dohrmann and P.B. Bochev. A stabilized finite element method for the stokes problem based on polynomial pressure projections. *International Journal for Numerical Methods in Fluids*, 46(2):183–201, 2004.

[38] M. Braack and E. Burman. Local projection stabilization for the oseen problem and its interpretation as a variational multiscale method. *SIAM Journal on Numerical Analysis*, 43(6):2544–2566, 2006.

[39] M. Braack and G. Lube. Finite elements with local projection stabilization for incompressible flow problems. *Journal of Computational Mathematics*, pages 116–147, 2009.

[40] E. Burman and P. Hansbo. Edge stabilization for the generalized stokes problem: a continuous interior penalty method. *Computer methods in applied mechanics and engineering*, 195(19):2393–2410, 2006.

[41] E. Burman, M.A. Fernández, and P. Hansbo. Continuous interior penalty finite element method for oseen's equations. *SIAM journal on numerical analysis*, 44(3):1248–1274, 2006.

[42] E. Burman and M.A. Fernández. Continuous interior penalty finite element method for the time-dependent navier–stokes equations: space discretization and convergence. *Numerische Mathematik*, 107(1):39–77, 2007.

[43] J.A. Cottrell, T.J.R. Hughes, and Y. Bazilevs. *Isogeometric analysis: Toward integration of CAD and FEA*. Wiley, 2009.

[44] T.J.R. Hughes, J.A. Cottrell, and Y. Bazilevs. Isogeometric analysis: CAD, finite elements, NURBS, exact geometry and mesh refinement.

Computer Methods in Applied Mechanics and Engineering, 194(39-41):4135–4195, 2005.

[45] O.M. Sapondzhyan. Bending of a simply supported polygonal plate. *Akad. Nauk Armyan. SSR. Izv. Fiz.-Mat. Estest. Tehn. Nauki*, 5(2), 1952.

[46] I. Babuška and J. Pitkäranta. The plate paradox for hard and soft simple support. *SIAM Journal on Mathematical Analysis*, 21(3):551–576, 1990.

[47] L. A. Piegl and W. Tiller. *The NURBS book*. Springer Verlag, 1997.

[48] G.E. Farin. *NURBS: from projective geometry to practical use*. AK Peters, Ltd., 1999.

[49] E.A. Cohen, G.A. Elber, et al. *Geometric modeling with splines: an introduction*. AK Peters Ltd, 2001.

[50] David F. Rogers. *An introduction to NURBS: with historical perspective*. Elsevier, 2000.

[51] J.A. Cottrell, A. Reali, Y. Bazilevs, and T.J.R. Hughes. Isogeometric analysis of structural vibrations. *Computer Methods in Applied Mechanics and Engineering*, 195(41-43):5257–5296, 2006.

[52] J.A. Cottrell, T.J.R. Hughes, and A. Reali. Studies of refinement and continuity in isogeometric structural analysis. *Computer methods in applied mechanics and engineering*, 196(41):4160–4183, 2007.

[53] J Kiendl, K-U Bletzinger, J Linhard, and R Wüchner. Isogeometric shell analysis with Kirchhoff–Love elements. *Computer Methods in Applied Mechanics and Engineering*, 198(49):3902–3914, 2009.

[54] J. Kiendl, Y. Bazilevs, M-C. Hsu, R. Wüchner, and K-U. Bletzinger. The bending strip method for isogeometric analysis of Kirchhoff–Love shell structures comprised of multiple patches. *Computer Methods in Applied Mechanics and Engineering*, 199(37):2403–2416, 2010.

[55] D.J. Benson, Y. Bazilevs, M.C. Hsu, and T.J.R. Hughes. Isogeometric shell analysis: the Reissner–Mindlin shell. *Computer Methods in Applied Mechanics and Engineering*, 199(5):276–289, 2010.

[56] D.J. Benson, Y. Bazilevs, M.C. Hsu, and T.J.R. Hughes. A large deformation, rotation-free, isogeometric shell. *Computer Methods in Applied Mechanics and Engineering*, 200(13-16):1367–1378, 2011.

[57] N. Nguyen-Thanh, J. Kiendl, H. Nguyen-Xuan, R. Wuchner, K.U. Bletzinger, Y. Bazilevs, and T. Rabczuk. Rotation free isogeometric thin shell analysis using PHT-splines. *Computer Methods in Applied Mechanics and Engineering*, 200(47-48):3410–3424, 2011.

[58] Y. Bazilevs and I. Akkerman. Large eddy simulation of turbulent Taylor-Couette flow using isogeometric analysis and the residual-based variational multiscale method. *Journal of Computational Physics*, 229(9):3402–3414, 2010.

[59] Y. Bazilevs, V.M. Calo, Y. Zhang, and T.J.R. Hughes. Isogeometric fluid-structure interaction analysis with applications to arterial blood flow. *Computational Mechanics*, 38(4):310–322, 2006.

[60] Y. Bazilevs, VM Calo, T.J.R. Hughes, and Y. Zhang. Isogeometric fluid-structure interaction: theory, algorithms, and computations. *Computational mechanics*, 43(1):3–37, 2008.

[61] Y. Bazilevs, J.R. Gohean, T.J.R. Hughes, R.D. Moser, and Y. Zhang. Patient-specific isogeometric fluid–structure interaction analysis of thoracic aortic blood flow due to implantation of the jarvik 2000 left ventricular assist device. *Computer Methods in Applied Mechanics and Engineering*, 198(45):3534–3550, 2009.

[62] Y. Bazilevs, M-C. Hsu, and M.A. Scott. Isogeometric fluid–structure interaction analysis with emphasis on non-matching discretizations, and with application to wind turbines. *Computer Methods in Applied Mechanics and Engineering*, 249:28–41, 2012.

[63] A Buffa, J Rivas, G Sangalli, and R Vázquez. Isogeometric discrete differential forms in three dimensions. *SIAM Journal on Numerical Analysis*, 49(2):818–844, 2011.

[64] A Buffa, G Sangalli, and R Vázquez. Isogeometric methods for computational electromagnetics: B-spline and t-spline discretizations. *Journal of Computational Physics*, 257:1291–1320, 2014.

[65] A. Ratnani and E. Sonnendrücker. Isogeometric analysis in reduced magnetohydrodynamics. *Computational Science & Discovery*, 5(1):014007, 2012.

[66] L. de Lorenzis, I. Temizer, P. Wriggers, and G. Zavarise. A large deformation frictional contact formulation using nurbs-based isogeometric analysis. *International Journal for Numerical Methods in Engineering*, 87(13):1278–1300, 2011.

[67] L De Lorenzis, P Wriggers, and G Zavarise. A mortar formulation for 3d large deformation contact using nurbs-based isogeometric analysis and the augmented lagrangian method. *Computational Mechanics*, 49(1):1–20, 2012.

[68] J. Lu. Isogeometric contact analysis: Geometric basis and formulation for frictionless contact. *Computer Methods in Applied Mechanics and*

Engineering, 200(5):726–741, 2011.

[69] I. Temizer, P. Wriggers, and T.J.R. Hughes. Contact treatment in isogeometric analysis with nurbs. *Computer Methods in Applied Mechanics and Engineering*, 200(9):1100–1112, 2011.

[70] W.A. Wall, M.A. Frenzel, and C. Cyron. Isogeometric structural shape optimization. *Computer methods in applied mechanics and engineering*, 197(33):2976–2988, 2008.

[71] X. Qian. Full analytical sensitivities in nurbs based isogeometric shape optimization. *Computer Methods in Applied Mechanics and Engineering*, 199(29):2059–2071, 2010.

[72] S. Cho and S.H. Ha. Isogeometric shape design optimization: exact geometry and enhanced sensitivity. *Structural and Multidisciplinary Optimization*, 38(1):53–70, 2009.

[73] K. Li and X. Qian. Isogeometric analysis and shape optimization via boundary integral. *Computer-Aided Design*, 43(11):1427–1437, 2011.

[74] J. Kiendl, R. Schmidt, R. Wüchner, and K.U. Bletzinger. Isogeometric shape optimization of shells using semi-analytical sensitivity analysis and sensitivity weighting. *Computer Methods in Applied Mechanics and Engineering*, 274:148–167, 2014.

[75] M. Nguyen Dang, A. Evgrafov, A.R. Gersborg, and J. Gravesen. Isogeometric shape optimization of vibrating membranes. *Computer Methods in Applied Mechanics and Engineering*, 200(13):1343–1353, 2011.

[76] E. De Luycker, D.J. Benson, T. Belytschko, Y. Bazilevs, and M.C. Hsu. X-fem in isogeometric analysis for linear fracture mechanics. *International Journal for Numerical Methods in Engineering*, 87(6):541–565, 2011.

[77] C.V. Verhoosel, M.A. Scott, T.J.R. Hughes, and R. De Borst. An isogeometric analysis approach to gradient damage models. *International Journal for Numerical Methods in Engineering*, 86(1):115–134, 2011.

[78] C.V. Verhoosel, M.A. Scott, R. de Borst, and T.J.R. Hughes. An isogeometric approach to cohesive zone modeling. *International Journal for Numerical Methods in Engineering*, 87(1-5):336–360, 2011.

[79] H. Gómez, V.M. Calo, Y. Bazilevs, and T.J.R. Hughes. Isogeometric analysis of the cahn–hilliard phase-field model. *Computer methods in applied mechanics and engineering*, 197(49):4333–4352, 2008.

[80] M.J. Borden, C.V. Verhoosel, M.A. Scott, T.J.R. Hughes, and C.M. Landis. A phase-field description of dynamic brittle fracture. *Computer Methods in Applied Mechanics and Engineering*, 217:77–95, 2012.

[81] M.J. Borden, T.J.R. Hughes, C.M. Landis, and C.V. Verhoosel. A higher-order phase-field model for brittle fracture: Formulation and analysis within the isogeometric analysis framework. *Computer Methods in Applied Mechanics and Engineering*, 273:100–118, 2014.

[82] K.G. Van der Zee and C.V. Verhoosel. Isogeometric analysis-based goal-oriented error estimation for free-boundary problems. *Finite Elements in Analysis and Design*, 47(6):600–609, 2011.

[83] H. Nguyen-Xuan, T. Hoang, and V.P. Nguyen. An isogeometric analysis for elliptic homogenization problems. *Computers & Mathematics with Applications*, 67(9):1722–1741, 2014.

[84] I. Temizer. Multiscale thermomechanical contact: Computational homogenization with isogeometric analysis. *International Journal for Numerical Methods in Engineering*, 97(8):582–607, 2014.

[85] Y. Bazilevs, V.M. Calo, J.A. Cottrell, J.A. Evans, T.J.R. Hughes, S. Lipton, M.A. Scott, and T.W. Sederberg. Isogeometric analysis using T-splines. *Computer Methods in Applied Mechanics and Engineering*, 199(5-8):229–263, 2010.

[86] M.A. Scott, M.J. Borden, C.V. Verhoosel, T.W. Sederberg, and T.J.R. Hughes. Isogeometric finite element data structures based on Bézier extraction of T-splines. *International Journal for Numerical Methods in Engineering*, 88(2):126–156, 2011.

[87] F. Auricchio, L.B. Da Veiga, T.J.R. Hughes, A. Reali, and G. Sangalli. Isogeometric collocation methods. *Mathematical Models and Methods in Applied Sciences*, 20(11):2075–2107, 2010.

[88] D. Schillinger, J.A. Evans, A. Reali, M.A. Scott, and T.J.R. Hughes. Isogeometric collocation: Cost comparison with Galerkin methods and extension to adaptive hierarchical NURBS discretizations. *Computer Methods in Applied Mechanics and Engineering*, 267:170–232, 2013.

[89] F. Auricchio, L. Beirao da Veiga, T. J. R. Hughes, A. Reali, and G. Sangalli. Isogeometric collocation for elastostatics and explicit dynamics. *Computer methods in applied mechanics and engineering*, 249:2–14, 2012.

[90] R.N. Simpson, S.P.A. Bordas, J. Trevelyan, and T. Rabczuk. A two-dimensional isogeometric boundary element method for elastostatic analysis. *Computer Methods in Applied Mechanics and Engineering*, 209:87–100, 2012.

[91] Michael A Scott, Robert N Simpson, John A Evans, Scott Lipton, Stephane PA Bordas, Thomas JR Hughes, and Thomas W Sederberg.

Isogeometric boundary element analysis using unstructured t-splines. *Computer Methods in Applied Mechanics and Engineering*, 254:197–221, 2013.

[92] P.J. Barendrecht. Isogeometric analysis for subdivision surfaces. *Eindhoven University of Technology: Eindhoven, The Netherlands*, 2013.

[93] A. Riffnaller-Schiefer, U.H. Augsdörfer, and D.W. Fellner. Isogeometric shell analysis with nurbs compatible subdivision surfaces. *Applied Mathematics and Computation*, 272(Part 1):139 – 147, 2016. Subdivision, Geometric and Algebraic Methods, Isogeometric Analysis and Refinability.

[94] Y. Bazilevs, L. Beirao da Veiga, J. A. Cottrell, T. J. R. Hughes, and G. Sangalli. Isogeometric analysis: approximation, stability and error estimates for h-refined meshes. *Mathematical Models and Methods in Applied Sciences*, 16(07):1031–1090, 2006.

[95] S. Lipton, J.A. Evans, Y. Bazilevs, T. Elguedj, and T.J.R. Hughes. Robustness of isogeometric structural discretizations under severe mesh distortion. *Computer Methods in Applied Mechanics and Engineering*, 199(5):357–373, 2010.

[96] L.B. Da Veiga, A. Buffa, J. Rivas, and G. Sangalli. Some estimates for h–p–k-refinement in isogeometric analysis. *Numerische Mathematik*, 118(2):271–305, 2011.

[97] A. Tagliabue, L. Dede, and A. Quarteroni. Isogeometric analysis and error estimates for high order partial differential equations in fluid dynamics. *Computers & Fluids*, 102:277–303, 2014.

[98] V.P. Nguyen, P. Kerfriden, M. Brino, S.P.A. Bordas, and E. Bonisoli. Nitsche's method for two and three dimensional nurbs patch coupling. *Computational Mechanics*, 53(6):1163–1182, 2014.

[99] M. Ruess, D. Schillinger, A.I. Ozcan, and E. Rank. Weak coupling for isogeometric analysis of non-matching and trimmed multi-patch geometries. *Computer Methods in Applied Mechanics and Engineering*, 269:46 – 71, 2014.

[100] W. Dornisch, G. Vitucci, and S. Klinkel. The weak substitution method–an application of the mortar method for patch coupling in NURBS-based isogeometric analysis. *International Journal for Numerical Methods in Engineering*, 103(3):205–234, 2015.

[101] E. Brivadis, A. Buffa, B. Wohlmuth, and L. Wunderlich. Isogeometric mortar methods. *Computer Methods in Applied Mechanics and Engineering*, 284:292 – 319, 2015.

[102] M. Aigner, C. Heinrich, B. Juttler, E. Pilgerstorfer, B. Simeon, and A. Vuong. Swept volume parameterization for isogeometric analysis. *Mathematics of Surfaces XIII*, pages 19–44, 2009.

[103] A. Apostolatos, R. Schmidt, R. Wüchner, and K.U. Bletzinger. A nitsche-type formulation and comparison of the most common domain decomposition methods in isogeometric analysis. *International Journal for Numerical Methods in Engineering*, 97(7):473–504, 2014.

[104] A-V. Vuong, C. Giannelli, B. Jüttler, and B. Simeon. A hierarchical approach to adaptive local refinement in isogeometric analysis. *Computer Methods in Applied Mechanics and Engineering*, 200(49):3554–3567, 2011.

[105] M.R. Dörfel, B. Jüttler, and B. Simeon. Adaptive isogeometric analysis by local h-refinement with T-splines. *Computer methods in applied mechanics and engineering*, 199(5):264–275, 2010.

[106] M.A. Scott, X. Li, T.W. Sederberg, and T.J.R. Hughes. Local refinement of analysis-suitable T-splines. *Computer Methods in Applied Mechanics and Engineering*, 213:206–222, 2012.

[107] D. Groisser and J. Peters. Matched gk-constructions always yield ck-continuous isogeometric elements. *Computer aided geometric design*, 34:67–72, 2015.

[108] D. Toshniwal, H. Speleers, and T.J.R. Hughes. Smooth cubic spline spaces on unstructured quadrilateral meshes with particular emphasis on extraordinary points: Geometric design and isogeometric analysis considerations. *Computer Methods in Applied Mechanics and Engineering*, 2017.

[109] A. Buffa, H. Harbrecht, A. Kunoth, and G. Sangalli. Bpx-preconditioning for isogeometric analysis. *Computer Methods in Applied Mechanics and Engineering*, 265:63–70, 2013.

[110] K.P.S. Gahalaut, S.K. Tomar, and J.K. Kraus. Algebraic multilevel preconditioning in isogeometric analysis: Construction and numerical studies. *Computer Methods in Applied Mechanics and Engineering*, 266:40–56, 2013.

[111] N. Collier, L. Dalcin, D. Pardo, and V.M. Calo. The cost of continuity: performance of iterative solvers on isogeometric finite elements. *SIAM Journal on Scientific Computing*, 35(2):A767–A784, 2013.

[112] L.B. da Veiga, D. Cho, L.F. Pavarino, and S. Scacchi. Isogeometric schwarz preconditioners for linear elasticity systems. *Computer Methods in Applied Mechanics and Engineering*, 253:439–454, 2013.

[113] G. Sangalli and M. Tani. Isogeometric preconditioners based on fast solvers for the sylvester equation. *SIAM Journal on Scientific Computing*, 38(6):A3644–A3671, 2016.

[114] L. Beirao da Veiga, A Buffa, G. Sangalli, and R. Vázquez. Mathematical analysis of variational isogeometric methods. *Acta Numerica*, 23:157–287, 5 2014.

[115] T.J.R. Hughes, A. Reali, and G. Sangalli. Efficient quadrature for nurbs-based isogeometric analysis. *Computer methods in applied mechanics and engineering*, 199(5):301–313, 2010.

[116] F. Auricchio, F. Calabro, T.J.R. Hughes, A. Reali, and G. Sangalli. A simple algorithm for obtaining nearly optimal quadrature rules for nurbs-based isogeometric analysis. *Computer Methods in Applied Mechanics and Engineering*, 249:15–27, 2012.

[117] F. Calabrò, G. Sangalli, and M. Tani. Fast formation of isogeometric galerkin matrices by weighted quadrature. *Computer Methods in Applied Mechanics and Engineering*, 316:606–622, 2017.

[118] A. Buffa, C. de Falco, and G. Sangalli. IsoGeometric Analysis: Stable elements for the 2D Stokes equation. *International Journal for Numerical Methods in Fluids*, 65(11-12):1407–1422, 2011.

[119] A. Bressan and G. Sangalli. Isogeometric discretizations of the Stokes problem: stability analysis by the macroelement technique. *IMA Journal of Numerical Analysis*, 33(2):629–651, 2013.

[120] T Rüberg and F Cirak. Subdivision-stabilised immersed B-spline finite elements for moving boundary flows. *Computer Methods in Applied Mechanics and Engineering*, 209:266–283, 2012.

[121] J.A. Evans and T.J.R. Hughes. Isogeometric divergence-conforming B-splines for the Darcy–Stokes–Brinkman equations. *Mathematical Models and Methods in Applied Sciences*, 23(04):671–741, 2013.

[122] J.A. Evans and T.J.R. Hughes. Isogeometric divergence-conforming b-splines for the steady navier–stokes equations. *Mathematical Models and Methods in Applied Sciences*, 23(08):1421–1478, 2013.

[123] J.A. Evans and T.J.R. Hughes. Isogeometric divergence-conforming b-splines for the unsteady navier–stokes equations. *Journal of Computational Physics*, 241:141–167, 2013.

[124] C.S. Peskin. The immersed boundary method. *Acta numerica*, 11:479–517, 2002.

[125] D. Boffi and L. Gastaldi. A finite element approach for the immersed boundary method. *Computers & structures*, 81(8):491–501, 2003.

[126] L. Lee and R.J. LeVeque. An immersed interface method for incompressible navier–stokes equations. *SIAM Journal on Scientific Computing*, 25(3):832–856, 2003.

[127] J. Kim, D. Kim, and H. Choi. An immersed-boundary finite-volume method for simulations of flow in complex geometries. *Journal of Computational Physics*, 171(1):132–150, 2001.

[128] A. Pinelli, I.Z. Naqavi, U. Piomelli, and J. Favier. Immersed-boundary methods for general finite-difference and finite-volume navier–stokes solvers. *Journal of Computational Physics*, 229(24):9073–9091, 2010.

[129] J. Yang, S. Preidikman, and E. Balaras. A strongly coupled, embedded-boundary method for fluid–structure interactions of elastically mounted rigid bodies. *Journal of Fluids and Structures*, 24(2):167–182, 2008.

[130] T. Ye, R. Mittal, H.S. Udaykumar, and W. Shyy. An accurate cartesian grid method for viscous incompressible flows with complex immersed boundaries. *Journal of computational physics*, 156(2):209–240, 1999.

[131] M. Ismail. *The fat boundary method for the numerical resolution of elliptic problems in perforated domains. Application to 3D Fluid Flows*. PhD thesis, PhD thesis, University Pierre and Marie Curie-Paris VI, France, 2004.

[132] J.M. Melenk and I. Babuška. The partition of unity finite element method: basic theory and applications. *Computer methods in applied mechanics and engineering*, 139(1-4):289–314, 1996.

[133] J. Dolbow and T. Belytschko. A finite element method for crack growth without remeshing. *International journal for numerical methods in engineering*, 46(1):131–150, 1999.

[134] T.P. Fries and T. Belytschko. The extended/generalized finite element method: an overview of the method and its applications. *International Journal for Numerical Methods in Engineering*, 84(3):253–304, 2010.

[135] K. Höllig. *Finite element methods with B-splines*. SIAM, 2003.

[136] E. Burman, S. Claus, P. Hansbo, M.G. Larson, and A. Massing. Cutfem: Discretizing geometry and partial differential equations. *International Journal for Numerical Methods in Engineering*, 104(7):472–501, 2015.

[137] A. Düster, J. Parvizian, Z. Yang, and E. Rank. The finite cell method for three-dimensional problems of solid mechanics. *Computer Methods in Applied Mechanics and Engineering*, 197(45–48):3768 – 3782, 2008.

[138] D. Schillinger and E. Rank. An unfitted hp-adaptive finite element method based on hierarchical B-splines for interface problems of com-

plex geometry. *Computer Methods in Applied Mechanics and Engineering*, 200(47–48):3358 – 3380, 2011.

[139] E. Rank, M. Ruess, S. Kollmannsberger, D. Schillinger, and A. Düster. Geometric modeling, isogeometric analysis and the finite cell method. *Computer Methods in Applied Mechanics and Engineering*, 249:104–115, 2012.

[140] D. Schillinger, L. Dede, M. A. Scott, J. A. Evans, M. J. Borden, E. Rank, and T. J. R. Hughes. An isogeometric design-through-analysis methodology based on adaptive hierarchical refinement of NURBS, immersed boundary methods, and T-spline CAD surfaces. *Computer Methods in Applied Mechanics and Engineering*, 249:116–150, 2012.

[141] D. Schillinger and M. Ruess. The finite cell method: A review in the context of higher-order structural analysis of CAD and image-based geometric models. *Archives of Computational Methods in Engineering*, pages 1–65, 2014.

[142] M. Ruess, D. Tal, N. Trabelsi, Z. Yosibash, and E. Rank. The finite cell method for bone simulations: Verification and validation. *Biomechanics and Modeling in Mechanobiology*, 2011.

[143] C.V. Verhoosel, G.J. van Zwieten, B. van Rietbergen, and R. de Borst. Image-based goal-oriented adaptive isogeometric analysis with application to the micro-mechanical modeling of trabecular bone. *Computer Methods in Applied Mechanics and Engineering*, 284:138 – 164, 2015.

[144] D. Kamensky, M. C. Hsu, D. Schillinger, J. A. Evans, A. Aggarwal, Y. Bazilevs, M. S. Sacks, and T. J. R. Hughes. An immersogeometric variational framework for fluid–structure interaction: Application to bioprosthetic heart valves. *Computer Methods in Applied Mechanics and Engineering*, 2014.

[145] M.-C. Hsu, D. Kamensky, F. Xu, J. Kiendl, C. Wang, M.C.H Wu, J. Mineroff, A. Reali, Y. Bazilevs, and M.S. Sacks. Dynamic and fluid-structure interaction simulations of bioprosthetic heart valves using parametric design with T-splines and Fung-type material models. *Computational Mechanics*, 55:1211–1225, 2015.

[146] E. Burman. Ghost penalty. *Comptes Rendus Mathematique*, 348(21-22):1217–1220, 2010.

[147] F de Prenter, CV Verhoosel, GJ van Zwieten, and EH van Brummelen. Condition number analysis and preconditioning of the finite cell method. *Computer Methods in Applied Mechanics and Engineering*, 316:297–327, 2017.

[148] I. Babuška and U. Banerjee. Stable generalized finite element method (sgfem). *Computer Methods in Applied Mechanics and Engineering*, 201:91–111, 2012.

[149] E. Burman and P. Hansbo. Fictitious domain methods using cut elements: Iii. a stabilized nitsche method for stokes' problem. *ESAIM: Mathematical Modelling and Numerical Analysis*, 48(3):859–874, 2014.

[150] B. Schott and W.A. Wall. A new face-oriented stabilized xfem approach for 2d and 3d incompressible navier–stokes equations. *Computer Methods in Applied Mechanics and Engineering*, 276:233–265, 2014.

[151] A. Massing, M.G. Larson, A. Logg, and M.E. Rognes. A stabilized nitsche fictitious domain method for the stokes problem. *Journal of Scientific Computing*, 61(3):604–628, 2014.

[152] J. Guzmán and M. Olshanskii. Inf-sup stability of geometrically unfitted stokes finite elements. *arXiv preprint arXiv:1605.09681*, 2016.

[153] A. Massing, B. Schott, and Wolfgang A. Wall. A stabilized nitsche cut finite element method for the oseen problem. *arXiv preprint arXiv:1611.02895*, 2016.

[154] F. Xu, D. Schillinger, D. Kamensky, V. Varduhn, C. Wang, and M-C. Hsu. The tetrahedral finite cell method for fluids: Immersogeometric analysis of turbulent flow around complex geometries. *Computers & Fluids*, 2015.

[155] D. Kamensky, M.C. Hsu, Y. Yu, J.A. Evans, M.S. Sacks, and T.J.R. Hughes. Immersogeometric cardiovascular fluid–structure interaction analysis with divergence-conforming b-splines. *Computer Methods in Applied Mechanics and Engineering*, 314:408–472, 2017.

[156] J. Parvizian, A. Düster, and E. Rank. Finite cell method – h- and p-extension for embedded domain problems in solid mechanics. *Computational Mechanics*, 41:121–133, 2007.

[157] R. Mittal and G. Iaccarino. Immersed boundary methods. *Annual Review of Fluid Mechanics*, 37:239–261, 2005.

[158] Z. Li and K. Ito. *The immersed interface method: numerical solutions of PDEs involving interfaces and irregular domains*. Society for Industrial and Applied Mathematics, 2006.

[159] R. Lohner, R. J. Cebral, F. E. Camelli, S. Appanaboyina, J. D. Baum, E. L. Mestreau, and O. A. Soto. Adaptive embedded and immersed unstructured grid techniques. *Computer Methods in Applied Mechanics and Engineering*, 197:2173–2197, 2008.

[160] H. Casquero, C. Bona-Casas, and H. Gomez. A NURBS-based immersed methodology for fluid–structure interaction. *Computer Methods in Applied Mechanics and Engineering*, 284:943–970, 2015.

[161] A. Johansson, M.G. Larson, and A. Logg. High order cut finite element methods for the Stokes problem. *Advanced Modeling and Simulation in Engineering Sciences*, 2(1):1, 2015.

[162] S. Fernández-Méndez and A. Huerta. Imposing essential boundary conditions in mesh-free methods. *Computer methods in applied mechanics and engineering*, 193(12):1257–1275, 2004.

[163] J. Nitsche. Uber ein Variationsprinzip zur Losung von Dirichlet-Problemen bei Verwendung von Teilraumen, die keinen Randbedingungen unterworfen sind. *Abhandlungen aus dem Mathematischen Seminar der Universitat Hamburg*, 36(1):9–15, 1971.

[164] A. Embar, J. Dolbow, and I. Harari. Imposing Dirichlet boundary conditions with Nitsche's method and spline-based finite elements. *International Journal for Numerical Methods in Engineering*, 83(7):877–898, 2010.

[165] M. Ruess, D. Schillinger, Y. Bazilevs, V. Varduhn, and E. Rank. Weakly enforced essential boundary conditions for NURBS-embedded and trimmed NURBS geometries on the basis of the finite cell method. *International Journal for Numerical Methods in Engineering*, 95:811–846, 2013.

[166] D.A. Di Pietro and A. Ern. *Mathematical Aspects of Discontinuous Galerkin Methods*. Springer, 2012.

[167] J.A. Evans and T.J.R. Hughes. Explicit trace inequalities for isogeometric analysis and parametric hexahedral finite elements. *Numerische Mathematik*, 123(2):259–290, 2012.

[168] M. Dauge, A. Düster, and E. Rank. Theoretical and numerical investigation of the finite cell method. *J. Sci. Comput.*, 65:1039–1064, 2015.

[169] V. Varduhn, M-C Hsu, M. Ruess, and D. Schillinger. The tetrahedral finite cell method: Higher-order immersogeometric analysis on adaptive non-boundary-fitted meshes. *International Journal for Numerical Methods in Engineering*, 2016. In press.

[170] L. Kudela, N. Zander, T. Bog, S. Kollmannsberger, and E. Rank. Efficient and accurate numerical quadrature for immersed boundary methods. *Advanced Modeling and Simulation in Engineering Sciences*, 2(1):1, 2015.

[171] L. Kudela, N. Zander, S. Kollmannsberger, and E. Rank. Smart octrees: Accurately integrating discontinuous functions in 3D. *Computer Methods in Applied Mechanics and Engineering*, 306:406–426, 2016.

[172] A. Massing, M.G. Larson, and A. Logg. Efficient implementation of finite element methods on nonmatching and overlapping meshes in three dimensions. *SIAM Journal on Scientific Computing*, 35(1):C23–C47, 2013.

[173] D.S. Malkus. Eigenproblems associated with the discrete LBB condition for incompressible finite elements. *International Journal of Engineering Science*, 19(10):1299–1310, 1981.

[174] F. Auricchio, L.B. da Veiga, A. Buffa, C Lovadina, A Reali, and G Sangalli. A fully "locking-free" isogeometric approach for plane linear elasticity problems: A stream function formulation. *Computer methods in applied mechanics and engineering*, 197(1-4):160–172, 2007.

[175] E. Burman. A penalty-free nonsymmetric Nitsche-type method for the weak imposition of boundary conditions. *SIAM Journal on Numerical Analysis*, 50(4):1959–1981, 2012.

[176] T.M. van Opstal, J. Yan, C. Coley, J.A. Evans, T. Kvamsdal, and Y. Bazilevs. Isogeometric divergence-conforming variational multiscale formulation of incompressible turbulent flows. *Computer Methods in Applied Mechanics and Engineering*, 316:859 – 879, 2017.

[177] T. Elguedj, Y. Bazilevs, V.M. Calo, and T.J.R. Hughes. B-bar and f-bar projection methods for nearly incompressible linear and non-linear elasticity and plasticity using higher-order nurbs elements. *Computer methods in applied mechanics and engineering*, 197(33):2732–2762, 2008.

[178] P. Antolin, A. Bressan, A. Buffa, and G. Sangalli. An isogeometric method for linear nearly-incompressible elasticity with local stress projection. *Computer Methods in Applied Mechanics and Engineering*, 316:694–719, 2017.

[179] T. Hoang, C.V. Verhoosel, F. Auricchio, E.H. van Brummelen, and A. Reali. Mixed isogeometric finite cell methods for the stokes problem. *Computer Methods in Applied Mechanics and Engineering*, 316:400 – 423, 2017. Special Issue on Isogeometric Analysis: Progress and Challenges.

[180] Michael Schäfer, Stefan Turek, Franz Durst, Egon Krause, and Rolf Rannacher. Benchmark computations of laminar flow around a cylinder.

In *Flow simulation with high-performance computers II*, pages 547–566. Springer, 1996.

[181] EH van Brummelen, KG van der Zee, VV Garg, and S Prudhomme. Flux evaluation in primal and dual boundary-coupled problems. *Journal of Applied Mechanics*, 79(1), 2012.

[182] V. John. Reference values for drag and lift of a two-dimensional time-dependent flow around a cylinder. *International Journal for Numerical Methods in Fluids*, 44(7):777–788, 2004.

[183] B.S. Hosseini, M. Möller, and S. Turek. Isogeometric analysis of the navier–stokes equations with taylor–hood b-spline elements. *Applied Mathematics and Computation*, 267:264–281, 2015.

[184] G. Nabh. *On high order methods for the stationary incompressible Navier-Stokes equations*. Interdisziplinäres Zentrum für Wiss. Rechnen der Univ. Heidelberg, 1998.

[185] I. Babuška and A. Miller. The post-processing approach in the finite element method—part 1: Calculation of displacements, stresses and other higher derivatives of the displacements. *International Journal for Numerical Methods in Engineering*, 20(6):1085–1109, 1984.

[186] DFG benchmark 2D-2 (Re100, periodic) - Featflow. http://www.featflow.de/en/benchmarks/cfdbenchmarking/flow/dfg_benchmark2_re100.html. Accessed: 2017-10-28.

[187] C Ross Ethier and DA Steinman. Exact fully 3d navier–stoskes solutions for benchmarking. *International Journal for Numerical Methods in Fluids*, 19(5):369–375, 1994.

[188] T. Hoang, C.V. Verhoosel, F. Auricchio, E.H. van Brummelen, and A. Reali. Skeleton-stabilized isogeometric analysis: High-regularity interior-penalty methods for incompressible viscous flow problems. *arXiv preprint arXiv:1711.04910*, 2017.

[189] A. Düster, E. Rank, and B. Szabó. The p-version of the finite element and finite cell methods. *Encyclopedia of computational mechanics. Chichester: John Wiley & Sons*, 2017.

[190] E. Burman and P. Hansbo. Fictitious domain finite element methods using cut elements: Ii. a stabilized nitsche method. *Applied Numerical Mathematics*, 62(4):328–341, 2012.

[191] M. G. Larson and A. Massing. L^2-error estimates for finite element approximations of boundary fluxes. *arXiv preprint arXiv:1401.6994*, 2014.

[192] M. Giles, M.G. Larson, J.M. Levenstam, and E. Süli. Adaptive error control for finite element approximations of the lift and drag coefficients in viscous flow. 1997.

[193] C. Qin, S.M. Hassanizadeh, and A. Ebigbo. Pore-scale network modeling of microbially induced calcium carbonate precipitation (micp): Insight into scale dependence of biogeochemical reaction rates. *Water Resources Research*, 52, 2016.

[194] E.H. van Brummelen, M. Shokrpour Roudbari, and G.J. van Zwieten. Elasto-capillarity simulations based on the Navier-Stokes-Cahn-Hilliard equations. In *Advances in Computational Fluid-Structure Interaction and Flow Simulation*, Modeling and Simulation in Science, Engineering and Technology, pages 451–462. Birkhäuser, 2016.

[195] J. Bueno, H. Casquero, Y. Bazilevs, and H. Gomez. Three-dimensional dynamic simulation of elastocapillarity. *Meccanica*, pages 1–17, 2017.

[196] E.H. van Brummelen, M. Shokrpour Roudbari, G. Simsek, and K.G. van der Zee. *Fluid Structure Interaction*, volume 20 of *Radon Series on Computational and Applied Mathematics*, chapter Binary-fluid–solid interaction based on the Navier–Stokes–Cahn–Hilliard Equations. De Gruyter, 2017.

Summary

Finite Element Analysis (FEA) of incompressible flow problems has been an active topic of research over the last decades, with research interests ranging from theoretical aspects to engineering applications. In recent years, IsoGeometric Analysis (IGA) – a spline-based finite element simulation paradigm proposed by Hughes et al. in 2005 – has been demonstrated to be very suitable for the simulation of incompressible flow problems. One advantage of isogeometric analysis is that it leverages the spline basis functions used to parametrize the geometry to directly construct approximation spaces for the velocity and pressure fields, thereby improving the integration between Computer Aided Design (CAD) tools and finite element simulations. An additional advantage of isogeometric analysis pertains to the smoothness of the employed spline functions. The higher-order continuity of these functions can be leveraged to construct approximation spaces with superior properties compared to traditional Lagrange finite elements.

Immersed simulation techniques – in particular the Finite Cell Method (FCM) introduced by Rank et al. 2007 – are a natural companion to isogeometric analysis. The key idea of such techniques is to extend a geometrically complex physical domain of interest into a geometrically simple embedding domain, on which a regular mesh can be built easily. Simulation strategies leveraging the advantages of isogeometric analysis and immersed methods are referred to as immersogeometric analysis techniques. On the one hand immersogeometric analysis facilitates consideration of CAD trimming curves in the context of isogeometric analysis. On the other hand, it enables the constructions of high-regularity spline spaces over geometrically and topologically complex volumetric domains, for which analysis-suitable spline parametrizations are generally not available.

The main goal of this dissertation is to develop a robust simulation strategy for incompressible flow problems based on the isogeometric and immersogeometric analysis frameworks. To accomplish this goal, first the complications related to using compatible isogeometric elements in an immersed context had to be identified. Based on the insights from this study an alternative formulation that rigorously resolves these complications could then be developed.

Isogeometric analysis of mixed formulations for incompressible flow problems based on inf-sup stable velocity-pressure pairs has been studied in detail in the literature, which has led to the development of a range of isogeometric element families, namely: Taylor-Hood elements, Sub-grid elements, Raviart-Thomas elements, and Nédélec elements. To understand the performance of these element families in an immersed setting, we have studied their behavior for the prototypical problem of steady Stokes flow in a quarter annulus ring. All isogeometric element families were found to exhibit local oscillations in the pressure field near cut boundaries. The occurrence of such oscillations on cut elements with relatively large volume fractions implies that this problem is related to the inf-sup stability of the discrete problem, rather than to conditioning issues related to cut elements with small volume fractions.

We proposed a novel stabilization technique to avoid the stability problem of immersogeometric analysis of incompressible flow problems based on inf-sup stable velocity-pressure pairs. The pivotal idea of this technique is to control the jump of high-order derivatives of the pressure field over the skeleton structure of the mesh. This skeleton-based stabilization technique allows utilizing identical discrete spaces for the velocity and pressure fields. This method – which to the best of our knowledge is new in the context of mesh-conforming isogeometric analysis – can be considered as a high-regularity extension of the (Continuous) Interior Penalty methods, making it applicable to a broad class of spline discretizations with arbitrary continuity conditions across element interfaces. To enable application of the skeleton-based stabilization technique in the immersogeometric context, the system had to be complemented with a stabilization term for the velocity space similar to that of the pressure space. In contrast to the pressure stabilization, the velocity stabilization – which is referred to in the literature as Ghost-penalty stabilization – is only applied at the faces of the background mesh skeleton structure that are located near the cut boundaries.

Since the proposed skeleton-based stabilization technique is applicable in the conforming setting, we have studied its performance for a range of Stokes flow and moderate Reynolds number Navier-Stokes flow benchmark problems on two and three-dimensional conforming meshes, including the case of a multi-patch NURBS-based isogeometric analysis. We have observed the skeleton-based stabilization method to yield solutions that are free of pressure oscillations and velocity locking effects, and to yield optimal rates of convergence under mesh refinement. Although a fundamental study of the selection of the stabilization parameter is beyond the scope of this work, we have observed robustness of the method within a sufficiently large range of parameters. The observations for the conforming isogeometric setting extend to the immersogeometric setting, where we have considered a range of two and three-dimensional problems for incompressible flows. To demonstrate the versatility of the proposed simulation strategy we have considered the immersogeometric analysis of Stokes flow through a porous medium, where the geometry is extracted directly from three-dimensional scan data.

Curriculum Vitae

Tuong Hoang was born on 08^{th} July 1986 in Ho Chi Minh city, Vietnam. In 2004 he finished his secondary education (specializing in mathematics) at the High School for the Gifted - Vietnam National University, in Ho Chi Minh city, Vietnam. After completing his Bachelor of Science in Mathematics with the thesis on Commutative Algebra in 2008 at the Ho Chi Minh city University of Education, he studied Master of Science in Mathematical Analysis at the University of Science in Ho Chi Minh city, Vietnam and graduated in 2012 with the first rank in the program. The results from his master thesis were published as the paper entitled "*An isogeometric analysis for elliptic homogenization problems*" (CAMWA, 2014), which was later given the award by the Vietnam Ministry of Education and Training in 2014 under the National Program for Development of Mathematics (NPDM). In November 2013, he received the Erasmus Mundus Joint Doctorate Fellowship (EMJD-SEED) offered by the European Commission, and started his PhD project at the Istituto Universitario di Studi Superiori di Pavia, Italy, and Technische Universiteit Eindhoven, The Netherlands, of which the results are presented in this dissertation. Since 01^{st} January 2018, he is employed as a postdoc fellow at the Utrecht University, The Netherlands, working on the topic of flow and transport in porous media, within the ERC Advanced project *SciPore*.